ROYAL SOCIETY OF CHEMISTRY

REVIEW

Check for updates

All-solid-state lithium batteries enabled by sulfide electrolytes: from fundamental research to practical engineering design

Changhong Wang, Jianwen Liang, Yang Zhao, Matthew Zheng, Xiaona Li and Xueliang Sun [ID] *

Sulfide electrolyte (SE)-based all-solid-state lithium batteries (ASSLBs) have gained worldwide attention because of their instrinsic safety and higher energy density over conventional lithium-ion batteries (LIBs). However, poor air stability of SEs, detrimental interfacial reactions, insufficient solid–solid ionic contact, and the large gap between fundamental study and practical engineering have impeded the commercialization of SE-based ASSLBs. This review aims to combine fundamental and engineering perspectives to rationally design practical SE-based ASSLBs with high energy density, covering SEs, interface, and practical all-solid-state pouch cells. First, the latest progress of typical pseudo-binary, pseudo-ternary, and pseudo-quaternary SEs is summarized, and effective strategies to improve ionic conductivity and chemical and electrochemical stability are highlighted. Moreover, challenges and strategies at the cathode and anode interfaces are reviewed separately. Furthermore, advanced *in situ* characterization techniques are examined to better understand the interface of ASSLBs. Encouraging demonstrations of SE-based all-solid-state lithium-ion and all-solid-state lithium–sulfur batteries are exemplified. Most importantly, energy-density-oriented all-solid-state pouch cells are designed using practical engineering parameters. The proposed design can serve as a quantitative framework to predict the practical energy density of SE-based all-solid-state pouch cells in future. Finally, future directions and our perspectives in SE-based ASSLBs are presented.

Broader context

All-solid-state lithium batteries (ASSLBs) with solid-state sulfide electrolytes (SEs) are thought to be one of the most promising alternatives to state-of-the-art lithium-ion batteries because of their much-improved safety and energy density. Over the past few years, continuous efforts have been made to develop SEs with high air stability and high ionic conductivity, and to eliminate large interfacial resistance between SEs and electrodes. The large gap between fundamental research and practical engineering, however, stymies the development of SE-based ASSLBs considerably. As a result, it is crucial to unify academic and industrial research objectives and advocate for goal-oriented research activities. This review not only summarizes the latest fundamental research advances in SE-based ASSLBs including all-solid-state lithium-ion batteries (ASSLIBs) and all-solid-state lithium–sulfur batteries (ASSLSBs) but also presents an energy-density-oriented design of all-solid-state pouch cells with realistic engineering parameters. The proposed design can serve as a quantitative framework to estimate the practical energy density of SE-based all-solid-state pouch cells. Future research directions are outlined to help guide the development of practical SE-based all-solid-state pouch cells with high energy density. This review bridges the large gap between fundamental research and practical engineering design of SE-based ASSLBs, pushing them one step closer to commercialization.

1. Introduction

Lithium-ion batteries (LIBs) as an efficient energy storage system have successfully revolutionized consumer electronics and electric-powered transportation.[1] The continuous upsurge in demand for the energy density of LIBs impels people to

Department of Mechanical and Materials Engineering, University of Western Ontario, 1151 Richmond St, London, Ontario, N6A 3K7, Canada. E-mail: xsun9@uwo.ca

explore high-voltage and/or high capacity electrodes, such as $LiNi_{0.9}Mn_{0.05}Co_{0.05}O_2$, a Li metal anode. Undoubtedly, high-voltage electrodes lead to poor electrode–electrolyte interfaces due to the limited electrochemical window of organic liquid electrolytes.[2,3] Besides, conventional organic liquid electrolytes are flammable, which is the root cause for safety hazards of current LIBs.[4] Under this circumstance, the ideal solution is to replace the flammable organic liquid electrolytes with some advanced non-flammable electrolytes, *e.g.* aqueous electrolytes

This journal is © The Royal Society of Chemistry 2021

Energy Environ. Sci., 2021, **14**, 2577–2619 | **2577**

and solid-state electrolytes. Aqueous batteries possess great competitiveness in safety, low cost, or environmental friendliness.[5–8] However, their large-scale application is plagued by limited output voltages and insufficient energy density.[9–11] Comparatively, solid-state electrolyte-based all-solid-state lithium batteries (ASSLBs) have gained increasing attention in recent years due to their superior advantages in excellent safety and high energy density.[12] Moreover, ASSLBs can be simply constructed by stacking bipolar electrodes with ultrathin solid-state electrolyte membranes.[13,14] Thus, ASSLBs can achieve high energy density at the system level.[3,15]

To realize ASSLBs, solid-state electrolytes are indispensable.[16] Over the past decades, numerous efforts have been made to develop solid-state electrolytes with high ionic conductivity, such as solid-state oxide electrolytes,[17–21] sulfide electrolytes (SEs),[22,23]

solid polymer electrolytes,[24–29] halide electrolytes,[30–42] borohydrides,[43–48] anti-perovskites,[49–53] and their hybrids.[54–56] Among them, solid-state SEs generally exhibit the highest ionic conductivity (10^{-3}–10^{-2} S cm^{-1}) and favorable mechanical properties.[57] For these reasons, SEs are gaining substantial research interest in both academia and industry.[13] However, the commercialization of SE-based ASSLBs is significantly impeded by major challenges, such as moisture sensitivity of SEs, narrow electrochemical windows, detrimental interfacial reactions at both the cathode and anode interfaces, and a large gap between fundamental research and practical engineering design. With continuous efforts in the last decade, various effective strategies have been proposed to address the aforementioned challenges and many exciting achievements have been demonstrated. Although there are several review papers related to sulfide electrolytes, most of

Changhong Wang

Dr Changhong Wang received his PhD degree in Mechanical and Materials Engineering in 2020 from Western University of Ontario (UWO) under the supervision of Prof. Xueliang (Andy) Sun. He is currently serving as the R&D director of GLABAT solid-state battery Inc. in Canada. He obtained his MS degree in Materials Engineering from the University of Science and Technology of China (USTC) in 2014. He has worked at the Singapore University of Technology and Design (SUTD) from 2014 to 2016 and focusing on electronic synapses for neuromorphic computing. His research interests include solid-state batteries, solid electrolytes, pouch cells, and electronic synapses.

Jianwen Liang

Dr Jianwen Liang is a Mitacs Postdoc Fellow in Prof. Xueliang (Andy) Sun's Group at the University of Western Ontario (Western University), Canada. He received his BS degree in Chemical Engineering and Technology from Wuyi University in 2010 and PhD degree in inorganic chemistry from the University of Science and Technology of China in 2015. He joined Prof. Sun's group in 2017 and his current research interests include sulfide and halide solid electrolytes as well as all-solid-state Li/Li-ion batteries.

Yang Zhao

Dr Yang Zhao is an Assistant Professor in the Department of Mechanical and Materials Engineering at the University of Western Ontario, Canada. Dr Zhao received his BS and MS degrees from Northwestern Polytechnical University (Xi'an, China) in 2011 and 2014, respectively. He obtained his PhD degree under the supervisor of Prof. Xueliang (Andy) Sun from the University of Western Ontario in 2018. Then, he had his postdoc training at Western and the Advanced Light Source of Lawrence Berkeley National Laboratory in 2019–2020. His research interests focus on advanced materials and interfaces for energy storage applications, and synchrotron-based X-ray techniques.

Matthew Zheng

Matthew Zheng is currently a PhD student under the supervision of Xueliang (Andy) Sun at the University of Western Ontario, Canada. Matthew received his BASc at the University of British Columbia in 2020. His research interests include application of 3D-printing and thin-film coating techniques for lithium metal batteries.

them generally focus on a specific theme such as the progress of solid-state SEs and/or interface between electrode and SEs,[13,14,22,58–66] seldom taking the industrial design of SE-based all-solid-state pouch cells into discussion. Considering that a series of exciting achievements have been realized in recent years and an increasing number of start-ups have reported their progress on SE-based all-solid-state pouch cells with high energy density, it is urgent and important to give a comprehensive review on SE-based ASSLBs with a joint viewpoint of fundamental research and engineering design to bridge the gap between fundamental research and industrial design and therefore, help propel the commercialization of SE-based ASSLBs.

In this comprehensive review, we start with discussing the state-of-the-art of the typical SEs, categorized into pseudo-binary (i.e. $Li_2S–P_2S_5$ or $Li_2S–MS_2$, M = Ge, Si, Sn), pseudo-ternary (i.e. $Li_2S–P_2S_5–MS_2$ or, $Li_2S–P_2S_5–LiX$, M = Ge, Si, Sn, etc.; X = F, Cl, Br, and I), and pseudo-quaternary systems ($Li_2S–P_2S_5–MS_2–LiX$, M = Ge, Si, Sn, etc.; X = F, Cl, Br, and I), followed by lithium-ion transport mechanisms as well as different strategies to improve the ionic conductivity and chemical and electrochemical stability. Thereafter, the latest progress on electrochemical and chemical stabilities of SEs are thoroughly examined. We then discuss the cathodic and anodic interfacial challenges between the cathode/anode and SE together with the promising and emerging strategies. To deepen the understanding of mysterious interfacial issues, advanced in situ characterization techniques are summarized. As examples, encouraging achievements of SE-based all-solid-state lithium-ion batteries (ASSLIBs) and all-solid-state lithium–sulfur batteries (ASSLSBs) are exemplified. More importantly, with various energy density targets of 250–500 W h kg^{-1}, practical all-solid-state pouch cells are carefully designed with practical engineering parameters, and viable manufacturing strategies for SE-based ASSLBs are discussed. Finally, the future research directions and our perspectives on SE-based ASSLBs are presented. We truly believe that this comprehensive review not only provides a fundamental and in-depth understanding of SE-based ASSLBs but also guides the engineering design of practical all-solid-state pouch cells with high energy density, thus propelling the development of SE-based ASSLBs (Fig. 1).

1.1 History of solid-state sulfide electrolytes

The earliest research on sulfide electrolytes starts from 1980s,[13,67] focusing on glassy materials, such as $Li_2S–P_2S_5–LiI$ (2 mS cm^{-1}),[68] $B_2S_3–Li_2S–LiI$ (1 mS cm^{-1}),[69] $Li_2S–SiS_2–GeS_2$,[70] and Li_3PS_4,[71] which generally exhibit an ionic conductivity approximately 1 mS cm^{-1}. Due to the rapid development and commercialization of LIBs since the 1990s, the investigation of SE-based ASSLBs slowed down. In 2001, R. Kanno et al. synthesized $Li_2S–P_2S_5–GeS_2$ with an ionic conductivity of 2.2 mS cm^{-1}.[72] With his continuous efforts, R. Kanno et al. reported a superionic solid electrolyte $Li_{10}GeP_2S_{12}$ (LGPS) that showed a high ionic conductivity of 12 mS cm^{-1} in 2011,[73] overtaking that of conventional liquid electrolytes (approximately 10 mS cm^{-1}).[2] That groundbreaking report encouraged a strong research enthusiasm in developing fast ionic conductors, including Na$^+$-conductor analogs.[74–76] In 2016, a solid-state electrolyte $Li_{9.54}Si_{1.74}P_{1.44}S_{11.7}Cl_{0.3}$ was reported by Toyota Motor Corporation, displaying the highest ionic conductivity among all-reported SEs so far (25 mS cm^{-1}).[15] Recently, single-crystal LGPS was reported to show an ultra-high ionic conductivity of 27 mS cm^{-1} along the [001] direction.[77]

Besides the LGPS evolution routes, the glassy $Li_2S–P_2S_5$ system was also gradually improved over the past years. Remarkably, the highly conductive phase $Li_7P_3S_{11}$ phase in the $Li_2S–P_2S_5$ system was identified in 2005, which exhibits a high ionic conductivity of 3.2 mS cm^{-1}.[78] Further reducing the grain-boundary resistance by hot pressing can yield a high ionic conductivity of 17 mS cm^{-1},[79] as reported by Y. Seino et al. in 2014.[79]
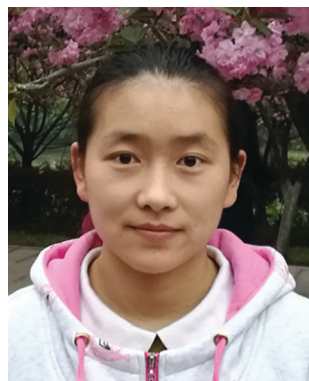
Xiaona Li

Dr Xiaona Li is a Mitacs Postdoc Fellow in Prof. Xueliang (Andy) Sun's Group at the University of Western Ontario (Western University), Canada. She received her BS degree in materials chemistry in 2011 from Sichuan University and PhD degree in inorganic chemistry in 2015 under the supervision of Prof. Yitai Qian on the study of electrode materials synthesis for lithium batteries from the University of Science and Technology of China. She joined Prof. Sun's group in 2017 and her current research interests focus on the synthesis of sulfide and halide solid electrolytes as well as all-solid-state lithium batteries.
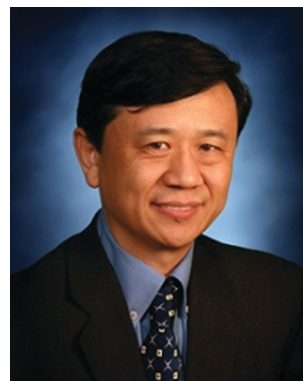
Xueliang Sun

Prof. Xueliang (Andy) Sun is a Canada Research Chair in the Development of Nanomaterials for Clean Energy, Fellow of the Royal Society of Canada and the Canadian Academy of Engineering, and Full Professor at the University of Western Ontario, Canada. Dr Sun received his PhD in materials chemistry in 1999 from the University of Manchester, UK, which he followed up by working as a postdoctoral fellow at the University of British Columbia and as a Research Associate at L'Institut National de la Recherche Scientifique (INRS), Canada. His current research interests are focused on advanced materials for electrochemical energy storage and conversion.

Fundamental Research
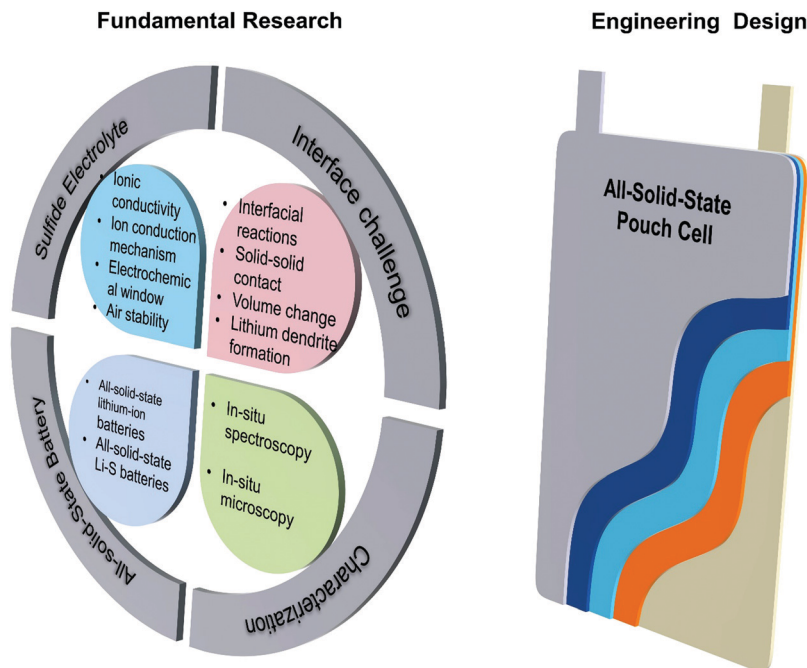
Engineering Design

Fig. 1 Overview of challenges and corresponding strategies of SEs and their ASSLBs from fundamental research to practical engineering design.

Lithium argyrodites (Li_6PS_5X, X = F, Cl, Br, and I) are another family of SEs with high ionic conductivity from 1–10 mS cm^{-1}, which was first reported in 2008 by Hans-Jorg Deiseroth et al.[80] Since then, the ionic conductivity and air stability of Li argyrodites were gradually improved by tuning the stoichiometric ratio and introducing doping elements, such as As, Se, Sb, Ge, Sn.[81–84] Recently, $Li_{5.5}PS_{4.5}Cl_{1.5}$ was synthesized by an ultimate-energy mechanical alloying method, exhibiting an ultra-high ionic conductivity of 10.2 mS cm^{-1}.[85] More interestingly, a new family of argyrodite thioantimonates was reported by L. Nazar's group, which exhibited a high room temperature ionic conductivity of 14.8 mS cm^{-1} for cold-pressed pellets and up to 24 mS cm^{-1} for sintered pellets.[86] Besides, lot of other lithium argyrodites, i.e. $Li_{5.35}Ca_{0.1}PS_{4.5}Cl_{1.55}$ (10.2 mS cm^{-1}),[87] $Li_{6.75}Sb_{0.25}Si_{0.75}S_5I$ (13.1 mS cm^{-1}),[88] were reported with a ionic conductivity over 10 mS cm^{-1} (Fig. 2).

Previously, many review papers categorized SEs from the perspective of their crystal structure.[14] In recent years, lots of pseudo-quaternary SEs (e.g. $Li_{9.54}Si_{1.74}P_{1.44}S_{11.7}Cl_{0.3}$) have been reported to show much-improved ionic conductivity.[15,89] However, they still belong to the same crystal structure. Therefore, it is not prudent to track the progress of SEs solely based on their crystal structure. Here we summarized SEs from their precursor-combinations, thereby clearly revealing the evolution and progress of SEs over past years. As shown in Fig. 3, SEs are categorized into (1) pseudo-binary systems including the $Li_2S–P_2S_5$ system and $Li_2S–MS_2$ system (Fig. 3A); (2) pseudo-ternary systems including $Li_2S–P_2S_5–MS_2$ (M = Ge, Sn, Si, Al, etc.) system and $Li_2S–P_2S_5–LiX$ (X = F, Cl, Br, I) (Fig. 3B); and (3) pseudo-quaternary system (Fig. 3C), e.g. $Li_2S + P_2S_5 + MS_2 + LiX$ (M = Ge, Sn, Si, Al, etc.; X = F, Cl, Br, I). In general, the sequence of ionic conductivity is

$\sigma_{\text{pseudoquaternary system}} > \sigma_{\text{pseudoternary system}} > \sigma_{\text{pseudobinary system}}$ (Fig. 3D). Following this category, the ionic conductivities and activation energies of typical SEs are summarized in Table 1. And the developing trend and typical characteristics of each type of SEs are discussed in detailed next.

1.2 Typical sulfide electrolytes

1.2.1 Pseudo-binary sulfide electrolytes

$Li_2S–P_2S_5$ system. The most typical pseudo-binary SEs include the $Li_2S–P_2S_5$ system and $Li_2S–MS_2$ (M = Ge, Sn, Si) system. Ionic conductivity and corresponding activation energy of some pseudo-binary SEs are listed in Table 1. The earliest attempts of the $Li_2S–P_2S_5$ system can date back to 1984, while γ-Li_3PS_4 was synthesized and displayed a low ionic conductivity of 10^{-7} S cm^{-1}. When heated to 195 °C, γ-Li_3PS_4 is converted to the high-conduction β-Li_3PS_4 phase, which shows an abrupt increase of ionic conductivity in the Arrhenius plot (Fig. 4A). However, β-Li_3PS_4 is meta-stable at elevated temperatures and easily reverts to its stable phase γ-Li_3PS_4 at temperatures under 195 °C. Therefore, stabilizing the high-conduction β-Li_3PS_4 phase at room temperature is a big challenge.[123] Fortunately, C. Liang et al. reported nanoporous Li_3PS_4 in 2013 (Fig. 4B) which allowed β-Li_3PS_4 to be well-maintained at room temperature with high ionic conductivity of 1.6 × 10^{-4} S cm^{-1}.[97] The findings of this referenced study suggested that increasing the surface energy of nanoporous Li_3PS_4 can promote surface conduction as the surface defects can enhance the lithium vacancy transport.[97,124–126]

In general, glass-ceramic $Li_2S–P_2S_5$ exhibits a room-temperature ionic conductivity over 10^{-4} S cm^{-1}. Interestingly, F. Mizuno et al. found that the crystallization of $Li_2S–P_2S_5$ glass-ceramics show extremely high ionic conductivity (3.2 × 10^{-3} S cm^{-1}) at ambient

2580 | *Energy Environ. Sci.*, 2021, **14**, 2577–2619

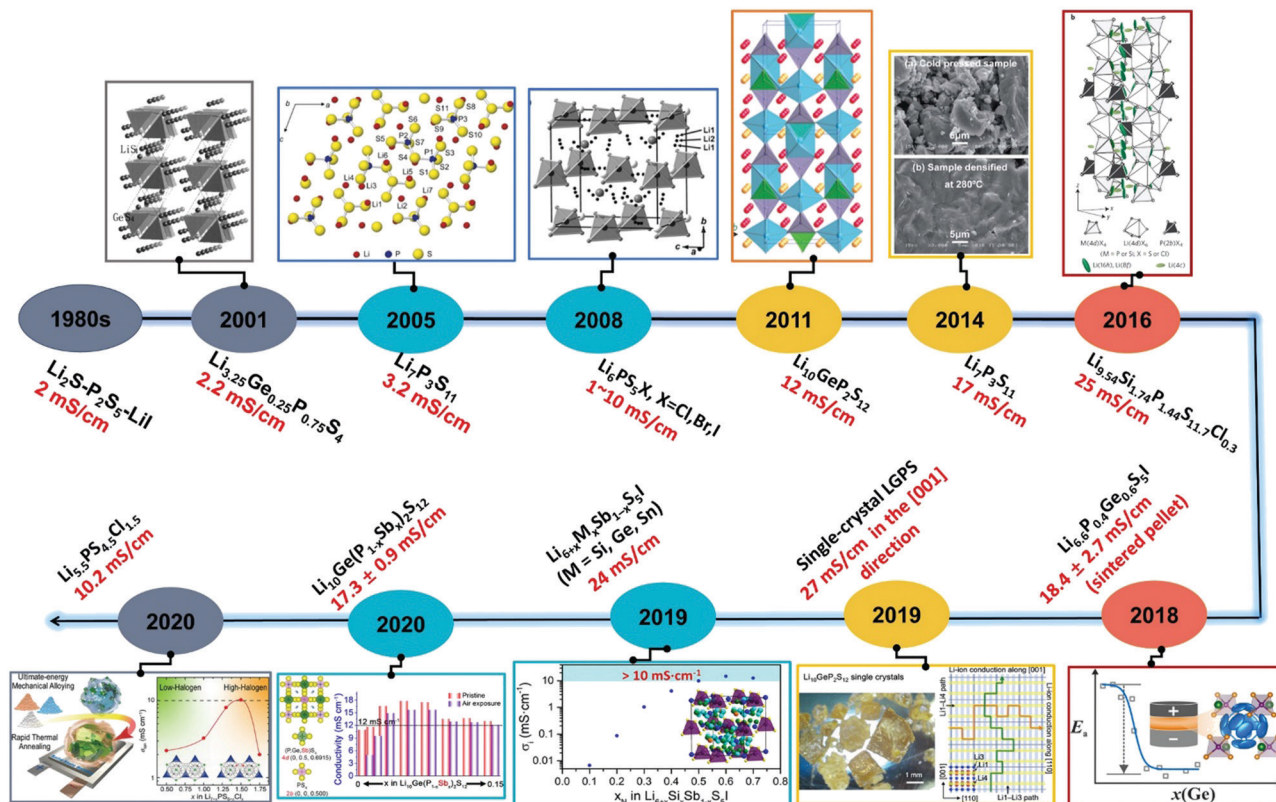This journal is © The Royal Society of Chemistry 2021

Fig. 2 Developing trend of solid-state sulfide electrolytes. It should be noted that the typical examples here are picked due to their excellent ionic conductivity. Reproduced with permission from ref. 72. Copyright (2001) The Electrochemical Society. Reproduced with permission from ref. 78, 90 and 91. Copyright (2005) Wiley-VCH, and Copyright (2013) Elsevier. Reproduced with permission from ref. 80 and 92. Copyright (2008) Wiley-VCH and Copyright (2016) American Chemical Society. Reproduced with permission from ref. 73. Copyright (2011) Nature Publishing Group. Reproduced with permission from ref. 79. Copyright (2014) Royal Society of Chemistry. Reproduced with permission from ref. 15. Copyright (2016) Nature Publishing Group. Reproduced with permission from ref. 82. Copyright (2018) American Chemical Society. Reproduced with permission from ref. 77. Copyright (2019) American Chemical Society. Reproduced with permission from ref. 86. Copyright (2019) American Chemical Society. Reproduced with permission from ref. 93. Copyright (2020) American Chemical Society. Reproduced with permission from ref. 85. Copyright (2020) American Chemical Society.

temperature,[78] which is much higher than those of glassy Li_2S–P_2S_5 and crystalline Li_2S–P_2S_5 prepared by solid-state reactions (Fig. 4C). This abnormal phenomenon is due to the formation of a highly-conductive phase $Li_7P_3S_{11}$,[91,127] One possible implication of this is that formation of the highly-conductive phase is crucial for improving the ionic conductivity of Li_2S–P_2S_5 glass-ceramics. Another important strategy used to improve the ionic conductivity of Li_2S–P_2S_5 glass-ceramics is by reducing the grain-boundary resistance by hot-pressing.[128,129] As shown in Fig. 4D, the high ionic conductivity of 17 mS cm^{-1} with a low activation energy of 17 kJ mol^{-1} can be obtained by hot-pressing Li_2S–P_2S_5 glass-ceramics. The reason is that the hot pressing eliminates voids and grain boundaries in SEs (Fig. 4D).[79,129,130] In recent years, a lot of pseudo-binary SEs were synthesized by the liquid-phase method,[131,132] such as Li_3PS_4,[97,133,134] and $Li_7P_3S_{11}$,[135–138] which is beneficial for improving the solid–solid ionic contact between SEs and electrodes. A. Miura et al. provided a systematic review of the liquid-phase synthesis of SEs for all-solid-state batteries.[22] Besides, G. Michael et al. reviewed the liquid-phase synthesis of the Li–P–S system from a chemical perspective.[132] It should be emphasized here that further improving the ionic conductivity of

SEs synthesized by the liquid-phase method is necessary and the impact of the solvent process on solid-state battery performance should be systematically investigated.[139]

Li_2S–MS_2 system. Other than Li_2S–P_2S_5 pseudo-binary system, the Li_2S–MS_2 pseudo-binary system including Li_2S–SiS_2,[102,103,141] Li_2S–SnS_2,[98,109] and Li_2S–GeS_2[104] have been well-developed over the past decade. Li_4SnS_4 exhibits an ionic conductivity of 7×10^{-5} S cm^{-1} at 20 °C.[109] The inferior ionic conductivity can be increased by As substitution. S. Gayatri et al. demonstrated that As-substituted Li_4SnS_4 exhibited an ionic conductivity of 1.39 mS cm^{-1} at 25 °C (Fig. 4E). As another benefit, As-substitution also improved the air and moisture stability of SEs.[98] Ge-Substituted Li_3AsS_4 ($Li_{3.334}Ge_{0.334}As_{0.666}S_4$) was also demonstrated to have a high ionic conductivity of 1.12×10^{-3} S cm^{-1} with a very low activation energy of 0.17 eV.[110] Taken together, these results suggest that heterovalent or aliovalent substitution creates interstitials or vacancies in the parent crystal matrix, thus enhancing the overall ionic conductivity of solid-state electrolytes. More recently, Y. Xie's group reported a high ionic conductor ($Li_xAg_{1-x}CrS_2$, $0 < x < 4$) with

This journal is © The Royal Society of Chemistry 2021

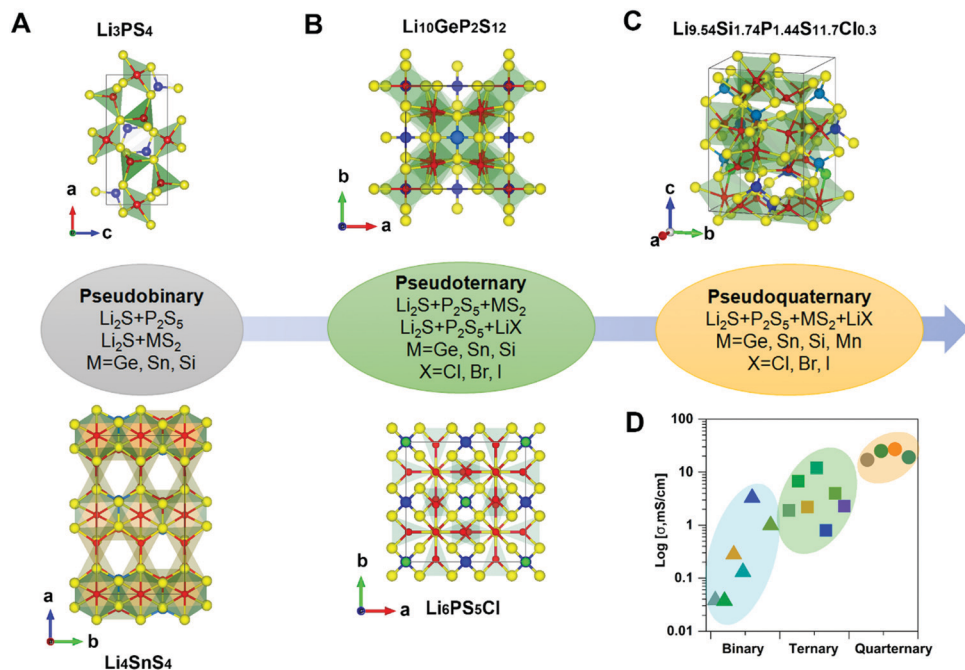Energy Environ. Sci., 2021, 14, 2577–2619 | 2581

Fig. 3 The main category of SEs and their typical examples. (A) Pseudo-binary system and crystal structures of the typical examples of Li_3PS_4 and Li_4SnS_4. (B) Pseudo-ternary system and crystal structures of classic examples $Li_{10}GeP_2S_{12}$ and Li_6PS_5Cl. (C) Pseudo-quaternary system and the crystal structure of typical $Li_{9.54}Si_{1.74}P_{1.44}S_{11.7}Cl_{0.3}$. (D) Ionic conductivities of typical pseudo-binary SEs, pseudo-ternary SEs, and pseudo-quaternary SEs. Data obtained from ref. 15, 72, 73, 77–80 and 93–101.

an ionic conductivity of 19.6 mS cm^{-1} given x is 0.31 (Fig. 4F). This opens a new avenue to develop a new Li^+ conductor based on two-dimensional layered structures.[140]

1.2.2 Pseudo-ternary sulfide electrolytes. Pseudo-ternary SEs mainly include $Li_2S–P_2S_5–MS_2$ (M = Ge, Si, Sn, Al, *etc.*) with a thio-LISICON (LIthium Super Ionic CONductor) structure and $Li_2S–P_2S_5–LiX$ (X = F, Cl, Br, and I) with an argyrodite structure. Both of them feature a high ionic conductivity of around 10^{-2} S cm^{-1}.

$Li_2S–P_2S_5–MS_2$ system. The most typical example of the $Li_2S–P_2S_5–MS_2$ system is the thio-LISICON family with a chemical formula of $Li_{10\pm1}MP_2X_{12}$, (M = Ge, Si, Sn, Al or P, and X = O, S, or Se), which demonstrated a very high ionic conductivity and in turn attracted worldwide research interest.[2] Historically, the earliest study on the thio-LISICON system can date back to 2001.[72] Kanno and his co-authors obtained an ionic conductivity of 2.2×10^{-3} S cm^{-1} at 25 °C by simply sintering the starting materials (Li_2S, GeS_2, and P_2S_5) at 700 °C for 8 hours. Later on, a series of thio-LISICON-typed SEs were developed, such as ternary $Li_2S–SiS_2–Al_2S_3$ and $Li_2S–SiS_2–P_2S_5$ systems.[104,107,112,142] With continuous efforts over 10 years, R. Kanno *et al.* disclosed a lithium superionic conductor (LGPS) in 2011, which exhibited an unprecedented conductivity of 1.2×10^{-2} S cm^{-1} at room temperature.[73] Besides, the high ionic conductivity of LGPS was also confirmed by the solid-state NMR technique, which showed that Li^+ hopping in LGPS is nearly an isotropic process with a low activation energy of 0.22 eV.[143] This superionic conductor has a 3D framework structure and one-dimensional (1D) Li conduction

path along the *c*-axis (Fig. 5A).[116,144,145] The 1D conduction pathway is formed by LiS_4 tetrahedra in the 16h and 8f sites, which share a common edge and form a 1D tetrahedron chain. These chains are connected by common corners of the LiS_4 tetrahedra (Fig. 5B). By neutron diffraction and maximum entropy methods, one-dimensional Li^+ conduction pathways of LGPS change to a three-dimensional conduction pathway at elevated temperatures.[145,146] Interestingly, Y. Mo *et al.* reported that the Li^+ transport of LGPS is not only along the *c*-axis but may be also along two other pathways in the *ab* plane. This was revealed by *ab initio* molecular dynamics simulations,[147] which was validated by neutron powder diffraction analysis reported by W. G. Zeier *et al.*[146] Experimentally, single-crystal $Li_{10}GeP_2S_{12}$ was successfully synthesized by a self-flux method. It was found that the ionic conductivity in the [001] and [110] directions was observed to be 27 and 7 mS cm^{-1}, respectively (Fig. 5C).[77]

The unprecedented ionic conductivity of LGPS sparked a new wave of enthusiasm in developing LGPS-type SEs.[120,148–154] The phase stability, electrochemical stability, and ionic conductivity of $Li_{10\pm1}MP_2X_{12}$ (M = Ge, Si, Sn, Al or P, and X = O, S, or Se) were systematically compared by *ab initio* molecular dynamics (MD) simulations.[155] The results show that isovalent cation substitutions have a small effect on the crystal structure, electrochemical stability, and Li^+ conductivity, and aliovalent cation substitutions (M = Al or P) with corresponding changes in the Li^+ concentration also seem to have a small effect on the Li^+ conductivity. However, anion substitutions make big difference in these properties.[155] Another concern of LGPS-typed

2582 | *Energy Environ. Sci.*, 2021, **14**, 2577–2619

This journal is © The Royal Society of Chemistry 2021

Table 1 State-of-the-art of solid-state SEs in the aspect of ionic conductivity and activation energy

Category	Composition	Ionic conductivity@RT (S cm^{-1})	Activation energy (eV)	Year	Ref.
Pseudo-binary system	γ-Li$_3$PS$_4$	1×10^{-7}	0.49	1984	71
	60Li$_2$S·40SiS$_2$	1×10^{-4}	0.31	1999	102 and 103
	Li$_4$GeS$_4$	2×10^{-7}		2000	104–106
		7.5×10^{-4} (film)	0.36	2011	
	75Li$_2$S·25P$_2$S$_5$	2×10^{-4}	0.35	2001	94
	80Li$_2$S·20P$_2$S$_5$	7.2×10^{-4}	0.29	2003	95
	Li$_{3.325}$P$_{0.675}$S$_4$	1.5×10^{-4}	0.31	2004	107
	70Li$_2$S·30P$_2$S$_5$	3.2×10^{-3}	0.12	2005	78, 79, 91, 96 and 108
	(Li$_7$P$_3$S$_{11}$ hot press)	1.7×10^{-2}		2014	
	Li$_4$SnS$_4$	3.2×10^{-3}	0.41	2012	109
	Li$_3$AsS$_4$	1.31×10^{-5}	0.40	2014	110 and 111
Pseudo-ternary system	Li$_{4-x}$Ge$_{1-x}$P$_x$S$_4$ ($x = 0.75$)	2×10^{-4}	0.21	2001	72
	Li$_2$S–SiS$_2$–P$_2$S$_5$	6.4×10^{-4}	0.29	2002	112
	Li$_2$S–SiS$_2$–Al$_2$S$_3$	2.3×10^{-7}	0.52	2002	112
	Li$_2$S–SiS$_2$–Li$_x$MO$_y$ (M = Si, P, Ge)	$>10^{-4}$	0.37	2002	113
	70Li$_2$S·27P$_2$S$_5$·3P$_2$O$_5$	3×10^{-3}	0.17	2008	114
	Li$_{10}$GeP$_2$S$_{12}$	1.2×10^{-2}	0.25	2012	73
	Li$_{10}$SnP$_2$S$_{12}$	4×10^{-3} (total)	0.27	2013	101
		7×10^{-3} (grain)	0.60 (grain boundary)		
	Li$_{11}$Si$_2$PS$_{12}$	$>1.2 \times 10^{-2}$	0.20	2014	100 and 115
	Li$_{3.45}$Si$_{0.45}$P$_{0.55}$S$_4$	6.7×10^{-3}	0.27	2014	116
	Li$_{11}$AlP$_2$S$_{12}$	8.02×10^{-4}	0.26	2016	117
	Li$_6$PS$_5$X (X = Cl, Br)	$\sim 10^{-3}$	0.33–0.41	2008	80
	Li$_6$PS$_5$Cl	1.9×10^{-3}	0.38	2011	118 and 119
		1.33×10^{-3}		2012	
	Li$_6$PS$_5$Br	6.8×10^{-3}	0.32	2011	118
	Li$_6$PS$_5$I	4.6×10^{-7}	0.26	2011	118
	Li$_7$P$_2$S$_8$I	6.3×10^{-4}	Unknown	2015	120
	Li$_{5.5}$PS$_{4.5}$Cl$_{1.5}$	1.02×10^{-2}	0.27	2020	85
	Li$_{5.35}$Ca$_{0.1}$PS$_{4.5}$Cl$_{1.55}$	1.02×10^{-2}	0.30	2021	87
Pseudo-quaternary system	Li$_{9.54}$Si$_{1.74}$P$_{1.44}$S$_{11.7}$Cl$_{0.3}$	2.5×10^{-2}	0.24	2016	15
	Li$_{10.35}$[Sn$_{0.27}$Si$_{1.08}$]P$_{1.65}$S$_{12}$	1.1×10^{-2}	0.20	2017	89
	Li$_7$P$_{2.9}$Mn$_{0.1}$S$_{10.7}$I$_{0.3}$	5.6×10^{-3}	0.216	2017	121
	Li$_{6+x}$M$_x$Sb$_{1-x}$S$_5$I	1.48×10^{-2}	0.25–0.41	2019	86
		2.4×10^{-2} (sintered)			
	Li$_{10}$Ge(P$_{1-x}$Sb$_x$)$_2$S$_{12}$	1.8×10^{-2}	0.27	2020	93
	30Li$_2$S·25B$_2$S$_3$·45LiI·25SiO$_2$	2.1×10^{-3}	0.33	2020	122
	Li$_{6.75}$Sb$_{0.25}$Si$_{0.75}$S$_5$I	1.31×10^{-2}	0.17	2021	88

solid electrolytes is cost because germanium is highly expensive. Therefore, the replacement of Ge with Sn, Al, Si to form Li$_{10}$SnP$_2$S$_{12}$,[101,156] Li$_{11}$AlP$_2$S$_{12}$,[117] Li$_{3.45}$Si$_{0.45}$P$_{0.55}$S$_4$,[116] could substantially lower the raw material cost without sacrificing ionic conductivity significantly.[101] Besides, using cheap raw materials (*i.e.* elemental Li, Ge, P, and S) not using highly expensive precursors (*i.e.* GeS$_2$, Li$_2$S), was successfully demonstrated to synthesized LGPS with a decent ionic conductivity of 3.2 mS cm^{-1} at room temperature.[157] Recently, R. Kanno's group provided a review of LGPS-typed SEs with a focus on synthesis, structure, and ion transport mechanisms.[66] So far the LGPS and its analogs are commercially available, which indicates that large-scale production is viable. The main challenges for this material are its relatively high reactivity with electrode materials, moisture sensitivity, as well as cost, each of which requires more effort to resolve in future.

Li$_2$S–P$_2$S$_5$–LiX system:

Lithium argyrodites (Li$_6$PS$_5$X, X = Cl, Br, I). The argyrodite family of compounds have a general formula of A$_{12-m-x}^+$(M^{m+}Y$_4^{2-}$)Y$_{2-x}^{2-}$X^{x-}, where A$^+$ = Li$^+$, Cu$^+$, Ag$^+$; M^{m+} = Si^{4+}, Ge^{4+}, Sn^{4+}, P^{5+}, As^{5+}; Y^{2-} = O^{2-}, S^{2-}, Se^{2-}, Te^{2-}; X$^-$ = Cl$^-$, Br$^-$, I$^-$; $0 \leq x \leq 2$. This family is named after the mineral

Ag$_8$GeS$_6$.[80,158–160] H. Deiseroth *et al.* first identified that Li$_6$PS$_5$X is a class of lithium-ion conductors with an unusually high Li$^+$ mobility by the nuclear magnetic resonance (NMR) technique.[80] Following that, Deiseroth and his co-authors conducted a series of research on the structure, phase transition, and lithium-ion conduction of lithium argyrodites by molecular dynamics simulation, solid-state NMR, and impedance spectroscopy,[81,83,161] where they showed that lithium argyrodites with a cubic phase possess three-dimensional lithium-ion conduction pathways.[99,159] V. Viallet *et al.* reported that the room-temperature ionic conductivities of Li$_6$PS$_5$Cl, Li$_6$PS$_5$Br, and Li$_6$PS$_5$I are 6.2×10^{-4} S cm^{-1}, 4.6×10^{-4} S cm^{-1}, and 1.9×10^{-4} S cm^{-1}, respectively.[119] J. Xie *et al.* employed Al^{3+} to partially substitute Li$^+$ in Li$_6$PS$_5$Br, leading to high ionic conductivity of 2.4×10^{-3} S cm^{-1}. The three-time increment in conductivity was ascribed to the shortened distance for Li-ions to jump[162] by density functional theory (DFT) molecular dynamics simulations, M. Wagemaker *et al.* investigated the origin of the lithium-ion conductivity in argyrodite solid electrolytes,[163,164] elucidating that not only do lithium-ion vacancies but also halogen atoms have an influence on their local surroundings and play an important role in the Li-ion diffusion of Li$_6$PS$_5$Cl and Li$_6$PS$_5$Br. Furthermore, simulations
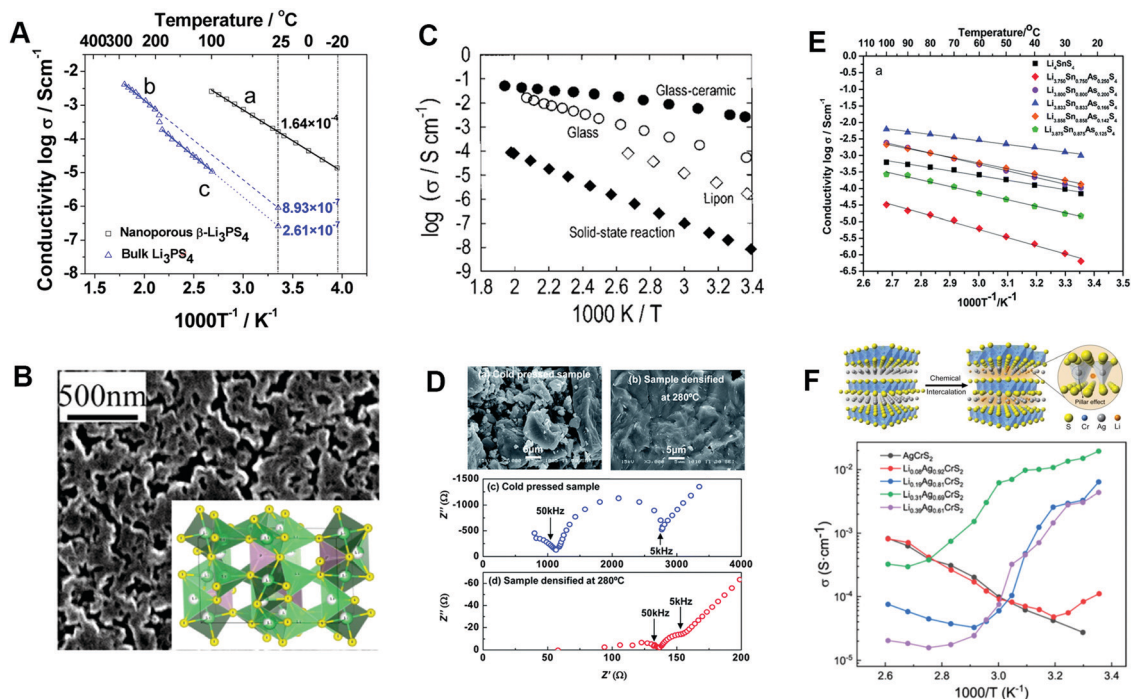
This journal is © The Royal Society of Chemistry 2021

Energy Environ. Sci., 2021, **14**, 2577–2619 | **2583**

Fig. 4 (A) Arrhenius plots for nanoporous β-Li₃PS₄ (line a), bulk β-Li₃PS₄ (line b), and bulk γ-Li₃PS₄ (line c).[97] (B) SEM image of the nanoporous β-Li₃PS₄ and its crystal structure framework inserted. Reproduced with permission from ref. 97. Copyright (2013) American Chemical Society. (C) The temperature-dependence of ionic conductivity of 70Li₂S·30P₂S₅ samples prepared by mechanical milling and solid-state reactions. Reproduced with permission from ref. 78. Copyright (2005) Wiley-VCH. (D) SEM images of the 70Li₂S·30P₂S₅ glass-ceramic material from a cold-pressed sample and the heat-treated sample at 280 °C and their corresponding EIS spectra. Reproduced with permission from ref. 79. Copyright (2014) The Royal Society of Chemistry. (E) Arrhenius plot of ionic conductivity of Li₄SnS₄ and As-doped Li₄SnS₄ with various molar ratios of As : Sn. Reproduced with permission from ref. 98. Copyright (2014) Royal Society of Chemistry. (F) Schematic of the intercalation process with partial Ag⁺ substituted by Li⁺, resulting in fast ionic conductivity at room temperature and temperature-dependent ionic conductivity of LiₓAg₁₋ₓCrS₂ crystals. Reproduced with permission from ref. 140. Copyright (2020) American Chemical Society.

were also performed on $Li_5PS_4X_2$ (X = Cl, Br, or I), which showed Li-ion conductivities similar to those of Li_6PS_5Cl and Li_6PS_5Br, suggesting that the $Li_5PS_4X_2$ compounds are interesting new compositions for SEs.[163] Recently, it was revealed that lithium halides can enhance the electrochemical stability of solid-state sulfide electrolytes against metallic lithium anodes.[165] As demonstrated by E. Rangasamy et al., the inclusion of I also creates stability with the metallic Li anode while simultaneously enhancing the interfacial kinetics and ionic conductivity.[120] Recently, H. Kim et al. innovatively synthesized a series of superionic halogen-rich Li-argyrodites using ultimate-energy mechanical alloying (UMA) and rapid thermal annealing (RTA) methods (Fig. 5D), in which they found $Li_{5.5}PS_{4.5}Cl_{1.5}$ exhibited the highest Li-ion conductivity among Li-argyrodites reported so far of 10.2 mS cm⁻¹ at room temperature (cold-pressed pellets). Compared to LGPS-type SEs, lithium argyrodites are easier to be synthesized from liquid phase, which is good for size and morphology control and interfacial solid–solid contact.[65,131,166–168] However, the ionic conductivity of SEs synthesized by liquid methods is generally lower than conventional solid-state sintering, as reviewed by M. Tatsumisago's research group[22,65]

1.2.3 Pseudo-quaternary sulfide electrolytes. To continue improving ionic conductivity and air-and-moisture stability of

SEs, pseudo-quaternary SEs have been a focus of development in recent years. In 2016, R. Kanno et al. reported a fast lithium superionic conductor $Li_{9.54}Si_{1.74}P_{1.44}S_{11.7}Cl_{0.3}$, which displays three-dimensional (3D) conduction pathways (1D along the c axis + 2D in the ab plane) (Fig. 6A). The high conductivity of $Li_{9.54}Si_{1.74}P_{1.44}S_{11.7}Cl_{0.3}$ is as high as 25 mS cm⁻¹ (Fig. 6B).[169] Fig. 6C shows a comparison of ionic conductivity between typical pseudo-binary, pseudo-ternary, and pseudo-quaternary SEs. Generally, the ionic conductivity of pseudo-quaternary SEs is higher than the other two even with the same lattice structure. Furthermore, the pseudo-quaternary SEs not only show higher ionic conductivity but also much-improved air stability. Our group developed a series of Sb-doped LGPS, which not only exhibit a high ionic conductivity (18 mS cm⁻¹) but also excellent air-stability (Fig. 6D). The softer acidity of Sb compared to P also ensures strong covalent bonding with S in $Li_{10}Ge(P_{1-x}Sb_x)_2S_1$, which improves the air stability of SEs.[93] Even after exposing to 1–3% humidity environment, $Li_{10}Ge(P_{1-x}Sb_x)_2S_{12}$ exhibited high ionic conductivities of 12.1–15.7 mS cm⁻¹. Furthermore, we also reported Sn(ɪv) substitution for P(v) in argyrodite sulfide Li_6PS_5I (LPSI) SSEs. Benefiting from the strong Sn–S bonding in Sn-substituted electrolytes, the LPSI-20Sn electrolyte shows excellent structural stability and improved air stability after exposure to O₂ and moisture.[84]
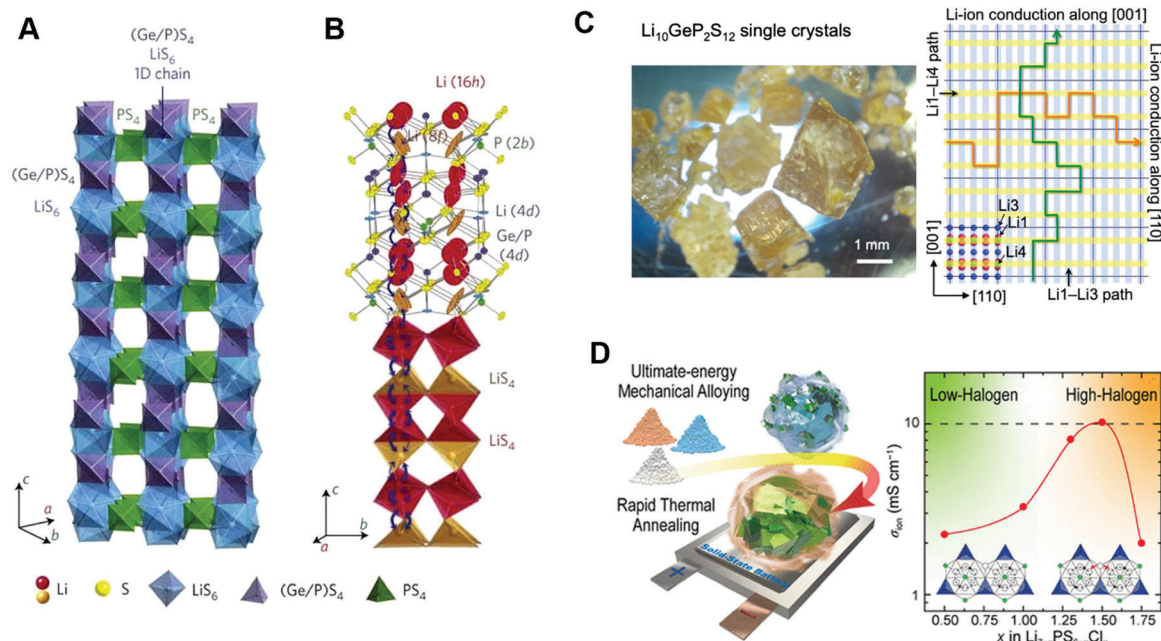
Fig. 5 (A) Framework structure of $Li_{10}GeP_2S_{12}$ and (B) conduction pathways of lithium ions. Zigzag conduction pathways along the c axis are indicated by arrows. Lithium ions in the LiS_4 tetrahedra (16h site) and LiS_4 tetrahedra (8f site) participate in ionic conduction. Reproduced with permission from ref. 73. Copyright (2011) Nature Publishing Group. (C) Photograph of typical LGPS crystals of a few millimeters in size and schematic drawing illustrating the possible conducting paths of Li ions in LGPS. Reproduced with permission from ref. 77. Copyright (2019) American Chemical Society. (D) Schematic images of one-pot crystallization using the ultimate-energy mechanical alloying and rapid thermal annealing (left) and ionic conductivity of $Li_{7-x}PS_{6-x}Cl_x$ (x = 0.50, 1.00, 1.25, 1.50, and 1.75). Reproduced with permission from ref. 85. Copyright (2020) American Chemical Society.
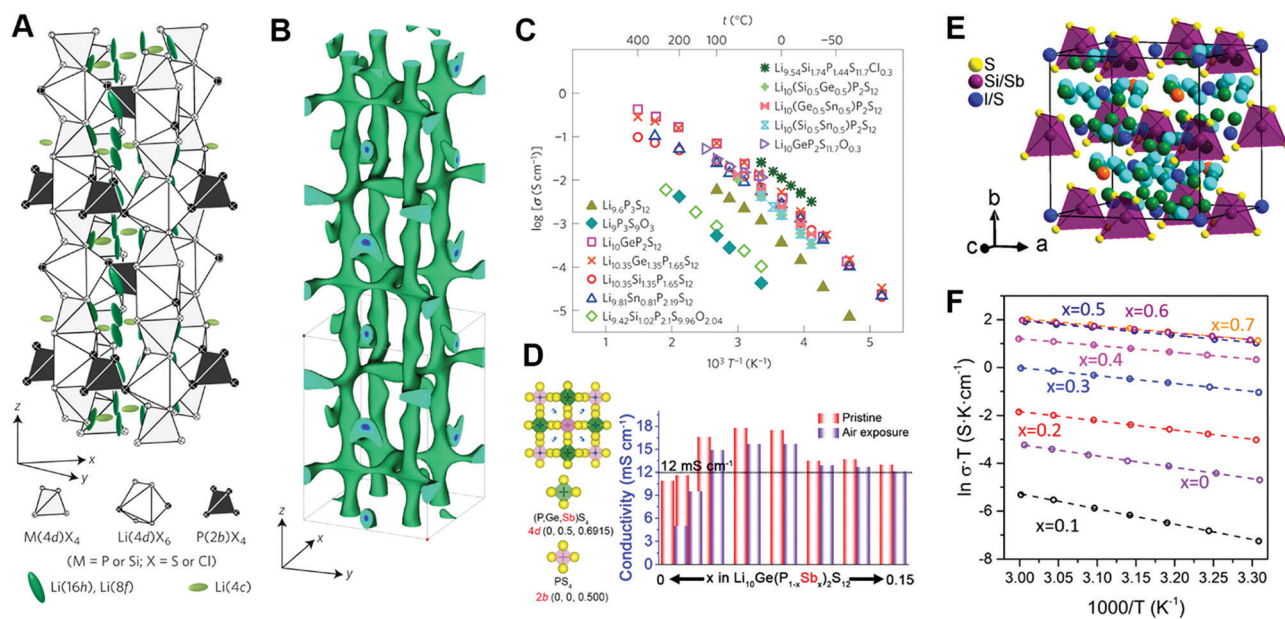
Fig. 6 (A) Crystal structure of $Li_{9.54}Si_{1.74}P_{1.44}S_{11.7}Cl_{0.3}$ and (B) nuclear distributions of Li atoms in $Li_{9.54}Si_{1.74}P_{1.44}S_{11.7}Cl_{0.3}$ at 25 °C.[15] (C) Arrhenius conductivity plots for the LGPS family and $Li_{9.6}P_3S_{12}$ and $Li_{9.54}Si_{1.74}P_{1.44}S_{11.7}Cl_{0.3}$. Reproduced with permission from ref. 15. Copyright (2016) Nature Publishing Group. (D) The ionic conductivity of Sb-doped $Li_{10}GeP_2S_{12}$ before and after air exposure. Reproduced with permission from ref. 93. Copyright (2020) American Chemical Society. (E) Crystal structure of $Li_{6.7}Si_{0.7}Sb_{0.3}S_5I$ from powder neutron diffraction at 300 K.[86] (F) Arrhenius plots of the conductivity values for $Li_{6+x}Si_xSb_{1-x}S_5I$ in the temperature range from 30 °C to 60 °C. Reproduced with permission from ref. 86. Copyright (2019) American Chemical Society.

In addition, L. Nazar and her colleagues reported a new family of argyrodite lithium superionic conductors, $Li_{6+x}M_xSb_{1-x}S_5I$ (M = Si, Ge, Sn) (Fig. 6E), which exhibited a room temperature ionic conductivity of 14.8 mS cm^{-1}, After eliminating grain

This journal is © The Royal Society of Chemistry 2021

Energy Environ. Sci., 2021, **14**, 2577–2619 | **2585**

boundary by hot pressing, the ionic conductivity of $Li_{6.6}Si_{0.6}Sb_{0.4}S_5I$ was as high as 24 mS cm^{-1} (Fig. 6F).[86] The high ionic conductivity is attributed to enhanced Li$^+$ cation site disorder that was induced by Si-substitution. Furthermore, L. Nazar and her co-authors also developed a series of $Li_2S–B_2S_3–SiO_2–LiI$ quaternary SEs that also were reported with high ionic conductivity of 2.1 mS cm^{-1}.[122]

In this section, recent progress of typical pseudo-binary, pseudo-ternary, and pseudo-quaternary SEs have been summarized. The ionic conductivity of SEs has been remarkably improved to 10^{-2} S cm^{-1} through either tuning the structure by doping (or substitution) or changing the stoichiometric ratio. The high ionic conductivity is even higher than that of traditional organic liquid electrolytes, undoubtedly meeting the requirements of practical solid-state batteries. Although significant improvement in the ionic conductivity has been made, continuous efforts are still required to further improve the air stability, widen the electrochemical windows, develop techniques for kilogram-scale production with low cost, and deepen the fundamental understanding of Li$^+$ transport mechanism in SEs.

1.3 Li$^+$ conduction mechanism of sulfide electrolytes

Understanding the Li$^+$ diffusion mechanism is crucial to design novel ionic conductors and optimize existing SEs for achieving high ionic conductivity as well as high air stability. To mathematically describe the Li$^+$ conduction in solid-state electrolytes, it is widely adopted to use the Nernst–Einstein relationship together with Fick's Diffusion law. The ionic conductivity of solid-state electrolytes can be described by the Nernst–Einstein equation.[170,171]

$$\sigma = \frac{\rho z^2 F^2}{k_B T} D(T) \qquad (1)$$

where ρ is the molar density of diffusing ions in the unit cell. F, k_B, and z are the Faraday constant, the Boltzmann constant, and the charge of lithium ions (+1 for Li+), respectively.

According to the Fick diffusion law, ion mobility in solid-state electrolytes can be described as follow.

$$D = D_0 e^{-E_a/k_B T} \qquad (2)$$

where D_0 is, E_a is the activation energy for lithium-ion hopping through the solid-state electrolytes. k_B is Boltzmann constant, T is the temperature in Kelvin.

Therefore, the ionic conductivity can be simply derived as:

$$\sigma = \frac{A_0}{T} e^{-E_a/k_B T} \qquad (3)$$

where A_0 is the pre-exponential factor, which combines molar density and other factors and constants mentioned above.

Based on mathematical analysis, it is easy to understand that the ionic conductivity is mainly determined by active Li$^+$ concentration and activation energy for Li$^+$ transport in the inorganic crystal framework. The lithium-ion concentration in solid-state electrolytes is strongly correlated with point defects in the crystal structure. Fig. 7A shows four kinds of point defects including vacancies, interstitials, Frenkel defects, and Schottky defects. The point defects decide the type and concentration of carriers, thus influencing the ionic conductivity of solid-state electrolytes.[172] Besides, the lithium-ion diffusion type in the crystal structure is also crucial for the ionic conductivity of solid-state electrolytes. In general, the ion-diffusion types include (i) interstitial hopping directly between adjacent sites; (ii) interstitial knock-off in which the migrating interstitial ion continuously displaces a neighboring ion, and (iii) direct vacancy hopping (coupled with carrier migration) (Fig. 7B).[173]

To design a fast ionic conductor, several criteria should be fulfilled:[174] (i) stable anion frameworks that possess weak interactions with mobile carriers; (ii) continuous diffusion pathways built with interconnected vacancies and interstitial sites. The neighboring sites should have a low migration barrier energy for ion hopping, and (iii) suitable conduction channels available for mobile ions with disordered sublattices to fit through.

The activation energy of lithium ions is strongly associated with the crystal structure of solid-state electrolytes. The crystal structure of solid-state electrolytes consists of immobile anion frameworks and the Li-ion sublattice. The interaction between Li-ions and immobile anion frameworks has a great effect on the Li-ion activation energy (lithium-ion mobility). Also, the spatial arrangement of immobile anion frameworks determines the lithium-ion pathways within ISEs. Therefore, crystal structural frameworks with a low energy barrier for lithium-ion transport are highly preferred for realizing high ionic conductivity. For example, Wang *et al.* proposed that body-centered cubic anionic frameworks allow for direct hops between adjacent tetrahedral sites with low activation energy (E_a) and do not require tetrahedral-octahedral hops with high activation energy (Fig. 7C).[175] Indeed, this body-centered cubic arrangement of anions is widely present in fast ion conductors, *e.g.* $Li_{10}GeP_2S_{12}$ and $Li_7P_3S_{11}$. More interestingly, Y. Mo *et al.* also proposed a new ion migration mechanism: a concerted migration of multiple ions with low energy barriers, will exhibit a much lower activation energy barrier than single-ion migration (Fig. 7D). This new mechanism has been widely adopted in lots of newly-discovered SEs.[86]

Based on these understandings, several strategies have been proposed to further improve ionic conductivity. The most effective strategy is doping or substitution. Doping with higher-valence cations can create cation vacancy or anion interstitials while doping with lower-valence cations can create cation interstitials or anion vacancies. In addition, site disorder also has a positive effect on the ionic conductivity of SE.[32,177,178] The second strategy is to introduce large cations to broaden the ion transport challenges. For example, replacing S^{2-} with larger Se^{2-} in Li_3PS_4 would not only induce point defects and interstitial ions but also broaden channels for lithium-ion transport, which may greatly improve the ionic conductivity of the solid electrolyte.[179] These fundamental theories could serve as a foundation to further improve the ionic conductivity of SEs.

2586 | *Energy Environ. Sci.*, 2021, **14**, 2577–2619

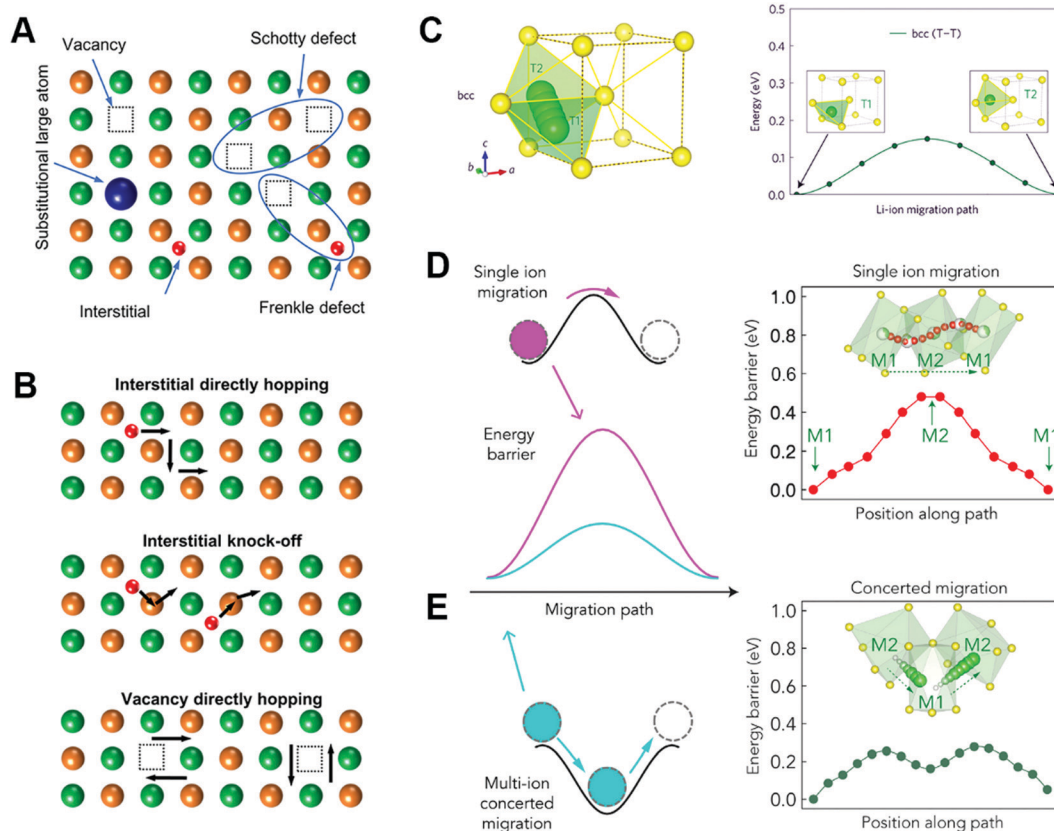This journal is © The Royal Society of Chemistry 2021

Fig. 7 Schematic representation of (A) point defects and (B) ion migration mechanisms. (C) Li-Ion migration path (left panels) and calculated energy path (right panels) in the bcc sulfur framework. Reproduction with permission from ref. 175. Copyright (2015) Nature Publishing Group. (D and E) Illustration of energy profiles for single-ion migration (pink) *versus* multiple-ion concerted migration (blue). (right) Energy landscape of concerted migration (upper) and the energy barrier of single Li$^+$ migration (lower) in LGPS. Reproduced with permission from ref. 176. Copyright (2017) Nature Publishing Group.

2. Chemical and electrochemical stability of sulfide electrolytes

2.1 Chemical stability of sulfide electrolytes

SEs are generally highly sensitive to moisture, generating harmful H_2S. For this reason, SEs must be handled in an inert gas atmosphere, which increases their cost for practical application. Recently, Y. Mo's group performed systematic thermodynamic analyses on the moisture stability of SE, which can serve as a guideline for designing air-stable SEs.[180]

Over the past years, three promising strategies have been demonstrated to improve air stability (Fig. 8), including metal oxide absorption, hard and soft acids and bases (HSAB) theory-guided doping, and core–shell nanostructure design. The first approach is to mix metal oxides with SEs to reduce H_2S generation from SEs. Metal oxides have a large negative value of Gibbs energy change (ΔG) for the following reaction: $M_xO_y + H_2S \rightarrow M_xS_y + H_2O$, thus absorbing H_2S or bringing about the acid–base reaction with H_2S. The ball-milled composites of the $75Li_2S\cdot25P_2S_5$ glass and one of the metal oxides (such as Fe_2O_3, ZnO, and Bi_2O_3) effectively suppressed the H_2S gas generation after the storage of the composites in the air (Fig. 8A and B).[181] T. Ohtomo and his co-workers demonstrated that the addition of x FeS to $(1 - x)$ $(0.75Li_2S\cdot0.25P_2S_5)$ was able to suppress the

generation of H_2S gas.[182] The increase in the amount of FeS in xFeS$\cdot(1 - x)$ $(0.75Li_2S\cdot0.25P_2S_5)$ linearly decreases the generation of H_2S from SEs, with the optimal mole content of FeS in $0.75Li_2S\cdot0.25P_2S_5$ found to be 40%. However, simply mixing metal oxides (more metal sulfides) with SEs generally decreases the high ionic conductivity of SEs.

The second approach is elemental substitution (or doping) based on the HSAB theory[183–185] in which hard acids react preferentially with hard bases while soft acids are more prone to react with soft bases.[98] Following this strategy, C. Liang *et al.* demonstrated that substituting tin with arsenic in Li_4SnS_4 ($Li_{3.833}Sn_{0.833}As_{0.166}S_4$) provides both a high ionic conductivity of 1.39×10^{-3} S cm^{-1} at room temperature and outstanding chemical stability to water. Impressively, after exposure to humid air, the change in ionic conductivity of $Li_{3.833}Sn_{0.833}As_{0.166}S_4$ was negligible compared with that of β-Li_3PS_4.[98] The excellent air stability was explained by the soft acids (*e.g.* tin and arsenic) preferentially reacting with soft bases (*i.e.* sulfur) rather than with hard acids (*i.e.* oxygen). Similarly, Liang and co-authors also demonstrated air-stable Na_3SbS_4 synthesized by both solid-state sintering and solution-based processes.[186,187] Our group reported that Sb-doped LGPS can significantly suppress H_2S release, as shown in Fig. 8C. Y-K Jung *et al.* reported air-stable Sb-substituted Li_4SnS_4 with high ionic conductivity of
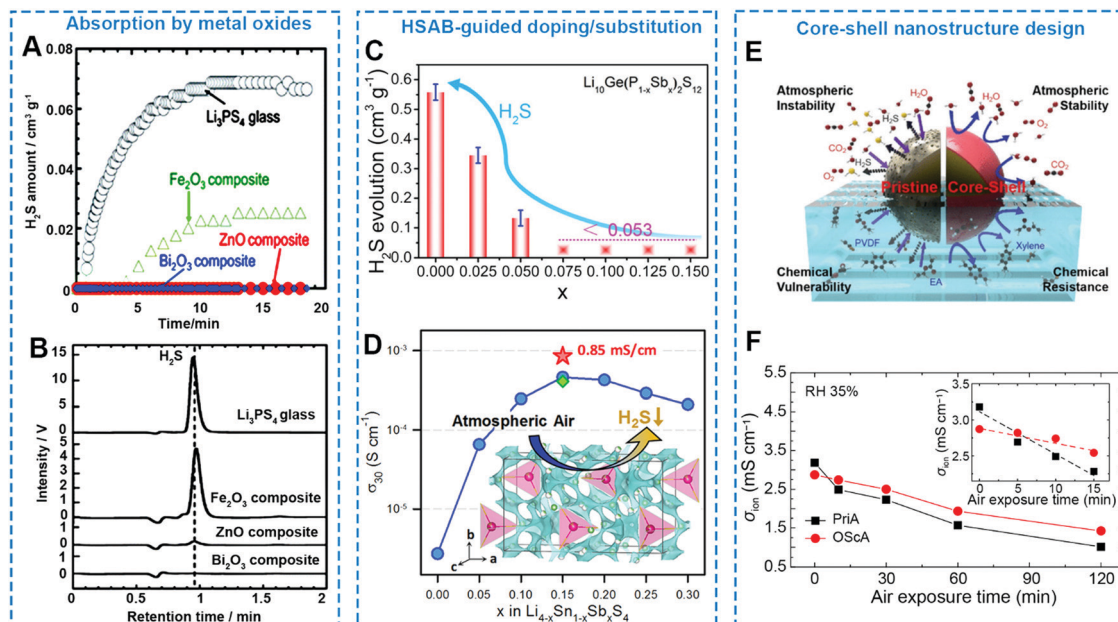
This journal is © The Royal Society of Chemistry 2021

Energy Environ. Sci., 2021, **14**, 2577–2619 | **2587**

Fig. 8 (A) H_2S amount as a function of exposure time to air and (B) gas chromatograms for the $90Li_3PS_4 \cdot 10M_xO_y$ (M_xO_y: ZnO, Fe_2O_3, and Bi_2O_3) composites and the Li_3PS_4 glass. Reproduced with permission from ref. 181. Copyright (2013) Royal Society of Chemistry. (C) Amount of H_2S gas released from commercial $Li_{10}GeP_2S_{12}$ and synthesized $Li_{10}Ge(P_xSb_{1-x})_2S_{12}$. Reproduced with permission from ref. 93. Copyright (2020) American Chemical Society. (D) Sb-Substituted Li_4SnS_4 showing a high Li^+ conductivity of 0.85 mS cm^{-1} at 30 °C and excellent dry-air stability as well as negligible H_2S evolution. Reproduced with permission from ref. 188. Copyright (2020) Elsevier. (E) Illustration of air stability and chemical vulnerability between pristine and core−shell SE particles.[193] (F) Variations in the ionic conductivity of SE with 35% relative humidity condition at 25 °C and air exposure time up to 120 min. Reproduced with permission from ref. 193. Copyright (2020) American Chemical Society.

0.85 mS cm^{-1} and negligible H_2S release in atmospheric air (Fig. 8D).[188] Moreover, Sn-doped Li_6PS_5I also demonstrated much-improved air stability. Oxygen or nitrogen substitution in SEs was also found to enhance their chemical stability in the ambient atmosphere.[189] X. Xu *et al.* demonstrated that Zn and O co-doped Li_3PS_4 glass-ceramic ($Li_{3.06}P_{0.98}Zn_{0.02}S_{3.98}O_{0.02}$) exhibits excellent stability against humid air, lithium metal, and chlorobenzene solvent.[185] L. Zhang *et al.* reported O-doped Li_6PS_5Br which exhibited excellent dendrite suppression capability, superior electrochemical and chemical stability against Li metal as well as high voltage oxide cathodes, and good air stability.[190] Besides, recent studies also suggest that lithium halides have the potential to increase the stability against moisture,[191] such as Li_3PS_4–LiI.[192]

The third strategy is the core–shell nanostructure design of SEs, in which a functional nanolayer is coated on the SE particles. As long as the outer layer does not block the Li^+ diffusion between SE particles, both high ionic conductivity and good air-stability can be achieved. Recently, a core–shell structured SEs with a stable oxysulfide nanolayer was reported to show a high ionic conductivity of 2.5 mS cm^{-1} after 30 min of air exposure (Fig. 8E and F). Besides, this core–shell SE also demonstrated high chemical resistivity in the wet casting process with various solvents.[193]

2.2 Electrochemical stability of sulfide electrolytes

Solid-state SEs are desired to pair with thin metallic lithium anodes and high-voltage cathodes, constituting high-energy-density ASSLBs.

Thus, a large electrochemical window of SEs is required to ensure the electrochemical stability of SEs during the charge/discharge process. In the past, the electrochemical stability window of SEs (such as LGPS, Li_2S–P_2S_5) was boasted to be 5 V *vs.* Li^+/Li, which is overestimated by the conventional experimental method using a Li metal/electrolyte/inert metal semi blocking electrode because of the limited contact area between the solid electrolyte and inert metal.[194] Based on theoretical calculation, the stable electrochemical window of $Li_{10}GeP_2S_{12}$ is only from 1.71–2.14 V *vs.* Li^+/Li, as displayed in Fig. 9A. The CV curves also show a reduction peak of 1.7 V and an oxidation peak of 2.1 V as shown in Fig. 9B and C, respectively, which is tested by a Li/electrolyte/electrolyte-carbon cell. Therefore, adding carbon additives to enhance the contact area between SE and conductive agents is more reliable to evaluate the intrinsic electrochemical windows than current Li/electrolyte/Pt semi-blocking electrodes.[194] Y. Mo *et al.* employed DFT calculations to examine the intrinsic electrochemical windows of SEs, which generally only stabilize between 1.7–2.1 V *vs.* Li^+/Li (Fig. 9D).[195] To improve the electrochemical windows of SEs, X. Li *et al.* designed a core–shell structured $Li_{9.54}Si_{1.74}P_{1.44}S_{11.7}Cl_{0.3}$ by controlling synthesis parameters and the consequent core–shell microstructural compositions (Fig. 9E).[196] The higher Si content on the shell results in a stable window of 0.7–3.1 V, which is much larger than the theoretical prediction (1.7–2.1 V).

Oxygen doping is demonstrated to be another effective way to improve the electrochemical stability of SEs.[190] R. Kanno *et al.* demonstrated that $Li_{9.42}Si_{1.02}P_{2.1}S_{9.96}O_{2.04}$ (LSiPSO)

2588 | *Energy Environ. Sci.*, 2021, **14**, 2577–2619

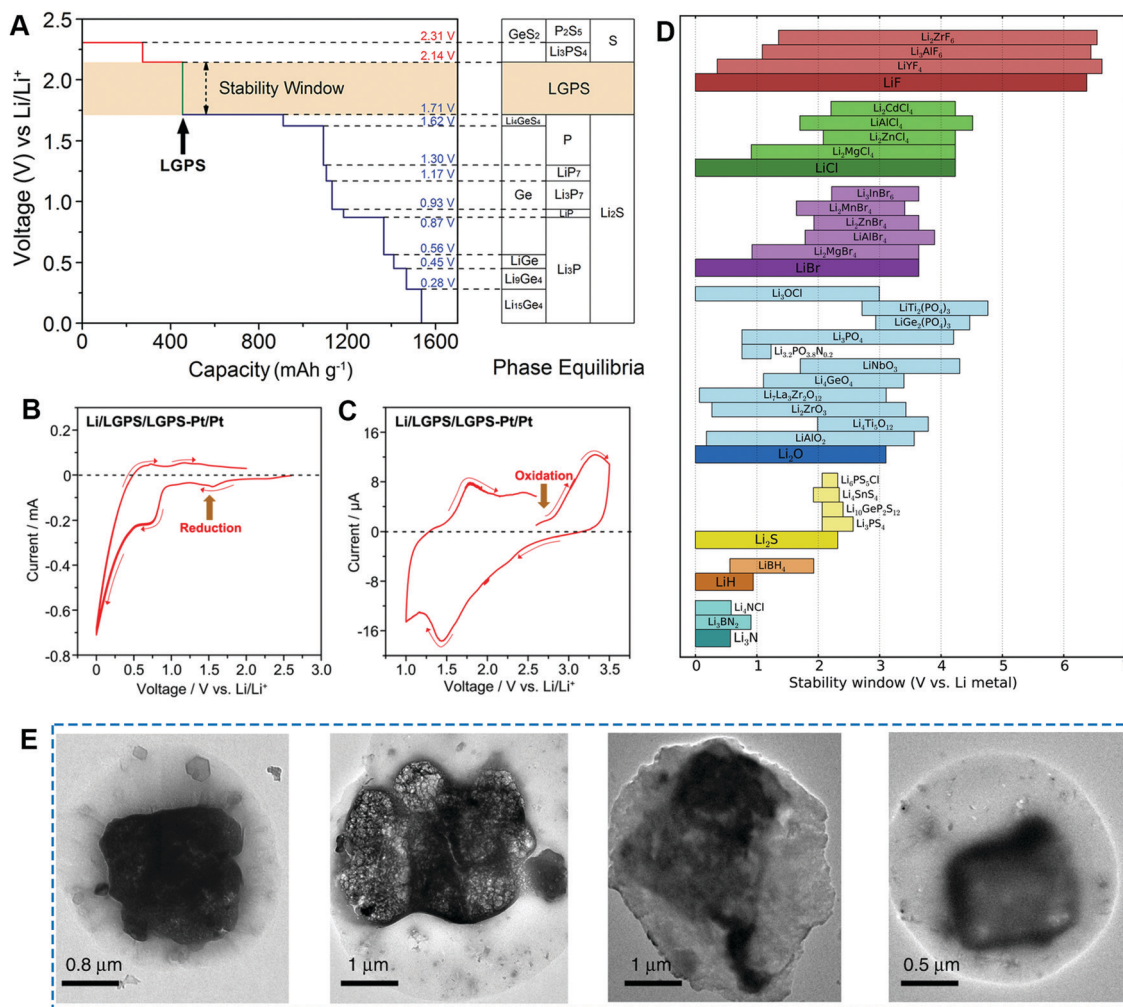This journal is © The Royal Society of Chemistry 2021

Fig. 9 (A) The first-principles calculation results of the voltage profile and phase equilibrium of LGPS solid electrolyte upon lithiation and delithiation.[194] Cyclic voltammetry of Li/LGPS-Pt/Pt semi-blocking electrode at a scan rate of 0.1 mV s^{-1} in the voltage range of 0–2.0 V (B) and 1.0–3.5 V (C). Reproduction with permission from ref. 194. Copyright (2016) Wiley-VCH. (D) Electrochemical stability ranges of various electrolyte materials grouped by anion, with corresponding binary materials for comparison. The high-voltage stability of these materials is determined primarily by the anion. Reproduced with permission from ref. 195. Copyright (2016) American Chemical Society. (E) TEM images of core−shell structured Li$_{9.54}$Si$_{1.74}$P$_{1.44}$S$_{11.7}$Cl$_{0.3}$ annealed at 450 °C, 460 °C, 480 °C, and 500 °C. Reproduced with permission from ref. 196. Copyright (2018) Nature Publishing Group.

exhibited an ionic conductivity as high as 3.2×10^{-4} S cm^{-1} at 298 K as well as high electrochemical stability to lithium metal.[197] Recently halide electrolytes have been revived due to their wide electrochemical windows compared to that of SEs and desirable ionic conductivity ($\sim$1 mS cm^{-1}),[33,198] which could be combined with SEs for developing all-solid-state lithium batteries.[35] To realize the high energy of ASSLBs that can compete with commercial LIBs, the electrochemical window of SEs should be further expanded to enable the use of lithium metal anodes and high-voltage cathodes.

To sum up, this section summarizes the progress of electrochemical and chemical stability of SEs. So far three strategies including metal oxide absorption, HSAB theory-guided doping or substitution, and core–shell structure design have been demonstrated to significantly improve the air stability of SEs. In addition, oxygen doping and interfacial nanostructure design have been proposed to widen the electrochemical

windows of SEs. However, some strategies (*i.e.* metal oxide absorption) are harmful to the ionic conductivity of SEs. Therefore, it is of vital importance to further improve the air stability and electrochemical windows with innovative and cost-effective strategies in the future without compromising the high ionic conductivity of SEs. Moreover, the in-depth understanding of chemical and electrochemical stability mechanisms is also crucial and meaningful.

3. Interfacial challenges and strategies of SE-based ASSLBs

The interface where the electrochemical reactions occur is the most critical part of the ASSLB.[199] However, the interface of ASSLBs suffers from great challenges that significantly prevent ASSLBs from commercialization. Fig. 10 schematically displays
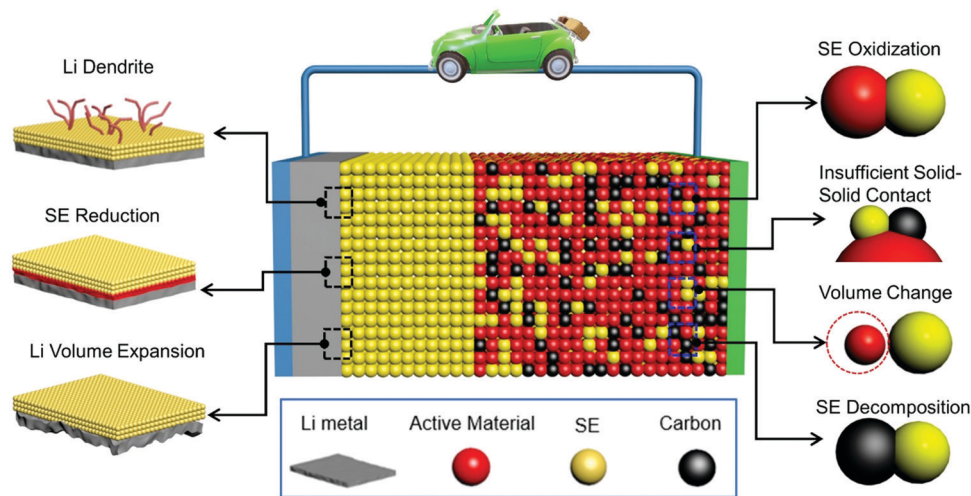
This journal is © The Royal Society of Chemistry 2021

Energy Environ. Sci., 2021, **14**, 2577–2619 | **2589**

Fig. 10 Schematic illustration of various interfacial challenges in cathode composites and Li/SE interface in SE-based ASSLBs.

the main challenges at the cathode and anode interface of ASSLBs, respectively. Major challenges at the cathode interface include interfacial reactions between transition metal oxides and SEs, the volume change of cathode materials, and detrimental decomposition reaction of SEs induced by carbon additives, which significantly depresses the electrochemical performance. At the anode interface, the lithium dendrite growth, SE reduction by lithium metal, as well as the infinite volume change of lithium metal are the most serious challenges.

It should be mentioned that the space charge effect at the cathode/SE interface has been broadly discussed in many previous review papers.[200,201] Recently, G. Cui et al. observed the lithium-ion accumulation in situ resulting from space charge effect at the $LiCoO_2/Li_6PS_5Cl$ interface using a differential phase contrast scanning transmission electron microscopy (DPC-STEM) technique.[202] Y. Namura et al. also observed the Li-ion space charge effect at Cu/oxide electrolyte interface using phase-shifting electron holography and spatially resolved electron energy-loss spectroscopy.[203] However, some studies suggested that the space charge effect between oxide cathodes and SEs is probably overstated.[61,204,205] To the best of our knowledge, the space charge effect exists at the oxide/SE interface,[200] but has less impact on electrochemical performance on ASSLBs than cathode interfacial reactions, the volume change of electrode materials, solid–solid ionic contact, and SE decomposition by carbon additives do.

3.1 Cathode interfacial challenges and corresponding strategies

3.1.1 Cathode interfacial reactions. Due to the narrow electrochemical windows, SEs are prone to be oxidized by oxide cathodes, especially at high voltages. Many previous investigations based on either first-principles calculation or experimental investigation have unveiled undesirable chemical reactions or elemental diffusions at the interface between oxide cathodes and SEs during the charge/discharge process.[206,207] A. Sakuda et al. first observed a 10 nm interfacial layer at the

interface between $LiCoO_2$ and $Li_2S–P_2S_5$ by transmission electron microscopy (TEM), which was ascribed to the elemental diffusion of Co, P, and S.[208,209] Y. Tateyama et al. theoretically confirmed that the mixing of Co and P at the $LiCoO_2/\beta-Li_3PS_4$ interface is energetically preferable via first-principles calculations (Fig. 11A).[206] A. Banerjee et al. identified the interfacial products of Ni_3S_4, LiCl, Li_3PO_4, and oxidized LPSCl from the spontaneous chemical reaction between $LiNi_{0.85}Co_{0.1}Al_{0.05}O_2$ (NCA) and Li_6PS_5Cl (LPSCl) by various advanced characterization tools and first-principles calculations to probe the interfacial phenomenon between the solid electrolyte LPSCl and a high-voltage cathode (NCA) (Fig. 11A).[210] Moreover, in situ X-ray photoelectron spectroscopy (XPS) has been widely adopted to characterize the interfacial reactions between the electrode materials and sulfide electrolytes.[209,211,212] It is broadly accepted that SEs are oxidized to elemental S, sulfites, phosphates, and high-oxidation-state P_2S_x compounds after cycling.[211,213] These highly insulative interphases dramatically hinder the Li^+ transport across the interface. By in situ X-ray absorption near-edge spectroscopy (XANES) combined with high-resolution transmission electron microscopy (HRTEM), our group recently demonstrated a metastable intermediate state of SEs at high voltage and discovered parasitic reactions with Ni-rich cathodes during the charge/discharge process which leads to an interfacial structural reconstruction of layered cathode materials.[214]

To suppress the significant interfacial reactions, a buffer layer is generally introduced between oxide cathodes and SEs, aiming at preventing interfacial reactions.[209,223–226] So far, both lithium-ion conducting coating layers (e.g. $LiNbO_3$,[227] $Li_4Ti_5O_{12}$,[228] and Li_2SiO_3,[208,229] Li_2ZrO_3[230]) and dielectric oxides (e.g. Al_2O_3[231]) are reported to dramatically reduce the cathodic interfacial resistance. By first-principles calculation, Y. Mo et al. suggested that Li–Ta–O, Li–Nb–O, Li–Si–O, Li–Ti–O, and Li–P–O possess a wide electrochemical window (Fig. 11B), meaning that these coating materials will improve stability at the electrode/electrolyte interface during cycling.[215] Experimentally, these coating
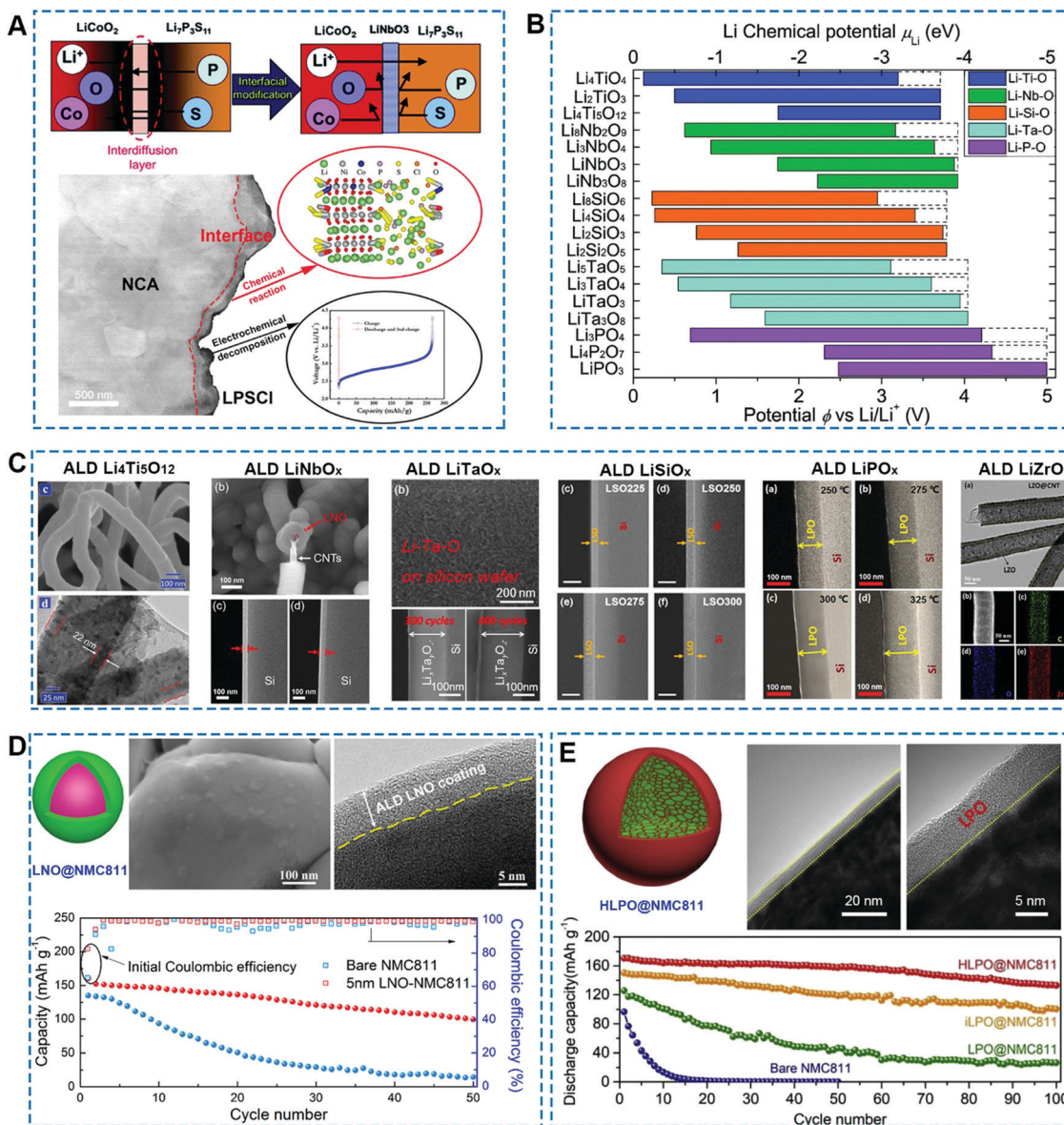
Fig. 11 (A) Schematic of interfacial elemental interdiffusion and chemical reactions and electrochemical decomposition. Reproduced with permission from ref. 210. Copyright (2019) American Chemical Society. (B) The electrochemical window of the proposed and previously demonstrated coating layer materials applied between SEs and cathode materials. The dashed line marks the equilibrium voltage to fully delithiate the materials. Reproduced with permission from ref. 215. Copyright (2016) The Royal Society of Chemistry. (C) The ALD deposition of various coating materials for interface engineering, including $Li_4Ti_5O_{12}$, reproduced with permission from ref. 216. Copyright (2013) The Royal Society of Chemistry. $LiNbO_x$, reproduced with permission from ref. 217. Copyright (2018) American Chemical Society. $LiTaO_x$, reproduced with permission from ref. 218. Copyright (2013) American Chemical Society. $LiSiO_x$, reproduced with permission from ref. 219. Copyright (2017) American Chemical Society. $LiPO_x$, reproduced with permission from ref. 220. Copyright (2014) IOP Publishing LTD and $LiZrO_x$, reproduced with permission from ref. 221. Copyright (2020) Elsevier. (D) $LiNbO_3$ coating on NMC811 particles by atomic layer deposition. Reproduced with permission from ref. 213 and 214. Copyright (2019) American Chemical Society. (E) Dual-functional interface design: Li_3PO_4 coated on polycrystalline NMC811. Reproduced with permission from ref. 222. Copyright (2020) Elsevier.

materials have been broadly verified and synthesized by sol–gel methods or spray coating.[61] The conventional synthesis techniques are very challenging when trying to control the thickness and uniformity of interfacial coatings. As a remedy, our group has successfully synthesized Li–Nb–O,[217] Li–Si–O,[219] Li–Ta–O,[218] Li–P–O,[220] Li–Ti–O,[216] and Li–Zr–O[221] by atomic layer deposition (ALD), which allow us to coat these promising interfacial materials on various cathodes conformally and

precisely (Fig. 11C). As demonstrated in our recent work, 5 nm $LiNbO_3$ was conformably deposited on $LiCoO_2$ particles by ALD, which effectively prevented interfacial reactions between LGPS and LCO (Fig. 11D).[213] Recently, ionically conductive Li–Zr–O with a thickness of 5 nm was coated on $LiCoO_2$ (LCO) by ALD, successfully inhibiting interfacial reactions between LCO and Li_6PS_5Cl.[221] Interestingly, G. Ceder et al. predicted that $LiPO_3$ possesses a wide electrochemical window,

This journal is © The Royal Society of Chemistry 2021

Energy Environ. Sci., 2021, **14**, 2577–2619 | **2591**

which can be a good coating material for high-voltage cathodes, such as $LiNi_{0.5}Mn_{1.5}O_3$, $LiCoPO_4$.[232] Besides, Li_3PO_4 can also serve as a fast ion conductor. Diffusion of Li_3PO_4 into polycrystalline Ni-rich layered cathode materials not only suppresses the grain boundary inside Ni-rich particles but also prevents the side reactions and consequent interfacial structure degradation as well as particle cracking (Fig. 11E).[233] Recently, we also revealed that improving the ionic conductivity of coating materials can significantly boost the interfacial ionic transport kinetics in SE-based ASSLBs.[234] Similarly, H. Zhu's group coated a thin layer of amorphous $Li_{0.35}La_{0.5}Sr_{0.05}TiO_3$ (LLSTO) with high ionic conductivity of 8.4×10^{-5} S cm^{-1} on $LiNi_{1/3}Mn_{1/3}Co_{1/3}O_2$ (NMC111). The resultant LLSTO@NMC111 cathodes exhibited an outstanding capacity of 107 mA h g^{-1} and was kept stable for 850 cycles with a high capacity retention of 91.5% at C/3.[235] Furthermore, we also coated LCO with the novel Li_3InCl_6 and obtained high ionic conductivity of 1.5×10^{-3} S cm^{-1}. LIC@LCO composites can considerably improve the rate-performance of ASSLBs, which is even comparable with that of conventional LIBs based on liquid electrolytes.[40] These experimental results unveiled that interfacial Li$^+$ transport is the most critical step in improving ASSLBs and hence, improving the ionic conductivity of interfacial materials can facilitate better interfacial Li$^+$ transport kinetics.

Apart from rationally designing interfacial coatings, synthesizing solid-state electrolytes with high voltage stability is an alternative and effective solution. Recently, Li_3YCl_6 and Li_3YBr_6 were reported to exhibit not only high ionic conductivity (1 mS cm^{-1}) but also high electrochemical stability.[30,33,34,236–239] Using Li_3YCl_6 solid-state electrolytes, LCO cathode without surface coatings delivered a high initial coulombic efficiency of 94%. Due to these advantages, lots of halide electrolytes, particularly high Li$^+$-conductive Li_3InCl_6,[240] Li_3ScCl_6,[39] $Li_{2.5}Zr_{0.5}Y_{0.5}Cl_6$,[198] $Li_{2.5}Zr_{0.5}Er_{0.5}Cl_6$,[198] Li_3ErCl_6,[32] Li_3LaI_6,[241] $Li_3Y(Br_3Cl_3)$,[130] $Na_{3−x}Er_{1−x}Zr_xCl_6$[31] have quickly developed within the recent two years. These highly ion-conductive halide electrolytes can be used as ionic additives in the cathode composite without any extra surface coating layers, enabling ultra-fast interfacial lithium-ion transport. We do believe that combining the advantages of SEs and halide electrolytes could catalyze the progress of ASSLBs soon.

3.1.2 Solid–solid ionic contact. To achieve the comparable electrochemical performance of ASSLBs with that of traditional liquid cells, sufficient solid–solid ionic contact between active materials and SEs must be guaranteed. To this end, various soluble-processable SEs have been developed over past years by suspension solution[186,242–247] such as Li_3PS_4,[242,248–250] $Li_7P_3S_{11}$,[134,135,251] $Li_{10}GeP_2S_{12}$,[252] Li_6PS_5Cl,[253,254] Li_6PS_5Br,[255] Li_6PS_5I,[167] LiI–Li_4SnS_4,[244] and $Li_{6+x}P_{1−x}M_xS_5I$ (M = Ge, Sn).[243] Recently, several comprehensive reviews about the liquid-phase synthesis of solid-state SEs have been published.[22,256] SEs can be used to coat on electrode material surface, thus increasing the solid–solid ionic contact and boosting Li-ion flux in the cathode composites (Fig. 12B).[213,244,253,257]
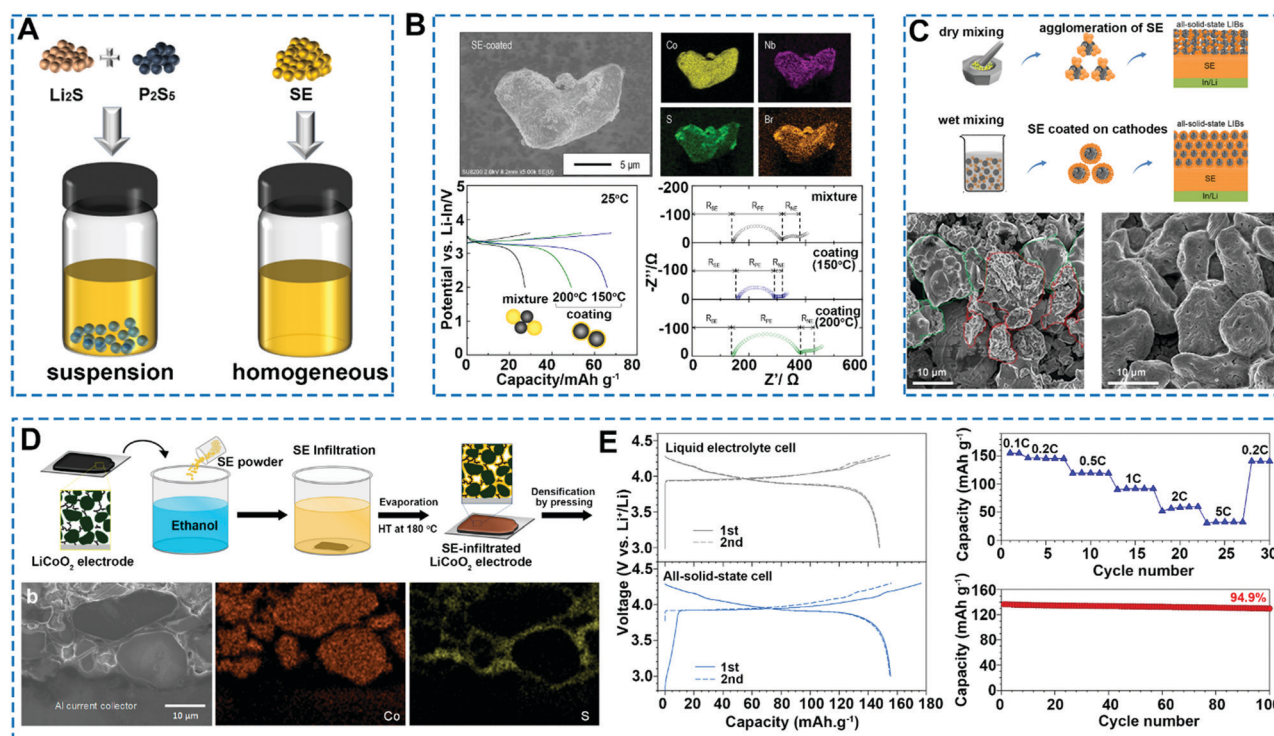
Fig. 12 (A) Schematic of liquid-phase synthesis of sulfide electrolytes. (B) Scanning electron microscopy and energy dispersive X-ray analysis mapping (Co, P, S, and Br) images of a $LiCoO_2$ particle coated with the Li_6PS_5Br solid electrolyte. Reproduced with permission from ref. 253. Copyright (2015) Elsevier. (C) Comparison between dry mixing and wet-chemistry mixing for cathode composite preparation. Reproduced with permission from ref. 213. Copyright (2019) Wiley-VCH. (D) Electrode infiltration using soluble sulfide electrolytes.[243] (E) Electrochemical performance of the SE-infiltrated electrodes. Reproduced with permission from ref. 243. Copyright (2020) American Chemical Society.

2592 | Energy Environ. Sci., 2021, **14**, 2577–2619

This journal is © The Royal Society of Chemistry 2021

Our group also systematically compared dry mixing and wet mixing methods to prepare the cathode composites, demonstrating that intimate solid–solid contact between cathode materials and SEs is required to realize a comparable electrochemical performance to that of liquid cells (Fig. 12C). Furthermore, soluble SEs can be directly coated on conventional electrode-sheets. With densification by pressing, intimate solid–solid ionic contact between active materials and SEs can be realized. This approach is feasible for practical pouch cell fabrication.[246,257] As shown in Fig. 12D, soluble Li_6PS_5Cl were successfully infiltrated into an electrode-sheet with a homogeneous distribution. The charge and discharge curves of ASSLBs exhibited negligible polarization, high rate performance, and a capacity retention 94.9% after 100 cycles (Fig. 12E).[243] Soluble SEs also can be employed to fabricate ultra-thin solid electrolyte membranes,[258,259] which are pivotal for the high-energy-density all-solid-state lithium metal batteries.[260]

3.1.3 Volume change of cathode composites. The third challenge at the cathode/SE interface is the volume change from oxide materials during the charge/discharge process.[261] Unlike in liquid cells, in which the volume change cathode particles upon cycling can be accommodated by fluid liquid electrolytes, solid-state SEs cannot accommodate the volume change of cathode materials. Tasumisago *et al.* observed the void formation between LCO and SE after the charge–discharge process. The void increased with a high cut-off voltage of 4.6 V.[262] In 2017, J. Janek *et al.* disclosed that NCM-811 particles shrink during delithiation (charge) and lose contact with the SE (Fig. 13A–F). The contact loss accumulates with further cycles, which is one reason for the capacity decay in ASSLBs. Furthermore, they also monitored the internal pressure change of $LiCoO_2$/$Li_{10}GeP_2S_{12}$/In cells. As shown in Fig. 13G, the internal pressure increases almost linearly during charging and decreases during discharging. The observed pressure changes agree well with the charge–discharge curves, indicating that the SE-based ASSLB experiences volume expansion during charging, and compression during the discharge. At a higher C-rate, less capacity is obtained, which leads to a lower pressure change. The observed decrease in capacity correlates well with the decrease of pressure peaks with cycling, which is indicative of irreversible processes at the electrode/electrolyte interfaces and particle contact loss due to the "breathing" of the ASSLB (Fig. 13H). Focused ion beam-scanning electron microscope (FIB-SEM) tomography with the nanoscale resolution was used for 3D characterization of the composite electrode morphology before and after cycling. The development of voids and cracks near the cathode particles and significant contact loss between the cathode particles and solid electrolyte after cycling was found.[263]

To address the volume change of cathode composites, Y. Janek *et al.* proposed to blend two cathode composites that show inverse volume change trends. For example, LCO expands during charge but shrinks upon discharge (Fig. 13I). On the contrary, NMC-811 shrinks during charge and expands upon discharge (Fig. 13J). This reverse volume change profile allows them to be blended to realized overall lower nominal stress (Fig. 13K).[261] Apart from the blended cathode materials, adding external pressure also can suppress the volume change, thus improve the solid–solid contact between cathodes and SEs during the charge/discharge process.[265,266] Also, using some compatible polymer electrolytes or surface wetting additives can enhance the ionic conduction after volume change, which is a direction that should be further developed in future.

3.1.4 Detrimental side reactions induced by carbon additives. The fourth challenge at the cathode/SE interface is the SE decomposition caused by carbon additives.[267–274] For example, C. Wang *et al.* reported that when LGPS is mixed with a large amount of carbon (*i.e.* 25 wt%), LGPS will be seriously decomposed.[194] R. Kanno *et al.* also found that the acetylene black (AB)/LGPS composite exhibited a high oxidation current in the cyclic voltammetry (CV) test, which means LGPS decomposition continuously occurs at the LGPS/AB interface within cathode composites.[268] In more detail, J. Janek *et al.* found that carbon additives in the cathode composites facilitate SE decomposition, which is responsible for large interfacial resistance and capacity decay (Fig. 14A).[267] K. Kang *et al.* further compared the various conductive carbon agents in the cathode composite of SE-based ASSLBs. It is found that adding various conductive carbon agents in the cathode composites, regardless of their physical appearance, does not improve the kinetic performance of SE-based ASSLBs as expected, but instead will significantly promote the SE decomposition.[274] Meng's group investigated the reversible decomposition redox of Li_6PS_5Cl in Li–In|Li_6PS_5Cl|Li_6PS_5Cl–C cell. As tested by cyclic voltammetry (CV) Fig. 14B, a positive sweep yielded two oxidative peaks (1, 2) at 2.6 and 3.0 V, which corresponds to the oxidization of Li_6PS_5Cl to PS_4^{3-} and S and P_2S_5, respectively. The negative sweep showed two reductive peaks (3, 4) at 2.0 and 1.1 V, which is ascribed to the reduction of PS_4^{3-} and Li_2S and Li_3P, respectively.[269] All the experimental results consistently verified that carbon additives significantly increase the decomposition of SEs in ASSLBs. However, carbon additives are essential for constructing electronic pathways in the cathode composites. Therefore, optimally balancing or finding a suitable conductive agent with a minimal influence on SEs is pivotal for designing high-power-density ASSLBs.

Recently, a poly(3,4-ethylene dioxythiophene) (PEDOT) modification was designed as a semiconductive additive for cathode composites (cathode/SSE/carbon) to realize high-rate capability.[270] As shown in Fig. 14C, electrons act as the charge carrier in the CNTs as a metallic conductor, while PEDOT is a p-type semiconductor, meaning the charge carriers are holes. When PEDOT thin film is deposited on the surface of CNTs, a metal/p-type semiconductor contact interface is formed. The Fermi energy (EF) of CNTs is higher than that of PEDOT. To maintain the equilibrium of EF after contact, electrons have to flow from CNTs into PEDOT until the Fermi energies are finally equalized. As a result, the holes in the PEDOT are filled by the electrons, causing decreased PEDOT thin-film conductivity. Therefore, the conductivity of PEDOT modified CNTs is also decreased. As shown in Fig. 14D, PEDOT-modified CNT/LGPS exhibits a much lower oxidation current than bare CNT/LGPS, which is indicative of adopting semiconductive additive in the cathode composites effectively, which alleviates
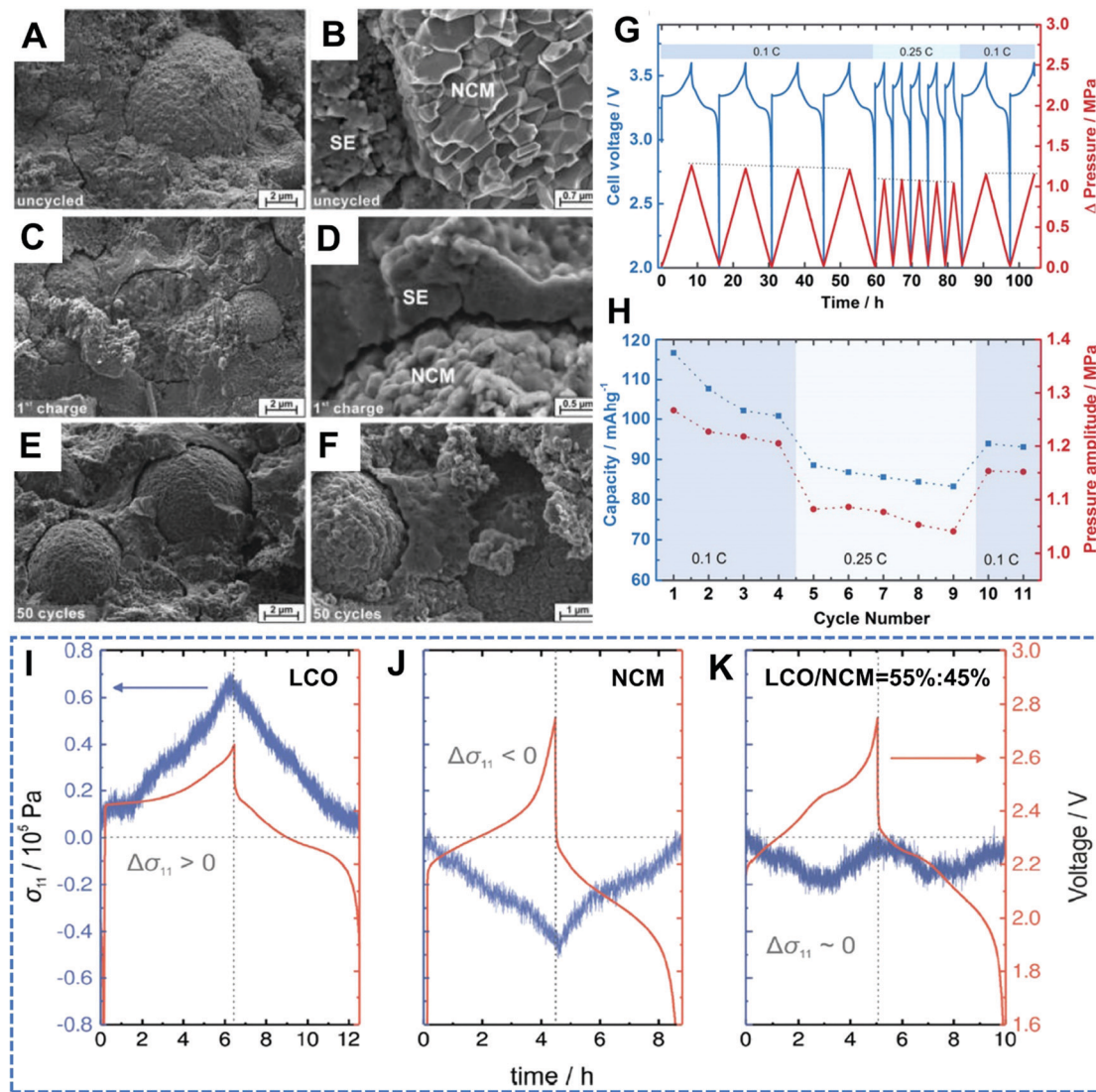
This journal is © The Royal Society of Chemistry 2021

Energy Environ. Sci., 2021, **14**, 2577–2619 | **2593**

Fig. 13 Volume change of cathode materials and its consequences in ASSLBs. Scanning electron micrographs of the cathode composite of NCM811 and β-Li₃PS₄ in a Li−In|β-Li₃PS₄|NCM-811/β-Li₃PS₄ cell: (A and B) before cycling. (C and D) After the first charge to 4.3 V vs. Li⁺/Li/at 0.1C. (E and F) After 50 cycles in the discharged state. Reproduced with permission from ref. 212. Copyright (2017) American Chemical Society. (G) Pressure change monitored during galvanostatic cycling (2.0−3.6 V vs. In/InLi) of a solid-state battery composed of In/Li₁₀GeP₂S₁₂/LiCoO₂ at 25 °C with a current density of 146 mA cm⁻² (corresponding to 0.1C) and 366 mA cm⁻² (corresponding to 0.25C). (H) Summarized capacity retention (blue) and pressure amplitude (red) with cycle numbers for the pressure monitored SE-based ASSLBs. Reproduced with permission from ref. 264. Copyright (2017) The Royal Society of Chemistry. Comparison of the stress response of LTO/SE|SE|CAM/SE using (I) LCO, (J) NCM-811, and (K) a blend of 55 : 45 wt% NCM-811 : LCO cathode composite. Reproduced with permission from ref. 261. Copyright (2018) The Royal Society of Chemistry.

the decomposition of SEs and the side reactions with cathode particles. More efforts are still required in this direction, particularly when using high-loading cathode composites in real pouch cells.

To sum up, the cathode interface between SEs and high-voltage metal oxide cathodes suffers from many challenges, such as significant interfacial reactions, poor solid–solid ionic contact, volume change, and SE decomposition by conductive agents. First, the interfacial protection layer is indispensable to prevent interfacial reactions because of the narrow electrochemical windows of SEs. Both the electrochemical stability and ionic conductivity of the interfacial protection layer are

responsible for the high performance of ASSLBs. Second, intimate solid–solid ionic contact is a prerequisite for the full utilization of active materials in ASSLBs. It was demonstrated that soluble SEs with decent ionic conductivity are very promising for realizing intimate solid–solid ionic contact in ASSLBs. Third, the non-negligible volume change of cathode materials during the charge/discharge process is harmful to the long-term cycling stability of SE-based ASSLBs, particularly with the high-loading cathode materials (>20 mg cm⁻²). Therefore, apart from external pressure to mitigate the volume change, innovative strategies such as interfacial wetting agents should be developed to accommodate the volume change in the
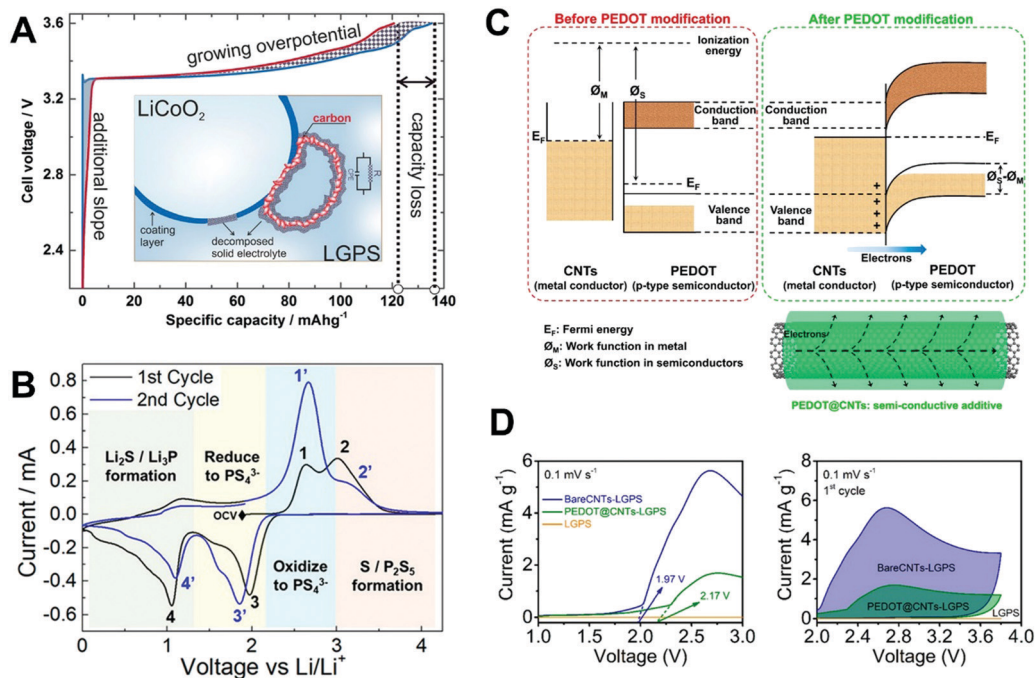
Fig. 14 Detrimental effect of carbon additives in cathode composites for SE-based ASSLBs. (A) Carbon additives facilitate SEs decomposition at the cathode/SE interface, resulting in large over-potential and fast capacity fading. Reproduced with permission from ref. 267. Copyright (2017) American Chemical Society. (B) Cyclic voltammograms for the first two cycles; the voltage was swept between 0 and 4.2 V (vs. Li$^+$/Li) at 0.1 mV s^{-1} starting from the OCV. Reproduced with permission from ref. 269. Copyright (2019) American Chemical Society. (C) Schematic illustration of the role of PEDOT modification.[270] (D) CV profiles at 0.1 mV s^{-1} during the first cycle of LGPS, bare CNT/LGPS, and PEDOT-modified CNT/LGPS. Reproduced with permission from ref. 270. Copyright (2020) American Chemical Society.

practical SE-based ASSLBs. Last but not least, carbon additives are necessary for cathode composites with high areal capacity ($\sim$4 mA h cm^{-2}), particularly for insulative cathodes, i.e. lithium-rich cathodes.[275] How to balance the electronic conductivity of cathode composites and SE decomposition by carbon additives should be carefully engineered in the future.

3.2 Anode interface of SE-based all-solid-state lithium batteries

To fulfill the high energy density of ASSLBs, a thin lithium metal anode is desirable because of its high theoretical capacity (3862 mA h g^{-1}) and the lowest operating potential (-3.040 V vs. standard hydrogen electrodes (SHE)).[3,276–279] However, integration of Li metal anode in ASSLBs face many challenges, including (i) lithium dendrite growth, (ii) severe interfacial reactions, and (iii) infinite volume change of the lithium metal anode.[195,280–284] These challenges must be overcome before realizing ASSLBs with a thin lithium metal anode.[174,285]

Fig. 15A schematically shows the formation of voids and dendrites at the Li/Li$_6$PS$_5$Cl interface during the Li$^+$ platting/ stripping process. When the critical current density for stripping removes Li from the Li/Li$_6$PS$_5$Cl faster than it can be replenished, voids form in the Li metal anode and accumulate on cycling, thus increasing local current density at the interface and eventually leading to lithium dendrite formation and cell failure.[286] J. Janek et al. used in situ XPS to probe the interfacial instability of LGPS at the lithium metal anode. In combination

with time-resolved electrochemical measurements, in situ XPS offers detailed information on the chemical reactions at the Li/LGPS interface. The decomposition of Li$_{10}$GeP$_2$S$_{12}$ leads to the formation of a mixed ion-electron conductive (MIEC) interphase composed of Li$_3$P, Li$_2$S, and Li–Ge alloy.[287,288] Comparatively, argyrodite Li$_6$PS$_5$X (X = Cl, Br, I) decomposes into a Li$_3$P, Li$_2$S, and LiX, which serves as an SEI interface (Fig. 15B).[289]

Another challenge to develop SE-based ASSLBs is the lithium dendrite formation.[290] M. Tatsumisago et al. used in situ SEM to investigate the lithium deposition and dissolution mechanism in bulk-type solid-state lithium batteries with Li$_2$S–P$_2$S$_5$ glass-ceramics.[291] At a high current density, non-uniform lithium deposition triggered large cracks, leading to irreversible lithium deposition and dissolution. But the unfavorable crack formation could be avoided using a small current density.[291]

Over the past years, a lot of investigations based on either in situ characterizations or theoretical calculations have shown that SEs are not stable against Li metal.[74,195,297–302] To rationally design anode interfaces, three types of the Li–SE interface are proposed (Fig. 15C):[292,298] (I) Type I: the stable interface, in which the solid electrolytes are thermodynamically stable against Li metal. Naturally, the interfaces with Li binary compounds e.g. Li/LiF, Li/Li$_3$N, Li/Li$_2$S, and Li/Li$_2$O, belong to this type; (II) Type II: the mixed ionic-electronic conducting interphase (MIEC), in which the sulfide electrolytes are thermodynamically unstable against Li metal, and both the electron and lithium-ion can penetrate through, leading to the continuous

This journal is © The Royal Society of Chemistry 2021

Energy Environ. Sci., 2021, **14**, 2577–2619 | **2595**
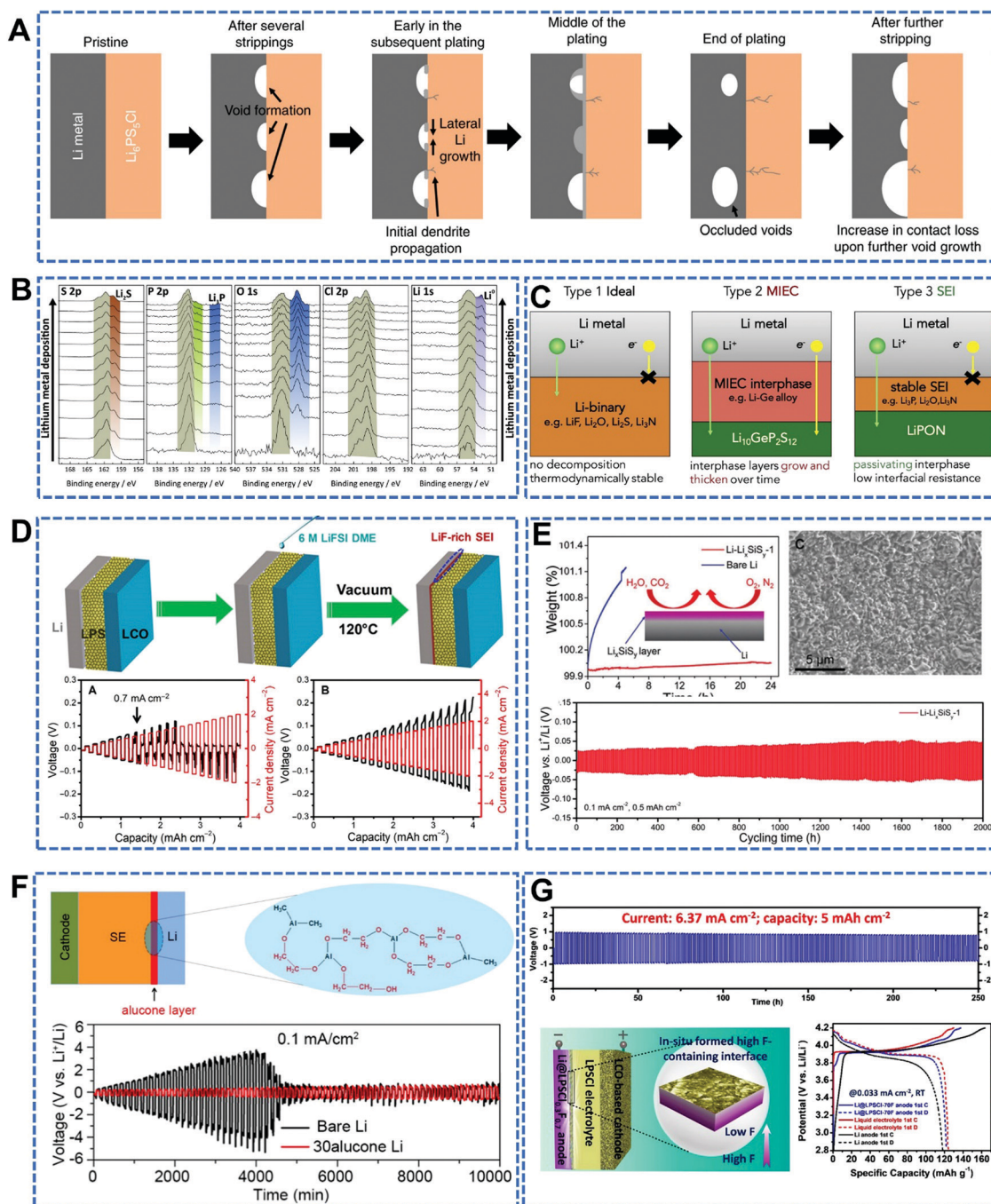
Fig. 15 (A) Schematic of Li metal/Li$_6$PS$_5$Cl interface cycled at an overall current density above the critical current density for stripping. Reproduced with permission from ref. 286. Copyright (2019) Nature Publishing Group. (B) S 2p, P 2p, O 1s, and Cl 2p XPS spectra of a Li$_6$PS$_5$Cl sample as a function of the increasing amount of lithium metal being deposited (from bottom to top). The formation of new species is colored and labeled, showing the decomposition of the original SE phase into Li$_2$S, Li$_3$P, and Li$_2$O. Reproduced with permission from ref. 289. Copyright (2018) Elsevier. (C) Illustration of different types of Li/SE interfaces. Type 1: intrinsically stable interface. Type 2: mixed ion-electron conductive (MIEC) interface, Type 3: a stable solid electrolyte interphase (SEI). Reproduced with permission from ref. 292. Copyright (2018) Cell Press. (D) Schematic illustration of the pretreated processes for the formation of a LiF-rich SEI layer between the Li metal and Li$_3$PS$_4$. Reproduced with permission from ref. 293. Copyright (2018) AAAS. (E) An air-stable Li$_x$SiS$_y$ interfacial coating on Li metal for highly stable SE-based ASSLBs. Reproduced with permission from ref. 294. Copyright (2019) Wiley-VCH. (F) An inorganic−organic hybrid interphase enabled by molecular layer deposition suppresses the interfacial reactions and lithium dendrite formation between Li$_{10}$SnP$_2$S$_{12}$ and Li metal. Reproduced with permission from ref. 295. Copyright (2018) Elsevier. (G) An ultra-stable interface with high capacity and current density achieved by fluorinating SEs. Reproduced with permission from ref. 296. Copyright (2020) American Chemical Society.

decomposition of sulfide electrolytes and consequently causes short-circuiting in all-solid-state batteries. (III) Type III: solid

electrolyte interphase (SEI), which possesses sufficient ionic conductivity and negligible electronic conductivity. The SEI

does not grow and can suppress the interfacial reactions and lithium dendrite formation.[287,299] Ideally, the stable and non-growing SEI is favorable as long as the resulting resistance and IR drop across the SEI layer is negligible.

To suppress the interfacial reactions and lithium dendrite formation at the SE/Li anode interface. Various strategies have been summarized as follows.

(1) *In situ* formed robust SEI: X. Fan *et al.* created a LiF-rich SEI between Li and Li_3PS_4 by infiltrating 6 M LiFSI DME solution (Fig. 15D). This *in situ* formed LiF-rich SEI enhances the critical current density of Li_3PS_4 to a record-high value of >2 mA cm^{-2}. Moreover, the Li plating/stripping coulombic efficiency was increased from 88% of pristine Li_3PS_4 to more than 98% for LiF-coated Li_3PS_4.[293] Y. Gao *et al.* designed an SEI consisting of inorganic/organic Li salts that was formed *in situ* on the Li metal surface by electrochemically decomposing high-concentration liquid electrolytes (*i.e.* 1 M LiTFSI in DOL/DME). Stable Li electrodeposition over 3000 hours was demonstrated.[303]

(2) Surface modification of Li metal: the second approach is a surface modification on the Li metal surface.[304–306] This method has been reviewed in liquid cells.[4,307–309] As an example, we have reported that the Li_3PS_4/Li interface in ASSLBs can be stabilized by an air-stable Li_xSiS_y protection layer that is formed *in situ* on the surface of Li metal through a solution-based reaction between Li_2S_8, $SiCl_4$, and Li metal in THF solution. Highly stable Li cycling for over 2000 h in symmetrical cells and a lifetime of over 100 cycles can be achieved in all-solid-state batteries with a structure of $LiCoO_2/Li_3PS_4/Li$ (Fig. 15E).[294] Also, highly Li$^+$-conductive Li_3PS_4-modified Li was also formed by an *in situ* and self-limiting reaction between polysulfides (*e.g.* P_4S_{16} and Li_2S_6) and Li in solvents (*e.g.* N-methyl-2-pyrrolidone or dimethoxyethane).[304,310] Moreover, an inorganic and organic hybrid interface (Al_2O_3/alucone) as an artificial SEI was engineered at the $Li_{10}SnP_2S_{12}$/Li metal interface by molecular layer deposition (Fig. 15F).[295] The stable Li$^+$ plating/stripping behavior confirms that artificial SEI can suppress the interfacial reactions and prevent spontaneous lithium dendrite formation. Also, LiF or LiI interphase layers, which are stable against Li metal, were proven very effective in suppressing the interfacial reactions and lithium dendrite formation.[195] More recently, C. Wang *et al.* designed Li_3N–LiF composites for high-capacity Li metal anode against Li_3PS_4. Due to the high ionic conductivity, low electronic conductivity, and high surface energy of the Li_3N–LiF composite, Li/Li_3N–LiF/LPS/Li_3N–LiF/Li symmetric cells demonstrated a high critical current >6 mA cm^{-2} even at a high capacity of 6 mA h cm^{-2}.[311] Meanwhile, Li/Li_3N–LiF/LPS/Li_3N–LiF/Li cells demonstrated long-cycle stability at a high current density of 1.0 mA cm^{-2} and capacity of 1 mA h cm^{-2} for 220 hours.[311]

(3) SE modification: apart from the external coating and interfacial modification, it is very attractive to address Li/SE interfacial issues by tuning the SE composition.[165,190,312,313] For example, C. Wang *et al.* demonstrated that the critical current density is improved significantly after incorporating LiI into Li_2S–P_2S_5 glass, reaching 3.90 mA cm^{-2} at 100 °C after adding 30 mol% LiI. Besides, stable cycling of the Li–Li cells for 200 h

is also achieved at 1.50 mA cm^{-2} at 100 °C.[165] Our group recently demonstrated that an ultra-stable interface with high current density and high areal capacity can be achieved by fluorinating SEs (Fig. 15G).[296]

(4) External pressure to mitigate volume change: suitable external pressure is required to accommodate the infinite volume change of Li metal.[266] Notably, by the *operando* neutron diffraction profile (NDP) study, C. Wang *et al.* revealed that the lithium dendrite formation in solid-state electrolytes is due to their high electronic conductivity. Therefore, minimizing the electronic conductivity of solid-state electrolytes instead of increasing their ionic conductivity is critical for suppressing the lithium dendrite formation in ASSLBs.[314]

(5) Reducing electronic conductivity: although the interfacial reactions and lithium dendrite formation at the SE/Li interface can be suppressed by either external interface modification or tuning the internal composition of SEs. The areal capacity for Li plating/stripping is around 0.1–0.5 mA h cm^{-2}, which is far from the requirements of real application of Li metal.[169,315] Considering that the conventional organic separator has a very low electronic conductivity ($10^{-15} – 10^{-16}$ S cm^{-1}), but the electronic conductivity of mainstream SEs is about 10^{-9} S cm^{-1}. Therefore, reducing the electronic conductivity of solid electrolytes can enable the large capacity of lithium metal cycling. More importantly, reducing the electronic conductivity of SEs can significantly reduce the self-discharge phenomena of ASSLBs, which has not been well highlighted yet.

Furthermore, thick Li (460 μm) was widely used in the ASSLB study, which definitely cannot meet the practical application. Thin Li (<40 μm) should be investigated in the future.[316] In theory, the coulombic efficiency of Li metal must be higher than 99.95% to ensure a long cycling life near 450 cycles, provided that 20% Li are consumed during the electrochemical cycling.[317] If the coulombic efficiency is 99.98%, the cycling life over 1000 cycles can be achieved providing 20% Li metal consumption during cycling. For the coulombic efficiency over 99.99%, the cycling life can be 2000 cycles with 20% Li consumption.

In summary, using Li metal anode in SE-based ASSLBs is highly critical for realizing high energy density. However, lithium metal in SE-based ASSLBs faces many challenges such as detrimental interfacial reactions, lithium dendrite growth, and infinite volume change. To overcome these tough challenges, interfacial reaction mechanisms and interfacial structure evolution have been well studied. Based on the in-depth understanding, several effective strategies such as *in situ* formed SEI, interface modification of Li metal, tuning chemical composition and electronic conductivity of SEs, as well as applying external pressure have been demonstrated to successfully address interfacial challenges between Li metal and SEs. Despite the tremendous success, further improvements on the cycling capacity (*i.e.* >4 mA h cm^{-2}), current density, cycling life of Li metal should be pursued. Moreover, the electronic conductivity of SEs should be significantly reduced to at least 10^{-12} S cm^{-1} to avoid the lithium dendrite growth along the grain boundaries of SEs and mitigate the

This journal is © The Royal Society of Chemistry 2021

Energy Environ. Sci., 2021, **14**, 2577–2619 | **2597**

self-discharge phenomenon of SE-based ASSLBs. Furthermore, future work should be performed based on ultrathin Li metal foil (*i.e.* <40 μm) and lean electrolytes,[318] which will give more constructive information for the development of practical SE-based solid-state lithium metal pouch cells.

4. Advanced characterizations on SE-based ASSLB interface

To further promote the advance on SE-based ASSLBs, an in-depth understanding of their interface is crucial.[327] Fortunately, lots of *in/ex situ* characterization techniques have been developed in recent years that can probe the interfacial chemical and structural information of ASSLBs.[328–331] Herein we classified those characterization techniques into spectroscopy and imaging technologies, most of which are *in situ* techniques for characterizing the interface of ASSLBs.

(1) Spectroscopy techniques: XPS technique is an excellent tool to analyze the interface of ASSLBs.[289] For example, S. Wenzel *et al.* systematically studied the chemical reactions at the Li/LGPS interface through *in situ* XPS combined with time-resolved impedance spectroscopy studies (Fig. 16A). It is found that the LGPS will be reduced to an SEI layer that is mainly comprised of Li_3P, Li_2S, and Li–Ge alloys, which will increase interfacial resistances (Fig. 16B). Furthermore, K. Wood *et al.* employed *operando* XPS and real-time *in situ* Auger electron spectroscopy mapping to probe the formation and evolution of the $Li/Li_2S–P_2S_5$ interface during electrochemical cycling, showing that electrochemically driving Li^+ to the surface leads to phase decomposition into Li_2S and Li_3P.[332] Raman is also a powerful tool to characterize the interface of ASSLBs.[333] For instance, M. Tasumisago *et al.* performed *in situ* Raman on the LCO/SE composites before and after initial charging, which demonstrated the unequal charge status of LCO particles.[334] R. Nuzzo *et al.* used *in situ* Raman spectroscopy to evaluate potential-dependent changes in the chemistry of SEs at active electrode interfaces (Fig. 16C).[319] Our group also conducted *in situ* Raman spectroscopy to investigate the mechanism of the Se cathode in the all-solid-state system, which identified the evolution of the Se and $PS_{4-x}Se_x{}^{3-}$ species in the cathode composite during the charge/discharge process (Fig. 16D).[40,320] Moreover, *in situ* and *operando* X-ray absorption spectroscopy (XAS), which is sensitive to the electronic states of materials, has been applied to investigate interfacial reactions in solid-state batteries.[335] Our group performed *in situ* and *operando* XAS to investigate interfacial behavior between Ni-rich layered cathodes and SEs. It is found that a metastable intermediate state of SEs exists at high voltage and parasitic reactions with cathodes exist during the charge/discharge process, which leads to the surface structural reconstruction of Ni-rich cathodes.[214] Moreover, Y. Yamagishi *et al.* visualized the lithium distribution and degradation in the cathode composite (NCA/Li_3PS_4) during cell operation using *operando* time-of-flight secondary ion mass spectrometry (Tof-SIMS) (Fig. 16E).[321] *In situ* neutron depth profiling (NDP),

as a non-destructive and Li-sensitive technique, also offers the possibility to observe lithium transport inside batteries.[336,337] For example L. Hu's group developed *in situ* NDP to *in situ* monitor the Li distribution and transport between garnet-typed solid electrolytes and metallic Li during cycling (Fig. 16F).[338] This *in situ* NDP technique is also able to diagnose the short circuits in solid-state batteries. As proven by C. Wang's group, the high electronic conductivity of SEs is responsible for the short-circuits of SE-based ASSLBs.[322] Therefore, reducing the electronic conductivity of SEs is highly crucial for stabilizing Li metal in ASSLBs. More recently, H. Zhu's group employed *operando* energy-dispersive X-ray diffraction (EDXRD) to observe the evolution of $Li_{6.6}Ge_{0.6}Sb_{0.4}S_5I$ at different voltages within FeS_2-based all-solid-state lithium–sulfur batteries.[339] These *in situ* spectroscopies provided detailed information at the interface of SE-based ASSLBs, which can serve as a guideline to overcome the interfacial challenges of ASSLBs.

(2) Imaging techniques: other than various *in situ* and *operando* spectroscopies, directly observing interface changes is also very important for understanding the interfacial behavior of ASSLBs. Apart from a lot of classic techniques, such as scanning electron microscopy (SEM),[212] or high-resolution transmission electron microscopy (HRTEM),[208] we summarized emerging *in situ* imaging techniques. For example, H. Masuda *et al.* combined Ar ion milling under non-atmospheric conditions with *in situ* cross-sectional Kelvin probe force microscopy (KPFM) for direct imaging of the internal electrical potential distribution of ASSLBs (Fig. 16G). The potential distribution around the interface between active materials and a solid electrolyte indicates the inhomogeneity of electrochemical reactions in the electrode.[323,340] Besides, J. Wan *et al.* investigated the morphological evolution of Li–In alloy anodes during Li deposition and stripping process by *in situ* atomic force microscopy, which interestingly elucidated a blocking formation and stack-accumulation behaviors during Li deposition.[341] Chien *et al.* employed 3D ^7Li magnetic resonance imaging (MRI) to examine Li distribution homogeneity in solid electrolyte $Li_{10}GeP_2S_{12}$ within $Li/Li_{10}GeP_2S_{12}/Li$ symmetric cells (Fig. 16H). The 3D 7Li MRI images demonstrated that a large amount of Li was consumed at the Li/LGPS interface, which can be mitigated *via* PEO coating.[324] Furthermore, *in situ* STEM-EELS with a high spatial resolution was used to observe the interfacial phenomena of $LiCoO_2/LiPON$ with a nanoscale resolution (Fig. 16I).[325,342] An unexpected structurally disordered interfacial layer was discovered without cycling. A disordered interfacial layer between cathode and electrolyte will form and accumulate lithium and evolves to rocksalt CoO after cycling.[325] Considering that SEs are sensitive to the high-energy electron beam, Cryo-TEM was explored recently for characterizing SEs and cathode/SE interface.[243] Recently, *in situ* synchrotron-based X-ray tomography is revived to investigate the ASSLBs. S. Pylypenko *et al.* developed *in situ* synchrotron-based X-ray tomography with a spatial resolution of 1 μm to investigate the formation and propagation of Li within $Li/Li_3PS_4/Li$ symmetrical cells (Fig. 16J).[326] The expansion of voids is observed throughout the symmetric cells. The crack propagation is probably caused

2598 | *Energy Environ. Sci.*, 2021, **14**, 2577–2619

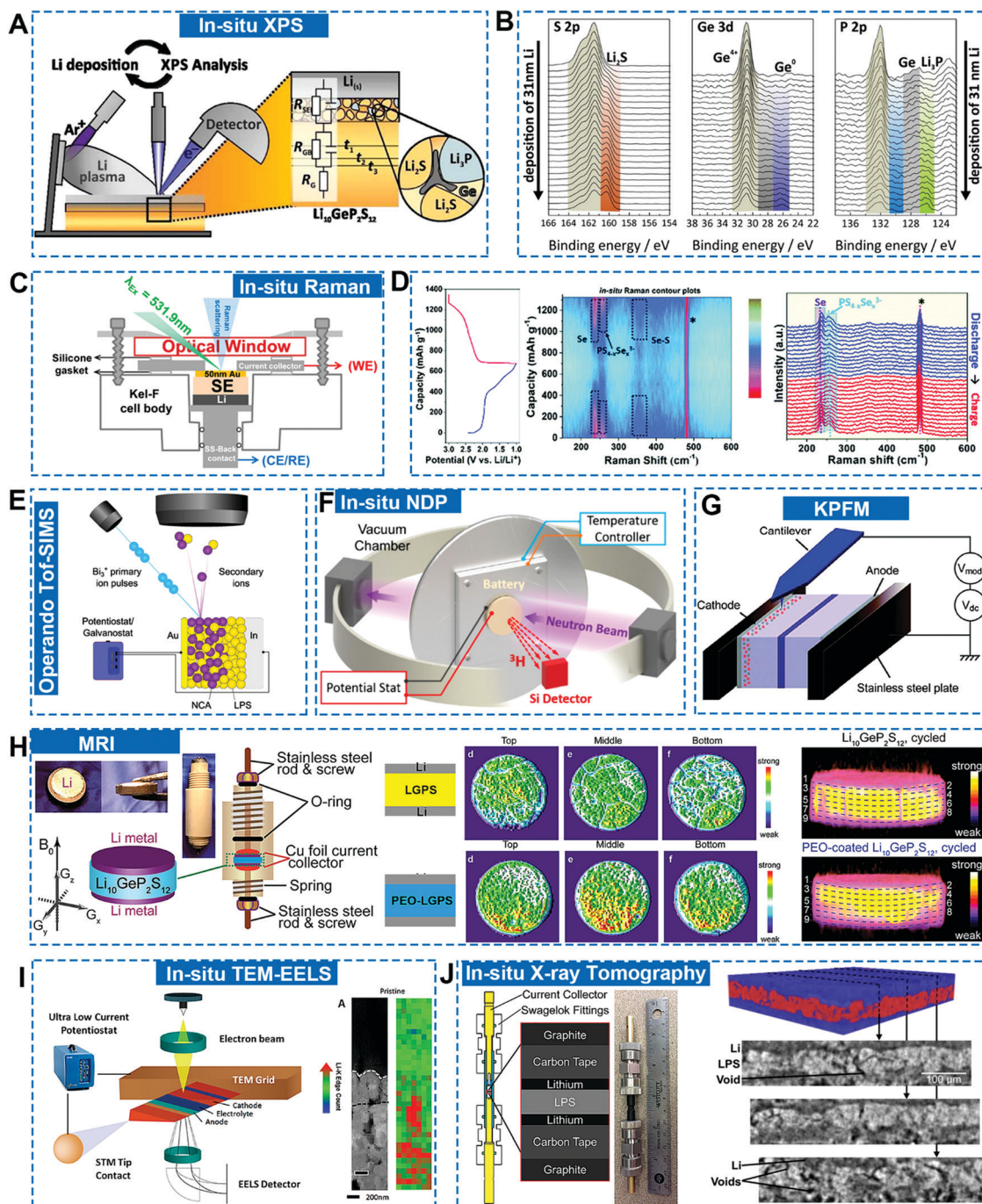This journal is © The Royal Society of Chemistry 2021

Fig. 16 Advanced Characterizations on the Interface of ASSLBs. (A) A schematic diagram of *in situ* XPS setup for analyzing the Li/SE interface. Reproduced with permission from ref. 287. Copyright (2016) American Chemical Society. (B) S 2p, Ge 3d, and P 2p detail spectra of LGPS/Li during 31 nm Li metal deposition on LGPS surface. Reproduced with permission from ref. 287. Copyright (2016). American Chemical Society. (C) Schematics of an *in situ* Raman cell for measuring Li/SE interface. Reproduced with permission from ref. 319. Copyright (2017) American Chemical Society. (D) *In situ* Raman analysis of all-solid-state Li–Se batteries during the first charge/discharge process. Reproduced with permission from ref. 320. Copyright (2018) The Royal Society of Chemistry. (E) Schematic illustration of *operando* SIMS measurement performed on an all-solid-state battery cell. Reproduced with permission from ref. 321. Copyright (2021) American Chemical Society. (F) Schematic of the neutron depth profiling (NDP) system. Reproduced with permission from ref. 322. Copyright (2017) American Chemical Society. (G) Schematic illustration of cross-sectional KPFM setup inside the N_2 flow glove box. Reproduced with permission from ref. 323. Copyright (2017) The Royal Society of Chemistry. (H) Pictures and schematic of a symmetric Li/Li$_{10}$GeP$_2$S$_{12}$/Li battery placed in a home-made cylindrical cell for MRI. 3D ^{7}Li MRI image of the Li/LGPS/Li and Li-PEO-coated LGPS/Li. Reproduced with permission from ref. 324. Copyright (2018) American Chemical Society. (I) Schematic of *in situ* TEM biasing of nanobattery. Reproduced with permission from ref. 325. Copyright (2016) American Chemical Society. (J) Schematic and image of the *operando* cell, optimized for X-ray microscopy by surrounding the Li/LPS/Li symmetric cell with low X-ray absorbing materials. 3D reconstruction of X-ray tomography data for an uncycled Li/LPS/Li stack. Reproduced with permission from ref. 326. Copyright (2018) The Electrochemical Society.

This journal is © The Royal Society of Chemistry 2021

Energy Environ. Sci., 2021, **14**, 2577–2619 | **2599**

by the interaction between the Li metal and pre-existing voids in the LPS electrolytes.[326] Kota Suzuki *et al.* analyzed lithium distribution in SE-based ASSLBs by particle-induced X-ray and gamma-ray emission measurements.[343] These powerful characterization techniques provided valuable information and guidance on the interface design of SE-based ASSLBs.

Apart from advanced characterizations, the theoretical calculation is very informative for seeking for superionic solid conductors,[175,178,344–346] guiding interface design,[195,215] understanding interfacial reaction mechanisms and Li-ion transport mechanisms in SEs,[155,232,347,348] as well as electrode engineering.[349] For example, using DFT calculation,[350] a new superionic conductor (Li_2CuP_4) with a kesterite structure was predicted to exhibit a high ionic conductivity of 84.9 mS cm^{-1} at 300 K. In terms of interface coating, computational screening suggests that LiH_2PO_4, $LiTi_2(PO_4)_3$, and $LiPO_3$ are particularly appealing cathode coating materials. These promising theoretical results should be experimentally verified in the future.

In summary, advanced *in situ* and *operando* characterization techniques and theoretical calculations are informative in understanding the Li$^+$ transport at the interface, interfacial reaction mechanisms, as well as the structural evolution of SEs and their full cells, thus providing guidelines for designing superionic SEs and stable interfaces for ASSLBs. In the future, continuous efforts should be devoted to developing advanced characterization techniques. Single *in situ* characterization is often not comprehensive enough for fully understanding perplexing lithium-ion transport in SEs and how they interact with the interface with electrodes. Therefore, it is highly recommended to combine multiple *in situ* characterizations with rational theoretical calculations to thoroughly understand the complex interfacial transport kinetics and corresponding interfacial reaction mechanism in SE-based ASSLBs, which is essential for the development of ASSLBs with high energy density and safety.

5. Demonstrations of SE-based ASSLBs

5.1 SE-based all-solid-state lithium-ion batteries (ASSLIBs)

Due to the high ionic conductivity of SEs, high-performance ASSLBs have been widely reported in references, including organic cathodes,[351–353] metal oxides cathodes,[354] sulfur cathodes,[355] and metal sulfide cathodes.[135,339] Typically, ASSLIBs based on highly Li$^+$-conductive $Li_{9.54}Si_{1.74}P_{1.44}S_{11.7}Cl_{0.3}$ demonstrate not only excellent cycling performance with 75% of the first discharge capacity remaining after over 500 cycles but also excellent rate capabilities with discharge current densities of 150C at 25 °C and 1500 °C at 100 °C.[15] The high power density is even comparable to that of supercapacitors.[15] Moreover, high-capacity and high-voltage electrodes have also been investigated in SE-based ASSLIBs such as $LiNi_{0.8}Co_{0.15}Al_{0.05}O_2$,[356] $LiNi_{1/3}Co_{1/3}Mn_{1/3}O_2$,[357] $LiNi_{0.5}Co_{0.2}Mn_{0.3}O_2$,[234] $LiNi_{0.6}Co_{0.2}Mn_{0.2}O_2$,[358,359] $LiNi_{0.8}Co_{0.1}Mn_{0.1}O_2$,[212,360] $LiNi_{0.90}Co_{0.05}Mn_{0.05}O_2$,[23] $LiNi_{0.5}Mn_{1.5}O_4$.[268] As demonstrated by M. Hirayama *et al.*, the high-voltage cathode, $LiNi_{0.5}Mn_{1.5}O_4$

delivers a specific capacity of 80 mA h g^{-1} with an average voltage of 4.3 V, using LGPS and Li metal anodes.[268] To be concise, the progress on advanced SE-based ASSLIBs can be simply divided into three categories: including active material designs; cathode/SE interface designs; and composite electrode designs, as shown in Fig. 17.

(1) Active material design: so far the mainstream active materials (*i.e.* NMC, NCA) are polycrystalline secondary particles. Unlike liquid cells, in which the liquid electrolyte can penetrate the pores of polycrystalline active materials, the solid-state battery shows great challenges at the interface contact between cathodes and solid-state electrolytes. In general, the solid-state electrolyte can only contact the cathode materials on the surface through solid–solid contact. In this case, Li$^+$ needs to pass through many grain boundaries of polycrystalline active materials before reaching the solid electrolytes. Comparatively, single-crystal cathodes do not contain grain boundaries inside one particle, thus providing continuous Li$^+$ conduction pathways. Therefore, the single-crystal cathode is believed to show faster Li$^+$ kinetics in ASSLIBs than the polycrystalline cathode.[364] We systematically compared SC-NMC532 and PC-NMC532. The comparison confirms that the SC-NMC532 demonstrates much faster Li$^+$ diffusion kinetics than PC-NMC532, thus showing better rate capability (Fig. 17A).[361] Recently, X. Liu *et al.* revealed single-crystalline NMC811 shows better mechanical integrity than the polycrystalline counterpart in ASSLBs, thus demonstrate more stable cycling performance.[365] Furthermore, a full-concentration gradient $Li[Ni_{0.75}Co_{0.10}Mn_{0.15}]O_2$ (FCG75) with radially oriented grains was designed to accommodate for volume change in ASSLIBs, which was able to maintain mechanical integrity during cycling. Compared with conventional $Li[Ni_{0.80}Co_{0.16}Al_{0.04}]O_2$ (NCA80), FCG75 demonstrated a high capacity retention of 79.1% after 200 cycles at 0.5C (Fig. 17B). Apart from the morphology design, the particle size of active materials also has a significant impact on the electrochemical performance of ASSLIBs.[358] As demonstrated by J. Janek *et al.*, cathode composites containing NMC622 with a small particle size (<10 μm) delivered a much higher discharge capacity than NMC622 with large particle size.[358] Moreover, Ceder's group also reported that optimization of particle size active materials as well as SEs is required for high-loading cathode composites in ASSLIBs.[349]

(2) Cathode/SE interface design: as discussed in Section 3.1, large interfacial resistance originating from the detrimental interfacial reactions and poor solid–solid contact significantly constrains the electrochemical performance of ASSLIBs.[366] To suppress large interfacial reactions, an interfacial coating layer preventing interfacial reactions between active materials and SEs is required.[367] For instance, D. Cao *et al.* reported using a thin amorphous $Li_{0.35}La_{0.5}Sr_{0.05}TiO_3$ (LLSTO) layer with high ionic conductivity of 8.4×10^{-5} S cm^{-1} coated on $LiNi_{1/3}Mn_{1/3}Co_{1/3}O_2$ (NMC111). The LLSTO-coated NMC111 delivered a high discharge initial capacity of 122 mA h g^{-1} at C/10, and 90 mA h g^{-1} at C/3 and kept stable for 450 cycles (Fig. 17C). Our group has demonstrated a dual-shell coating on active materials, in which the inner shell $LiNbO_3$ (LNO) is to suppress interfacial

2600 | *Energy Environ. Sci.*, 2021, **14**, 2577–2619

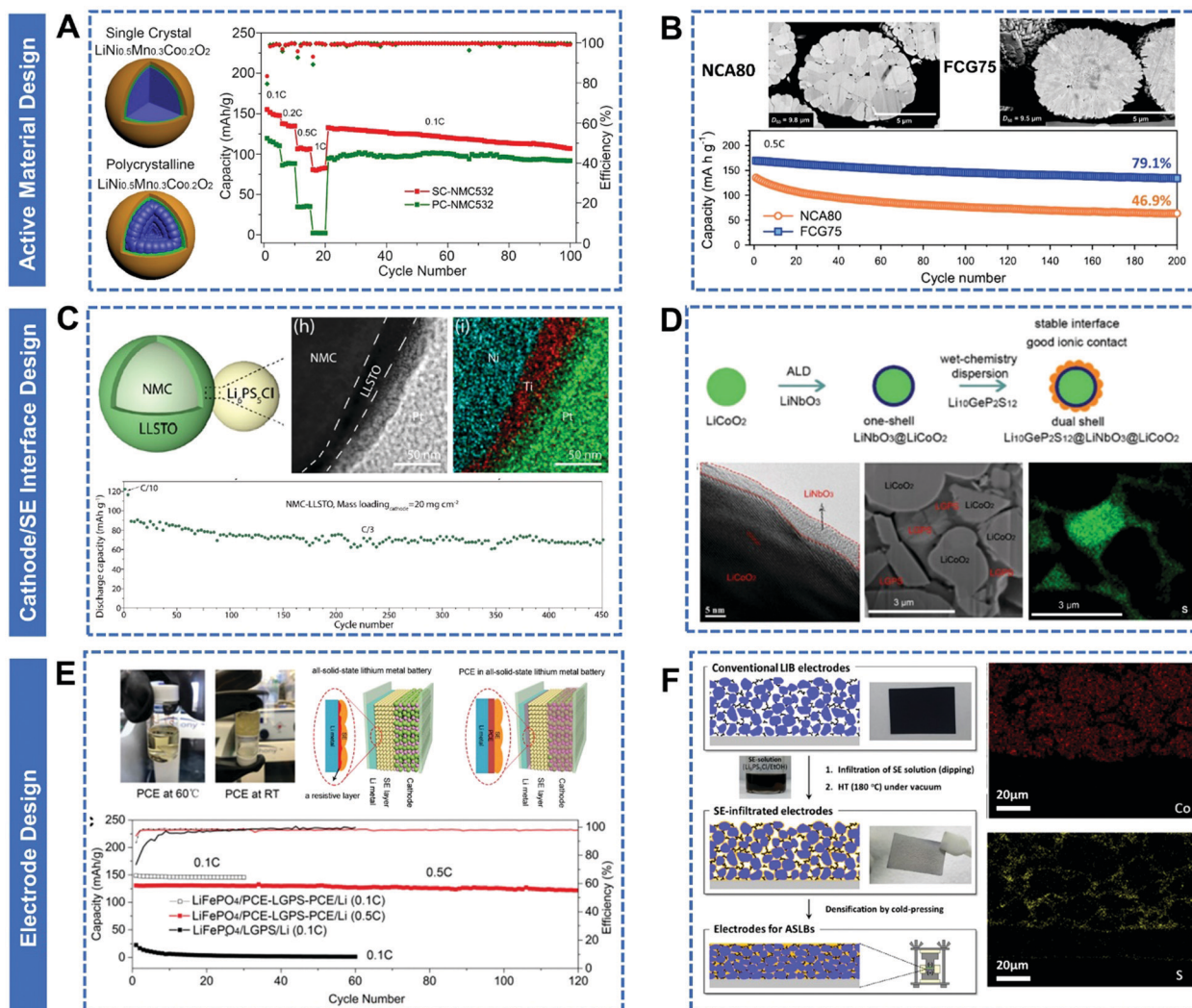This journal is © The Royal Society of Chemistry 2021

Fig. 17 (A) Rate-performance comparison of single-crystal NMC532 with polycrystalline NMC532. Reproduced with permission from ref. 361. Copyright (2020) Elsevier. (B) Cross-sectional SEM images of conventional NCA80 and radially-oriented FCG75 particles with their cycling performance in ASSLBs. Reproduced with permission from ref. 362. Copyright (2020) Wiley-VCH. (C) TEM image elemental mapping of $Li_{0.35}La_{0.5}Sr_{0.05}TiO_3$-coated NMC111 and its long cycling performance at C/3. Reproduced with permission from ref. 235. Copyright (2019) American Chemical Society. (D) Dual-shell design for cathode composites of SE-based ASSLBs. Reproduced with permission from ref. 213. Copyright (2019) Wiley-VCH. (E) Improving solid–solid ionic contact in slurry-coated electrode sheet by plastic crystal electrolytes. Reproduced with permission from ref. 363. Copyright (2019) Wiley-VCH. (F) Schematic diagram illustrating the infiltration of conventional IB composite electrodes with solution-processable SEs. EDXS elemental maps of the LPSCl-infiltrated LCO electrode. Reproduced with permission from ref. 246. Copyright (2017) American Chemical Society.

reactions while the outer shell $Li_{10}GeP_2S_{12}$ (LGPS) is to improve the solid–solid contact between active materials and SEs. The resultant LGPS@LNO@LCO with a dual shell structure demonstrated not only long-term cycling stability but also high rate performance (Fig. 17D).[213] Besides, the volume change of electrode materials during the charge–discharge process results in "loss contact" between electrodes and SEs.[212,261] Using zero-strain materials as the electrode, such as $Li_4Ti_5O_{12}$, results in solid-state batteries that exhibit remarkable cycling performance within 700 cycles.[368]

(3) Electrode design: for solid-state pouch cell manufacturing, sheet-type electrodes are necessary. Our group has demonstrated that a solid-state plastic crystal electrolyte (PCE), which is solid–liquid transformable, can enable sheet-type electrode

fabrication.[363] As shown in Fig. 17E, the conventional LiFePO₄ electrode can be filled with PCEs at elevated temperature. The sheet-typed LiFePO₄ electrode in our tests exhibited stable cycling performance at 0.5C for 120 cycles in LGPS-based ASSLBs due to excellent compatibility between PCEs and LGPS. D. Kim et al. reported a scalable fabrication protocol for sheet-typed electrodes of ASSLBs. As presented in Fig. 15F, Li_6PS_5Cl ethanol solution is infiltrated into conventional porous electrodes, which was further densified by cold pressing. This infiltration method enabled intimate solid–solid contact and favorable ionic percolation.[246] This method is compatible with current LIB fabrication technology. However, the ionic conductivity of solution-processable SEs should be further improved to ensure the high-rate performance of ASSLIBs.[254,369]

This journal is © The Royal Society of Chemistry 2021

Energy Environ. Sci., 2021, **14**, 2577–2619 | **2601**

As a summary, to further improve ASSLIBs, there are several parameters to be considered. (1) The interfacial reactions between the electrode and SEs should be suppressed to enable long-term cycling stability. (2) The electrode–electrolyte contact area should be maximized either by physical deposition, solution method coating, or organic polymer infiltration. (3) The volume change of electrode materials can result in the "loss contact" between the electrodes and SEs. Therefore, the strategies to accommodate the volume change of ASSLIBs need to be developed in near future. (4) Last but not least, advanced techniques, such as 3D printing, should be used to fabricate the thin SE layer to increase the cell-level energy density of ASSLIBs.

5.2 SE-based all-solid-state lithium–sulfur batteries (ASSLSBs)

Lithium–sulfur (Li–S) batteries have been considered as one of the most promising next-generation battery technologies with a potential of possessing energy densities at least twice those of state-of-the-art Li-ion batteries.[276,370–373] However, intermediate polysulfides, especially the long-chain polysulfides, will easily dissolve in the liquid electrolyte causing a "shuttle effect".[374] This notorious "shuttle effect" leads to fast capacity degradation, low coulombic efficiency, and severe self-discharge.[375,376] To solve this major problem, the replacement of liquid organic electrolytes with solid-state SEs may be the ultimate approach to eliminate the shuttle effect.[377] In recent years, lots of encouraging results on SE-based all-solid-state

lithium–sulfur batteries (ASSLSBs) have been demonstrated.[58,378–381] For example, a glassy $75Li_2S–25P_2S_5$ (stoichiometric Li_3PS_4) electrolyte has been applied to develop high-performance ASSLSBs. An initial capacity as high as 1600 mA h g^{-1} with high coulombic efficiency of 99% was demonstrated.[382] No obvious capacity degradation within 100 cycles was observed. However, ASSLSBs exhibit a very low utilization of active materials.[383] M. Tatsumisago et al. demonstrated that using lithium halides (LiCl, LiBr, and LiI) can dramatically improve the utilization of Li_2S in ASSLSBs. Specifically, $80Li_2S·20LiI$ can achieve 1100 mA h g^{-1} at 0.5C (corresponding to 95% of theoretical capacity) and 980 mA h g^{-1} at 2C (Fig. 18A). More impressively, the ASSLSBs could achieve results of 980 mA h g^{-1} for 2000 cycles without capacity decay.

It is believed that the three-phase interface between active materials, carbon additives, and SEs are critical to achieving high reversible capacity in ASSLSBs.[381,384] Therefore, many nanocomposites have been designed to achieve both high capacity and long cycling stability.[385,386] For example, C. Wang et al. synthesized a nanocomposite consisting of nanosized Li_2S, carbon matrix, and Li_6PS_5Cl. The homogeneous nanocomposite electrode achieved a large reversible capacity of 830 mA h g^{-1} (71% utilization of Li_2S) at 50 mA h g^{-1} for 60 cycles.[387] C. Liang's group fabricated core–shell structured Li_2S nanoparticles with Li_2S as the core and Li_3PS_4 as the shell, functioning as the lithium superionic sulfide cathode for ASSLSBs,[388] which demonstrated an initial discharge capacity
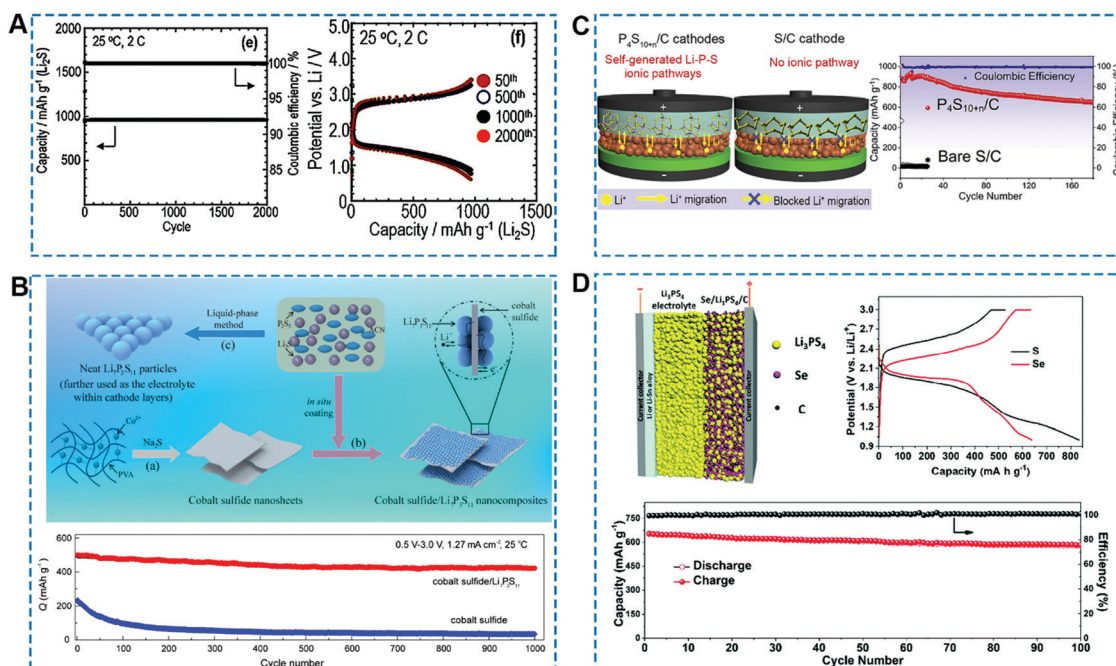
Fig. 18 (A) Long-term cycle performance of the cell with $80Li_2S·20LiI$ electrode materials for 2000 cycles at 2C and its charge–discharge curves. Reproduced with permission from ref. 389. Copyright (2017) Wiley-VCH. (B) Long-term cycling ASSLSBs based on cobalt sulfide/$Li_7P_3S_{11}$ nanocomposites at 1.27 mA cm^{-2}. Reproduced with permission from ref. 135. Copyright (2016) American Chemical Society. (C) Schematic ion transport in ASSLSBs with P_4S_{16}/C and S/C cathodes. Reproduced with permission from ref. 390. Copyright (2020) Elsevier. (D) Schematic diagram of an all-solid-state Li–Se battery with its typical discharge/charge profiles and cycling performance at 50 mA g^{-1}. Reproduced with permission from ref. 320. Copyright (2018) The Royal Society of Chemistry.

2602 | Energy Environ. Sci., 2021, **14**, 2577–2619

This journal is © The Royal Society of Chemistry 2021

of 1216 mA h g^{-1} (based on the sulfur content) at 60C. This result accounts for a 73% utilization of Li_2S and was still able to be maintained at a 70% capacity after 100 cycles.

Besides elemental sulfur (S_8) and Li_2S, a lot of metal sulfides, such as TiS_2,[303] FeS_2,[391] Co_8S_9 and Li_3CuS_2,[392] have been used in ASSLS batteries because metals sulfides have a high electronic conductivity compared to S_8 and Li_2S. Recently, $Co_8S_9/Li_7S_3S_{11}$ nanocomposites were designed for ASSLSBs, which displayed 1000 cycles at 1.24 mA cm^{-2} at room temperature (Fig. 18B). Our group has developed a series of unique P_4S_{10+n} cathodes for high-performance all-solid-state Li–S batteries, in which no extra SEs are added into cathode composites (Fig. 18C).[390] Synchrotron-based X-ray absorption near edge structure analysis coupled with other analyses confirmed that ionic conductive Li_3PS_4 together with $Li_4P_2S_6$ components can be electrochemically self-generated during the lithiation process and partially maintained to provide fast Li$^+$ transport pathways within the cathode layer. The P_4S_{34}/C cathode showed a highly reversible capacity of 883 mA h g^{-1} and stable cycling performance over 180 cycles with a high active material content of 70 wt%. Furthermore, our group also developed all-solid-state Li–Se batteries.[320] Compared to elemental S_8, selenium (Se) possesses a higher electronic conductivity, showing great promise for application in all-solid-state batteries.[393,394] Se–Li_3PS_4–C was synthesized by ball milling, which was used as the cathode composites for all-solid-state Li–Se batteries (Fig. 18D). Because of the higher electronic conductivity (1×10^{-3} S cm^{-1}) of Se than that of S_8 (0.5×10^{-27} S cm^{-1}), Se–Li_3PS_4–C cathodes exhibited a smaller polarization than that of S_8. Furthermore, due to the high electronic and ionic conductivity of Se–Li_3PS_4–C cathode composites, the all-solid-state Li–Se batteries exhibited an initial capacity of 652 mA h g^{-1} (corresponding to 96% theoretical capacity), which remained at 585 mA h g^{-1} after 100 cycles.

In summary, to enable high-performance ASSLSBs, first, improving the electronic conductivity of sulfur cathodes is of great importance to obtain a high reversible capacity in ASSLSBs. Second, a three-phase interface between active materials, carbon additives, and SEs should be carefully designed to ensure the long-term cycling stability of ASSLSBs. Ideally, the electronic conduction path and ionic conduction path should

be separated to avoid the detrimental interfacial reactions between carbon additives and SEs. Third, the significant volume change of sulfur cathodes (78%) in ASSLSBs that still requires significant investigation. Moreover, on the anode side, lithium dendrite formation is also a big challenge in SE-based ASSLSBs, which requires continuous effort in the future. Based on our calculation, sulfur loading in the cathode composites should be improved to 6 mg cm^{-2} to realize the high energy density of 600 W h kg^{-1}. Therefore, the high mass loading of sulfur cathodes for ASSLSBs should be developed with high sulfur utilization. Correspondingly, ultra-thin Li metal foil with a high areal capacity (>4 mA h cm^{-2}) should be realized with stable cycling performance and no dendrite formation.

6. Guidelines for SE-based all-solid-state pouch cells

6.1 Engineering design of sulfide-based solid-state pouch cells

Although tremendous success has been reported based on literature analysis,[395] the state-of-the-art energy density of SE-based all-solid-state pouch cell is far behind the commercial LIBs based on liquid electrolytes.[395] Currently, most of the fundamental studies were performed in mold cells, (Fig. 19A), in which the favorable interfacial ionic contact between active materials and SEs is achieved by mechanical pressing due to the excellent deformability of SEs (Fig. 19B). However, mold cells are only suitable for fundamental research and are not realistic for real application. Instead, pouch-format cells based on the lamination process are the ultimate choice for realizing the high-energy-density of SE-based ASSLBs (Fig. 19C).[396,397] Due to the immature engineering process for developing all-solid-state pouch cells and the huge gap between fundamental study and practical engineering, only a few publications reported SE-based all-solid-state pouch cells.[142,398] Therefore, how to realize high-energy-density all-solid-state pouch cells is not sufficiently well understood.

To guide the engineering design of SE-based all-solid-state pouch cells with the targets of 250 W h kg^{-1}, 300 W h kg^{-1}, and 350 W h kg^{-1}, and 400 W h kg^{-1}, we numerically analyzed the
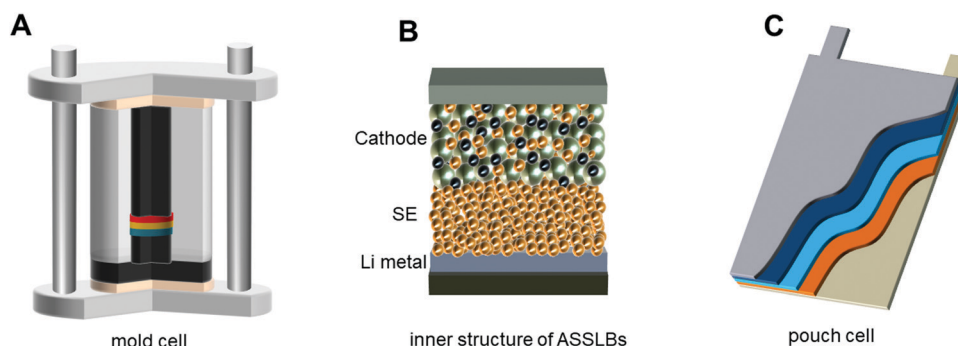

Fig. 19 (A) Schematic diagram of solid-state mold cells for laboratory research. (B) The inner structure of ASSLBs. (C) Schematic diagram of solid-state pouch cells with bipolar stacking.

This journal is © The Royal Society of Chemistry 2021

Energy Environ. Sci., 2021, **14**, 2577–2619 | **2603**

Table 2   Parameters of selected electrode systems for energy density calculation

Electrode materials	Average voltage (V)	N/P ratio	Cathode			Anode		
			Press density (g cm^{-3})	Reversible capacity (mA h g^{-1})	Initial CE (%)	Press density (g cm^{-3})	Reversible capacity (mA h g^{-1})	Initial CE (%)
LCO|graphite	3.9	1.05	4.2	160	90	1.6	350	94
NMC811|Si–C	3.6	1.05	3.6	200	90	1.6	450	90
NMC811|Li	3.7	2	3.6	200	90	0.53	3860	100
Li-Rich|Li	3.8	2	2.7	270	90	0.53	3860	100

energy density of various electrode systems with practical engineering parameters, which we listed in Table 2. This calculation is based on the bi-polar stacking technology with 44 cathode sheets and 45 anode sheets. The dimension of solid-state pouch cells is assumed to be 102 mm × 52 mm. The 15 μm carbon-coated Al foil and 8 μm carbon-coated Cu foils are chosen as the current collectors. A 115 μm aluminum laminated film with a density of 1.576 g cm^{-3} is used as the package. The promising Li$_6$PS$_5$Cl is selected as the typical SE for energy density evaluation. The thickness of cathode composites is fixed as 70 μm in this calculation. The corresponding capacity of the cathode sheet is approximately 4 mA h cm^{-2}. It should be noted that further reducing the thickness of the current collectors and aluminum laminated film also can enhance the practical energy density of SE-based ASSLBs.

The most critical parameters that have the greatest impact on the energy density of all-solid-state pouch cells are the active material contained in cathode composites, SE thickness, discharge capacity and voltage, tap density, and negative-to-positive electrode ratio (N/P ratio). For certain electrode systems, the most critical engineering parameters are active material content and SE thickness. The rest of the parameters are fixed as shown in Table 2. In this numerical analysis, the cathode content varying from 70% to 90% is examined. The active material content over 90% is technically very challenging to achieve considering that intimate solid–solid contact must be guaranteed to ensure full utilization of active materials in ASSLBs. The thickness of SE membranes varies from 500 μm to 10 μm.

(1) LCO/graphite system with an energy density target of 250 W h kg^{-1}. Using LCO as the cathode and graphite as the anode, 250 W h kg^{-1} can be achieved when the thickness of the Li$_6$PS$_5$Cl layer is 30 μm and the cathode content in the composite is 85% (Fig. 20B and 21A). In the references, most cathode content is 70%, in that case, LCO/SE/graphite can only deliver an energy density of 200 W h kg^{-1} when even an ultra-thin SE membrane of 50 μm is incorporated. The upper limit of gravimetric energy density based on LCO/SE/graphite pouch cells cannot exceed 280 W h kg^{-1}. Accordingly, the upper limit of volumetric energy density will not go beyond 660 W h L^{-1} (Fig. 20C). It should be mentioned here that the graphite content in the anode component is assumed to be 80% (graphite : SE = 80% : 20%), although it is very technically challenging. If this battery system was loaded in an electric vehicle, we may wonder how far this electric vehicle can go per charge. Fig. 21A estimated the mileage range of an electric vehicle (EV) based on LCO/SE/graphite pouch cell. According to

the performance of Tesla's electric vehicles model 3 (6.25 km kW^{-1} h^{-1}) and model X (5.23 km kW^{-1} h^{-1}), we assume 6 km kW^{-1} h^{-1} for this estimation, and 400 kg batteries are loaded in an EV. Under this condition, all-solid-state LCO/graphite pouch cells with an energy density of 250 W h kg^{-1} can enable an EV to drive 5600 km. It should be mentioned this mileage range may vary with the gross weight of an EV and real road condition.

(2) NMC811/Si–C-450 system with an energy density target of 300 W h kg^{-1}. As mentioned above, the LCO/graphite system will not reach an energy density higher than 280 W h kg^{-1}. To achieve the target of 300 W h kg^{-1}, using NMC811 and Si–C-450 as cathode and anode materials is a good choice. Based on our calculation, 300 W h kg^{-1} can be realized when the thickness of SE is reduced to 15 μm (Fig. 20E and 21B) and the NMC811 content in the cathode composites is 85%. The corresponding volumetric energy density is 700 W h L^{-1} (Fig. 20F). It should be highlighted here that fabricating 15 μm SE membranes is technically very challenging. Further increasing the specific capacity of Si–C composites (i.e. Si–C-600) can boost the energy density of the NMC811/Si–C system to 325 W h kg^{-1}. It is estimated that 720 km per charge can be achieved using all-solid-state NMC811/Si–C-450 pouch cells with an energy density of 300 W h kg^{-1} (Fig. 21B).

(3) NMC811\|SE\|Li-40 μm with an energy density target over 350 W h kg^{-1}. Li metal is a promising anode for ASSLBs, which has been intensively investigated in recent years. Therefore, it is necessary to show the potential of ASSLBs based on Li metal, even though the ultra-thin Li metal anode has not been ready yet for practical use. Here, we further replaced the Si–C-450 composite anode with an ultra-thin Li metal sheet (40 μm) to examine the gravimetric and volumetric energy density (Fig. 20H and I). As tabulated in Table 2, the excess amount of Li metal (N/P = 2) is employed in the numerical analysis. When the 40 μm SE thickness is used, the energy density of NMC811\|Li$_6$PS$_5$Cl\|Li with 80% cathode content can easily reach 350 W h kg^{-1} and the volumetric energy density is 750 W h L^{-1}. Further reducing the thickness of SE and enhancing NMC811 content in the cathode composites can enable a higher energy density of 400 W h kg^{-1} and 885 W h L^{-1} (Fig. 21C). The upper limitations of gravimetric energy density and volumetric energy density of NMC811\|Li$_6$PS$_5$Cl\|Li cannot exceed 450 W h kg^{-1} and 1000 W h L^{-1}, respectively. Employing these solid-state pouch cells with an energy density of 400 W h kg^{-1} for EVs, the driving mileage can reach approximately 960 km (Fig. 21C).
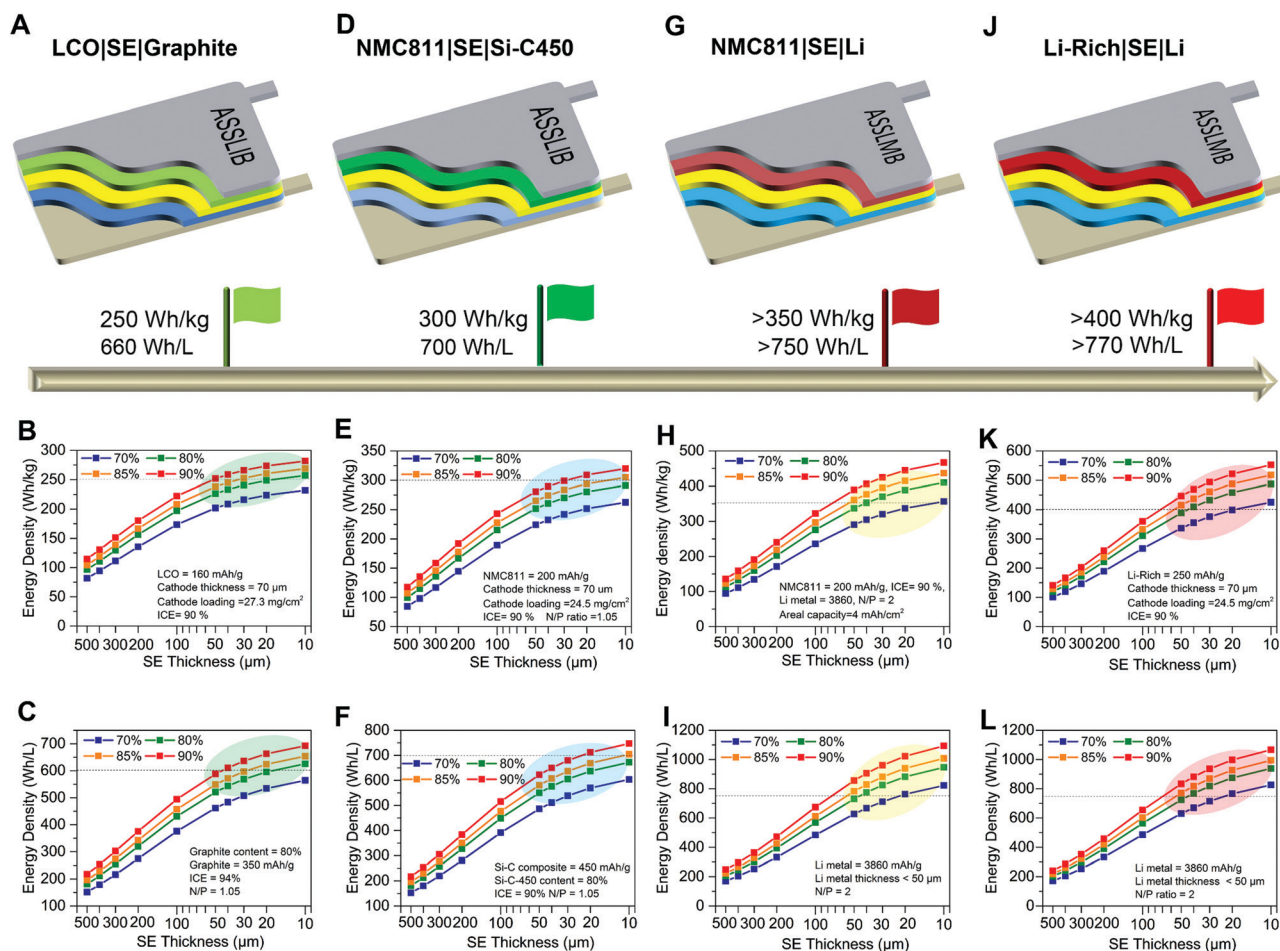
Fig. 20 Engineering design of SE-based all-solid-state pouch cells with different targets of energy density. (A) Schematic of an all-solid-state pouch cell with a configuration of LCO|Li$_6$PS$_5$Cl|graphite with an energy density target of 250 W h kg^{-1} and its gravimetric energy density (B) and volumetric energy density (C). (D) Schematic of an all-solid-state pouch cell with a structure of NMC811|Li$_6$PS$_5$Cl|Si−C-450 with a target energy density of 300 W h kg^{-1} and its gravimetric energy density (E) and volumetric energy density (F). (G) Schematic of an all-solid-state pouch cell based on NCA|Li$_6$PS$_5$Cl|Li with an energy density above 350 W h kg^{-1} and its gravimetric energy density (H) and volumetric energy density (I). (J) Schematic of an all-solid-state pouch cell based on Li-rich|Li$_6$PS$_5$Cl|Li with an energy density beyond 400 W h kg^{-1} and its gravimetric energy density (K) and volumetric energy density (L).

(4) Li-Rich/Li system with energy density beyond 400 W h kg^{-1}. It is straightforward that enhancing the capacity of cathode materials can dramatically improve the energy density of solid-state pouch cells. Taking the promising high-capacity Li-rich cathodes (typically 250 mA h g^{-1}) as an example coupled with a thin lithium metal anode of 40 μm, the energy density of Li-rich/SE/Li-40 μm can reach up to 400 W h kg^{-1} when and just 80% Li-rich materials in the cathode composite. In this case, the volumetric energy density is 705 W h L^{-1}. Comparatively, the low volumetric energy density is due to the low tap density of Li-rich composites (Table 2). The gravimetric energy density will not go beyond 550 W h kg^{-1} and the volumetric energy density will not go beyond 1100 W h L^{-1} even when an ultra-thin SE membrane of 10 μm is used. With 90% Li-rich in the cathode composites and 25 μm ultra-thin SE membranes, Li-rich/SE/Li all-solid-state pouch cells can deliver an energy density of 500 W h kg, which can allow an EV to continuous run over 1200 km (Fig. 21D).

Based on this evaluation, several solid conclusions can be drawn. First, the gravimetric energy density of SE-based

all-solid-state pouch cells cannot compete with that of conventional LIBs based liquid electrolytes because of the relatively higher density of inorganic SEs in contrast to that of liquid electrolytes. Second, the ultra-thin lithium metal anode should be used in all-solid-state pouch cells to ensure a high energy density of over 350 W h kg^{-1}. Third, reducing the thickness of SE layers can significantly improve the energy density of all-solid-state pouch cells. Ideally, the thickness of the SE membrane should be less than 30 μm. Fourth, the cathode content in the composite should be improved to 85% to obtain a high energy density of all-solid-state pouch cells based on SEs. It is believed that this systematic numerical analysis of SE-based pouch cells can serve as a standard metric for researchers and engineers to estimate the practical energy density based on the initial values tested in the mold cells in the future.

6.2 Feasible manufacturing process for mass production of all-solid-state pouch cells

To transfer the laboratory research to industrial mass production, some scientists and engineers have already examined the viability
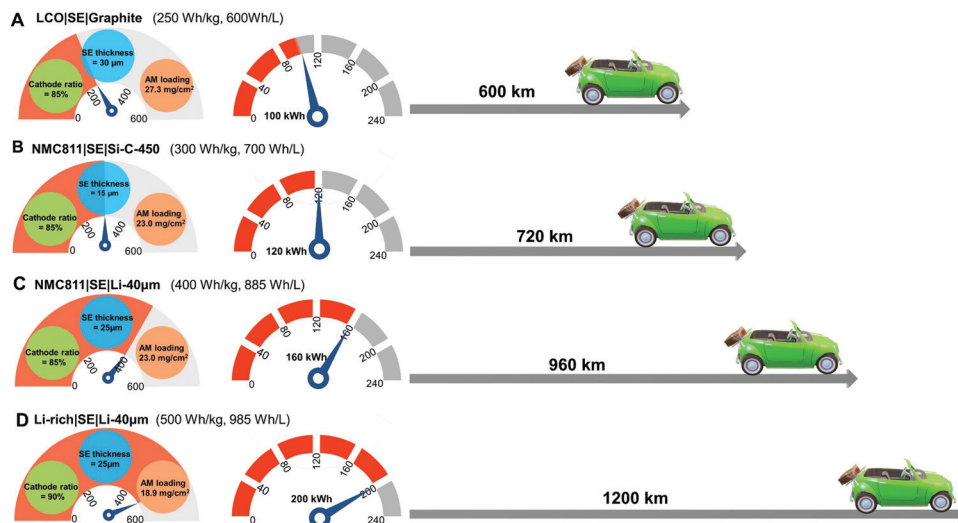
This journal is © The Royal Society of Chemistry 2021

Energy Environ. Sci., 2021, **14**, 2577–2619 | **2605**

Fig. 21 All-solid-state pouch cells on basis of various electrode systems with specific gravimetric energy density and volumetric energy density. The left dashboard indicates the key parameters for realizing all-solid-state pouch cells with specific energy density tasks. The middle dashboard diagram shows how much electricity is contained within the electric vehicle (EV). The right schematics illustrate how far the EV can drive. (A) LCO|SE|Graphite with a gravimetric energy density of 250 W h kg^{-1} and a volumetric energy density of 600 W h L^{-1}, (B) NMC811|SE|Si−C-450 with a gravimetric energy density of 300 W h kg^{-1} and a volumetric energy density of 700 W h L^{-1}. (C) NMC811|SE|40 µm Li with a gravimetric energy density of 400 W h kg^{-1} and a volumetric energy density of 885 W h L^{-1}. (D) Li-rich|SE|40 µm Li with a gravimetric energy density of 500 W h kg^{-1} and a volumetric energy density of 985 W h L^{-1}.

of ASSLIBs and identified some promising and practical processes.[65,142,246,399–403] Noticeably, J. Schnell et al. thoroughly evaluated the challenges and requirements for the industrial production of ASSLBs via joint discussion from research institutes, material suppliers, and automotive manufacturers in a workshop.[397] J. Schnell et al. systematically evaluated the processing cost of ASSLBs in comparison with that of current LIB technology.[404] It is found that the SE-based ASSLBs can be very competitive if the materials compatibility issues are solved and production is successfully scaled.[404]

An earliest SE-based all-solid-state pouch cell was demonstrated by R. Kanno et al. in 2009 which showed good cycling characteristics at a current of 0.1 mA.[142] Q. Zhang et al. recently reported fast charging ASSLBs under 6C and a 30 mm × 30 mm Li$_4$Ti$_5$O$_{12}$/Li$_7$P$_3$S$_{11}$/Li all-solid-state pouch cell was demonstrated.[368] In general, the cathode, the anode, and the SE separator can be made in three steps, including component mixing, lamination, and layer compaction. Specifically, the cathode composite fabrication process is similar to the conventional electrode fabrication process, in which active materials, solid-state SEs, binders, carbon additives are mixed to make a slurry, which can be tape-casted or extruded on a current collector, following by calendaring and/or sintering process (Fig. 22A).[405] It should be mentioned that core–shell cathode particles should be suggested to avoid the interfacial reactions between cathode particles and SEs. For graphite or Li$_4$Ti$_5$O$_{12}$ anodes, the fabrication process can be the same as the cathode composite process.[406] However, if using Li metal as the anode, the fabrication process must be re-engineered. Potential fabrication protocols for Li metal anodes include 3D printing,[407] vapor deposition, and

electrochemical platting, but the cost of these process have not been examined yet.

To enable sheet-typed solid-state electrolytes and solid-state composite electrodes for the fabrication of pouch-format ASSLBs. Besides the infiltration method discussed in Section 3.1, there are two methods: slurry coating and dry film process. Both the slurry-coating process and dry film process have been demonstrated in recent years.[408] In general, the slurry-coating process is compatible with conventional LIB production technology but has more strict requirements on binders and solvents due to the high reactivity of SEs.[260] Dry film process does not involve any solvents, which is highly promising for ASSLBs manufacturing.[409]

(1) Slurry coating process: J. Schnell et al. systematically evaluated the production process of all-solid-state batteries in comparison with that of conventional LIBs. It is suggested that composite electrode fabrication can be adapted with some effort, while the thin solid electrolyte separator and lithium metal integration require completely new processes.[397] Using slurry coating processes to fabricate sheet-typed composites electrolytes, the available solvent is restricted to nonpolar or less polar choices such as xylene, toluene, and heptane because of the severe reactivity of SEs with common polar solvents. Therefore, binder selection is also limited to nitrile-butadiene rubber (NBR). In 2018, J. Nam et al. demonstrated a wet slurry coating method using NBR as a binder and anhydrous xylene as the solvent, an all-solid-state sulfide-based pouch-type LiNi$_{0.6}$Co$_{0.2}$Mn$_{0.2}$ (NCM622)/graphite batteries with a dimension of 80 × 60 mm^2 is demonstrated (Fig. 22B).[257] Its cross-sectional SEM image clearly shows that the 30 µm SE layer is sandwiched between the NMC622 positive layer and graphite
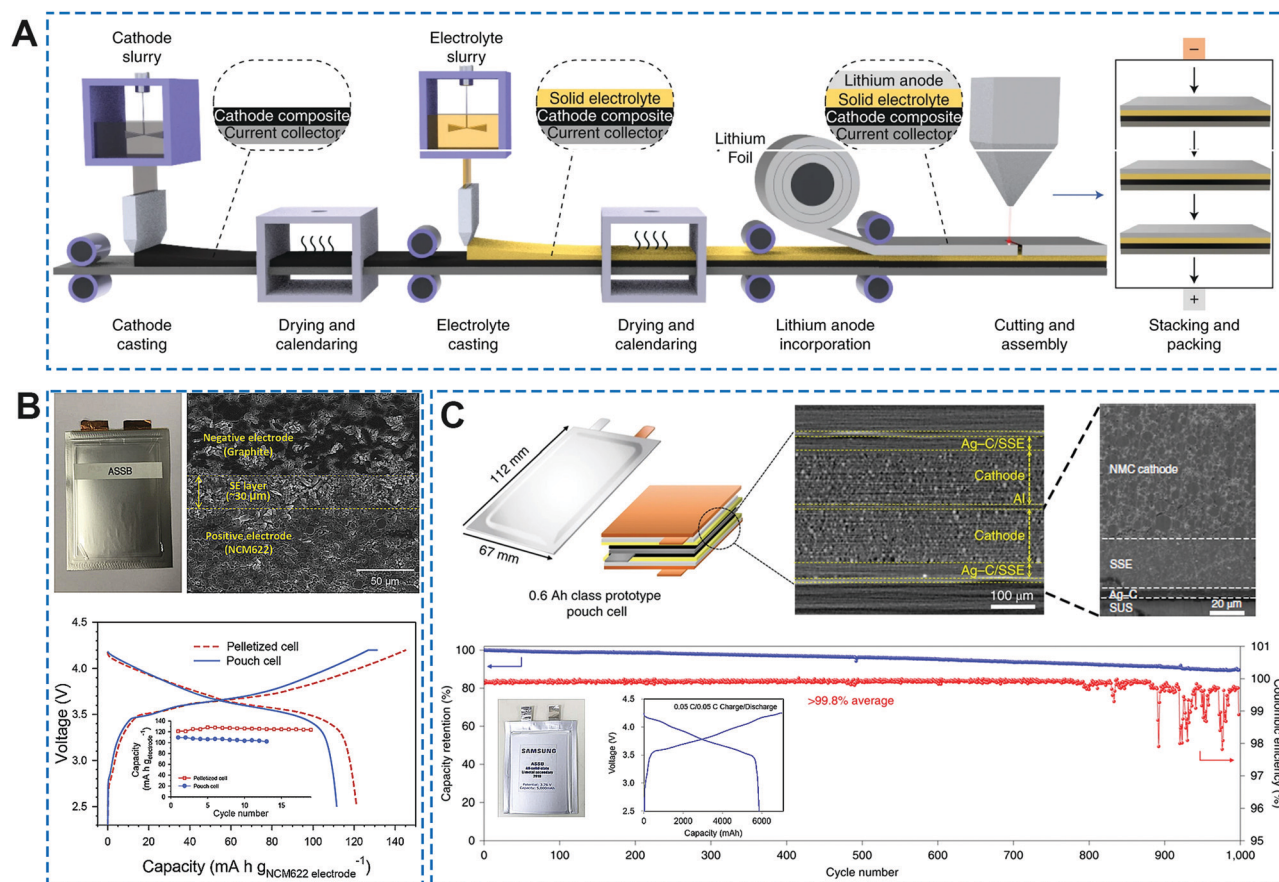
Fig. 22 Configurations of solid-state batteries and fabrication processes for performance improvement. (A) Schematic of large-scale manufacturing of ASSLBs. Reproduced with permission from ref. 328. Copyright (2020) Nature publishing group. (B) The cross-sectional SEM image of SE-based all-solid-state pouch cells based NMC622 and Graphite (8 cm × 6 cm) and the initial charge–discharge voltage profiles at 0.025C. Reproduced with permission from ref. 257. Copyright (2018) Elsevier. (C) A 0.6 A h class prototype pouch cell and illustration of a bi-cell structure. X-ray CT of the bi-cell and symmetric structure based on an aluminum current collector. Cycling performance and coulombic efficiency of the Ag–C|SE|NMC prototype pouch cell (0.6 Ah). (Inserted: A photograph and charge–discharge curves of 5 A h class all-solid-state Li metal battery.) Reproduced with permission from ref. 23. Copyright (2020) Nature Publishing Group.

anode layer. The initial charge–discharge curves of pelletized and pouch-type NCM622/graphite full-cells at 0.025C at 25 °C and 30 °C were compared. The discharge capacities for the pelletized and pouch-type NCM622/graphite full-cells were measured to be 121 mA h g^{-1} and 112 mA h g^{-1}, respectively, which corresponds to 190 W h kg^{-1} and 184 W h kg^{-1} based on the total weight of the electrodes (active materials, SEs, carbon additives, polymeric binders, and current collectors). The volumetric energy density of the pouch-type full cell was calculated to be 432 W h L^{-1}. In the study, the NBR binder was dispersed into the sheet-type electrode, which decreased the power and cycle performance of ASSLBs. M. Yamamoto et al. reported a volatile poly(propylene carbonate)-based binder which can be removed by heat treatment, thus binder-free solid-state electrolyte sheets and composite electrodes can be obtained with enhanced rate capability and excellent cycling stability.[410]

To enable both volumetric and gravimetric energy density of ASSLIBs comparable with those of commercial lithium-ion batteries, the desired thickness of the SE layer should be less than 30 μm, according to numerical analysis.[260,411–414]

Therefore, achieving thin films of solid-state electrolyte is of vital importance, although technically very challenging.[249] Y-S Jung et al. were the first to report a bendable and thin SE film reinforced with a mechanically compliant poly(para phenylene terephthalamide) nonwoven (NW) scaffold, which enabled the fabrication of free-standing and stackable ASSLBs with high energy density and high rate capabilities. The ASSLB, using a thin (~70 μm) NW-reinforced SE film, exhibited a 3-fold increase of the cell-energy-density compared to that of a conventional cell without the NW scaffold.[259] In the future, developing advanced techniques to fabricate SE thin films at a low cost is critical for the commercialization of ASSLBs.

(2) Dry film process. In contrast to the wet coating process, a dry film process does not involve any solvents, thus avoiding the negative influence of solvents in the process.[409] Recently, F. Hippauf et al. presented a promising dry film process based on a fibrous PTFE binder.[415] To ensure the high ionic conductivity of thin SE film, the binder amount in the composites was reduced to as low as 0.1 wt%, which is the lowest reported value so far.[416] Based on this method, Y.-G. Lee et al.

This journal is © The Royal Society of Chemistry 2021

Energy Environ. Sci., 2021, **14**, 2577–2619 | **2607**

demonstrated an all-solid-state lithium metal pouch cell (0.6 A h) based on high high-Ni layered oxide cathode with a high specific capacity (>210 mA h g^{-1}) of Li–Zr–O coated $LiNi_{0.90}Co_{0.05}Mn_{0.05}O_2$ and silver-carbon composite anode (Fig. 22C). A pouch cell with a high capacity of 5 A h was also constructed by multi-stacking.[23] Recently, S. Kaskel and his co-workers demonstrated $LiNi_{0.9}Co_{0.05}Mn_{0.05}O_2/Li_6PS_5Cl/Si$ pouch cells, in which a columnar silicon anode is used.[417]

Although there has been a pioneering success in fabrication pouch-cell SE-based ASSLBs, many engineering challenges remain, such as the selection of solvents, binders, slurry viscosity, quality control, and process stability. We believe that with a joint effort from academia and industry, SE-based all-solid-state pouch cells can be successfully commercialized with a reasonable cost and high energy density in the future.

7. Summary and perspectives

In summary, we systematically reviewed the most recent advances of SE-based ASSLBs from the material level, the interface level, as well as the full cell level.

At the material level, the latest development and fundamental understanding of pseudo-binary, pseudo-ternary, and pseudo-quaternary SEs were summarized with the focus of ionic conductivity, chemical stability, and electrochemical windows. Importantly, promising strategies to improve the ionic conductivity and chemical and electrochemical stability of SEs were outlined. It is clarified that the ionic conductivity of SEs can be further improved by tuning Li$^+$ concentration, Li$^+$ vacancies, and crystal structure, and site disorder. The chemical and electrochemical stability can be altered by nanostructure design and chemical composition tuning. Particularly, the HSAB theory-guided doping is very effective to develop air-stable SEs.

At the interface level, the cathodic and anodic interfacial challenges are reviewed separately. At the cathode interface, the interface reactions can be prevented *via* interfacial coatings, particularly using Li$^+$-conductive coating materials. The poor solid–solid ionic contact can be improved with soluble SEs. Volume change and SE decomposition by conductive carbon require careful engineering design toward practical solid-state pouch cells. At the anode interface, the lithium dendrite formation, volume change, and interfacial reactions are three outstanding challenges, which can be mitigated by *in situ* formed SEI. Li metal surface modification, SE modification, external pressure, and reducing electronic conductivity. However, further increasing the cycling capacity of Li metal anode (*i.e.* >4 mA h cm^{-2}) is highly desirable. Meanwhile, it is highly recommended that future work should base on the ultrathin Li foils, which could give direct insights into the practical engineering design of solid-state pouch cells. Moreover, advanced *in situ* characterization techniques, as well as first-principles theory calculations are highlighted, which provide insights into the complex interfacial issues of SE-based ASSLBs.

At the full cell level, the latest progress on all-solid-state lithium-ion batteries (ASSLIBs) and all-solid-state lithium–sulfur batteries (ASSLSBs) are reviewed. More importantly, SE-based all-solid-state pouch cells with various energy density targets from 250 W h kg^{-1} to 500 W h kg^{-1} were designed with practical engineering parameters. This engineering design with various energy density targets could serve as a quantitative framework to estimate the practical energy density of SE-based all-solid-state pouch cells in future. Moreover, conventional slurry coating technology and emerging dry electrode process are reviewed for SE-based ASSLBs manufacturing. We truly believe that this comprehensive review not only provides a fundamental and in-depth understanding of SE-based ASSLBs but also can guide the engineering design of practical all-solid-state pouch cells, thus propelling SE-based ASSLBs one step forward toward commercialization.

Although many remarkable achievements have been made in recent years, there are still many challenges yet to be addressed and more efforts are still required in the future to help realize the commercialization of SE-based ASSLBs. We list the detailed potential directions and perspectives for SE-based ASSLBs as follows.

(1) Improvements of solid-state sulfide electrolytes

(I) Improving the ionic conductivity of SEs: although some SEs exhibit a comparable ionic conductivity with those of liquid electrolytes, improving the ionic conductivity of SEs is still necessary for realizing fast-charging ASSLBs under all-weather conditions. Improving the air stability of SEs and reducing the cost is also very urgent to meet the requirement of large-scale applications. Based on the recent cost calculation,[404] the final cost of SEs should be less than 50 USD per kg. (II) Air-stability: improving the air stability of SEs now is very critical for the commercialization of SE-based ASSLBs. New strategies beyond metal oxide absorption, soft-acid doping, and nanostructure design are highly encouraged. In addition, the standard procedures to evaluate the air stability of SE should be established with the joint consideration of exposure area, exposure time, and atmospheric conditions. (III) Electrochemical stability: designing nanostructure and/or tuning the chemical composition of SEs should be further explored to improve the electrochemical windows SEs. In addition, the structural stability and thermal stability of SEs under battery abuse conditions (*i.e.* over-charge, hot-box testing) should be investigated. (IV) Reducing electronic conductivity of SEs: so far the electronic conductivity of reported SEs is about 10^{-9} S cm^{-1}. which is too high for practical application in comparison with the electronic commercial organic separators (10^{-15}–10^{-16} S cm^{-1}). The high electronic conductivity of SEs will cause the serious self-discharge of practical pouch cells and induce lithium dendrite growth along the grain boundary of SEs. Therefore, reducing the electronic conductivity of SEs either by inorganic/organic composites or elemental doping to tune the bandgap of SEs should be explored. (V) Low-cost synthesis route: new synthesis routes with the features of low cost, environmentally friendly, and high production efficiency should be developed

2608 | *Energy Environ. Sci.*, 2021, **14**, 2577–2619

This journal is © The Royal Society of Chemistry 2021

for large-scale production of SEs. (VI) Alternative ionic conductors: discovering new solid electrolytes with high ionic conductivity, high chemical stability, wide electrochemical windows, and low cost is highly desirable, such as reviving research interests into halide electrolytes (*e.g.* Li_3MX_6, M = In, Y, Sc, Er, *etc.*, X = Cl, Br, I).

(2) Overcoming interfacial challenges of SE-based ASSLBs

Cathode interface: (I) interfacial coating requirements; interfacial coatings are required to suppress the interfacial reactions at the cathode interface and lithium dendrite growth at the anode interface. The electronic and ionic conductivity of interfacial coating layers should be investigated to figure out the basic requirements of interfacial layers. Besides, the long-term stability of interfacial coatings during cycling and upon heating should be investigated. Moreover, multilayer interfacial layers with different electrochemical windows or different mechanical stability, such as an inorganic–organic hybrid coating, should be developed to suppress reduction/oxidization reactions by electrodes and accommodate the volume change of electrode upon cycling. (II) Interfacial coating method; sol–gel method and fluidized bed were widely used to develop interfacial coatings on cathode particles. However, these methods are very difficult to control the thickness and uniformity. Atomic layer deposition (ALD) and molecular layer deposition (MLD) with atomic-level controllability in thickness and chemical composition should be further explored in SE-based ASSLBs. (III) Soluble SE for ionic contact; interfacial ionic contact between the electrode and SEs can be improved by soluble SE coating. However, improving the ionic conductivity of soluble SEs is urgently required for designing high-power solid-state batteries. (IV) Interface wetting agents; only using SE in the cathode would not resolve all the issues, particularly for significant volume change upon long-term cycling. Therefore, interfacial wetting agents with high ionic conductivity would be necessary, such as Li^+-conductive elastomer, SE-compatible ionic liquids, deep eutectic solvents. It should be mentioned that these interfacial wetting agents should be thermally and electrochemically stable against SEs, lost-cost, and not compromise the safety of SE-based ASSLBs. (V) High loading cathode composites; to ensure the high energy density of ASSLBs, the SE content in the cathode composites should be minimized to less than 15% without sacrificing the solid–solid interface contact. In addition, high loading cathode composites with a large areal capacity (>4 mA h cm^{-2}) should be carefully engineered to balance the electron and electron transport. (VI) Gassing behavior of SE-ASSLBs; it is well known that layered transition metal oxides are easy to release oxygen under moderate temperatures or high operating voltages (>4.5 V *vs.* Li^+/Li).[359,418,419] Therefore it is important to take gas evolution into account in ASSLBs and its coincident interfacial reactions and safety hazards.

Anode interface: (I) ultrathin Li foil with high capacity and high coulombic efficiency: to meet the practical engineering requirements, future work should base on ultrathin Li foils other than thick Li pellets. In addition, a large cycling capacity of Li metal (>4 mA h cm^{-2}) needs to be achieved. Furthermore,

the coulombic efficiency of Li metal in solid-state batteries should be investigated to guarantee long-term stable cycling of SE-based ASSLBs. Advanced Li-alloys should also be explored in SE-based ASSLBs. (II) Safety of ultrathin Li foils: the melting point of Li metal is only 180.5 °C. Therefore, the safety of solid-state lithium metal batteries should be examined systematically. (III) Advanced characterizations: advanced characterization techniques, particularly *in situ* techniques, are always encouraged to probe in-depth interfacial information at both anode and cathode interfaces of SE-based ASSLBs.

(3) Perspectives of SE-based ASSLSBs

To realize SE-based ASSLSBs, several key challenges should be addressed. (I) Improve the electronic and ionic conductivity of sulfur cathode composites: a three-phase interface between active materials, carbon additives, and SEs should be carefully designed to achieve high capacity and long cycling stability of ASSLSBs. Ideally, the electronic conduction path and ionic conduction path should be separated to avoid the detrimental interfacial reactions between carbon additives and SEs. (II) Accommodate volume change of sulfur cathodes: considerable volume change of sulfur cathodes in ASSLSBs occur and should be alleviated, particularly for high-loading sulfur cathodes. A potential strategy is to add some soft and ionic-conductive materials in sulfur cathode composites to ensure intimate solid–solid ionic contact after volume change. (III) Realize high-loading sulfur cathodes: the sulfur loading in reported ASSLSBs is insufficient in previous reports.[420] Based on our calculations, sulfur loading in the cathode composites should be improved to 6 mg cm^{-2} to realize a SE-based ASSLSB with an energy density of 600 W h kg^{-1}. Simultaneously, high sulfur utilization in the high-loading sulfur cathodes and high-capacity (>4 mA h cm^{-2}) lithium metal anodes should be met.

(4) Mass production of SE-based ASSLB pouch cells

Although manufacturing processes have been proposed and some prototypes of SE-based ASSLBs have been successfully demonstrated, the remaining engineering challenges, such as solvent and binder selection criteria, quality control, compatible battery management systems, material cost, and manufacturing cost should be addressed in the future. (I) Ultrathin SE membranes: the ultrathin SE membrane with a thickness of less than 30 μm is desired to fulfill the high energy density of ASSLBs.[260,421] Besides, the internal resistance of less than about 40 Ω cm^2 should be realized to enable 1C cycling with more than 90% energy efficiency. Therefore, advanced methods to fabricate ultrathin SE membranes with high ionic conductivity (>1 mS cm^{-1}) should be developed. To ensure the good mechanical property of such a thin SE membrane, incorporation of a small portion of chemically compatible polymer electrolytes would be expected. (II) Tape casting process: although the tape casting process has been widely demonstrated in previous work, the engineering optimization of solvents, binders, and quality control, and manufacturing cost still requires more effort. (III) Dry electrode process: the dry

This journal is © The Royal Society of Chemistry 2021

Energy Environ. Sci., 2021, **14**, 2577–2619 | **2609**

electrode process that avoids the negative effects of organic solvent on SEs requires more research efforts in the future. (IV) Testing condition: so far, most pouch-type pouch cells are tested under external pressures. The optimal testing pressure should be investigated. In addition, how to apply the pressure for solid-state pouch cell operation in the practical application should be considered. If possible, removing the testing pressure would make the real application much more convenient.

Foreseeably, with increased endeavors to overcome the highlighted challenges, SE-based ASSLBs with high energy densities and great safety can be realized for wide applications in a myriad of products including electric vehicles, smart grids, consumer electronics, and even flexible electronics in the future.

Author contributions

X. Sun supervised the overall work; C. Wang designed and wrote the whole review; J. Liang and Y. Zhao, X. Li gave suggestions on the sulfide electrolyte part, the interface part, solid-state Li–S part, respectively. M. Zheng carefully polished the language. All authors read and commented on the manuscript.

Conflicts of interest

The authors declare no conflicts of interest.

Acknowledgements

References

1 J. M. Tarascon and M. Armand, *Nature*, 2001, **414**, 359–367.
2 K. Xu, *Chem. Rev.*, 2004, **104**, 4303–4418.
3 J. W. Choi and D. Aurbach, *Nat. Rev. Mater.*, 2016, **1**, 16013.
4 Y. Zhao, K. Zheng and X. Sun, *Joule*, 2018, 1–22.
5 J. Hao, L. Yuan, C. Ye, D. Chao, K. Davey, Z. Guo and S.-Z. Qiao, *Angew. Chem., Int. Ed.*, 2021, **60**, 7366–7375.
6 M. Wang, X. Zheng, X. Zhang, D. Chao, S.-Z. Qiao, H. N. Alshareef, Y. Cui and W. Chen, *Adv. Energy Mater.*, 2021, **11**, 2002904.
7 F. Xie, H. Li, X. Wang, X. Zhi, D. Chao, K. Davey and S.-Z. Qiao, *Adv. Energy Mater.*, 2021, **11**, 2003419.
8 D. Chao, C. Ye, F. Xie, W. Zhou, Q. Zhang, Q. Gu, K. Davey, L. Gu and S.-Z. Qiao, *Adv. Mater.*, 2020, **32**, 2001894.

9 X. Yuan, F. Ma, L. Zuo, J. Wang, N. Yu, Y. Chen, Y. Zhu, Q. Huang, R. Holze, Y. Wu and T. van Ree, *Electrochem. Energy Rev.*, 2021, **4**, 1–34.
10 D. Chao and S.-Z. Qiao, *Joule*, 2020, **4**, 1846–1851.
11 D. Chao, W. Zhou, F. Xie, C. Ye, H. Li, M. Jaroniec and S.-Z. Qiao, *Sci. Adv.*, 2020, **6**, eaba4098.
12 A. Manthiram, X. Yu and S. Wang, *Nat. Rev. Mater.*, 2017, **2**, 16103.
13 R. Chen, Q. Li, X. Yu, L. Chen and H. Li, *Chem. Rev.*, 2020, **120**, 6820–6877.
14 Q. Zhang, D. Cao, Y. Ma, A. Natan, P. Aurora and H. Zhu, *Adv. Mater.*, 2019, **31**, 1901131.
15 Y. Kato, S. Hori, T. Saito, K. Suzuki, M. Hirayama, A. Mitsui, M. Yonemura, H. Iba and R. Kanno, *Nat. Energy*, 2016, **1**, 16030.
16 Q. Zhao, S. Stalin, C.-Z. Zhao and L. A. Archer, *Nat. Rev. Mater.*, 2020, **5**, 229–252.
17 M. Jia, N. Zhao, H. Huo and X. Guo, *Electrochem. Energy Rev.*, 2020, **3**, 656–689.
18 H. Duan, W.-P. Chen, M. Fan, W.-P. Wang, L. Yu, S.-J. Tan, X. Chen, Q. Zhang, S. Xin, L.-J. Wan and Y.-G. Guo, *Angew. Chem., Int. Ed.*, 2020, **59**, 12069–12075.
19 H. Duan, J. Zhang, X. Chen, X.-D. Zhang, J.-Y. Li, L.-B. Huang, X. Zhang, J.-L. Shi, Y.-X. Yin, Q. Zhang, Y.-G. Guo, L. Jiang and L.-J. Wan, *J. Am. Chem. Soc.*, 2018, **140**, 18051–18057.
20 H. Huo, Y. Chen, J. Luo, X. Yang, X. Guo and X. Sun, *Adv. Energy Mater.*, 2019, **9**, 1804004.
21 Z. Jiang, S. Wang, X. Chen, W. Yang, X. Yao, X. Hu, Q. Han and H. Wang, *Adv. Mater.*, 2020, **32**, 1906221.
22 A. Miura, N. C. Rosero-Navarro, A. Sakuda, K. Tadanaga, N. H. H. Phuc, A. Matsuda, N. Machida, A. Hayashi and M. Tatsumisago, *Nat. Rev. Chem.*, 2019, **3**, 189–198.
23 Y.-G. Lee, S. Fujiki, C. Jung, N. Suzuki, N. Yashiro, R. Omoda, D.-S. Ko, T. Shiratsuchi, T. Sugimoto, S. Ryu, J. H. Ku, T. Watanabe, Y. Park, Y. Aihara, D. Im and I. T. Han, *Nat. Energy*, 2020, **5**, 299–308.
24 L. Yue, J. Ma, J. Zhang, J. Zhao, S. Dong, Z. Liu, G. Cui and L. Chen, *Energy Storage Mater.*, 2016, **5**, 139–164.
25 J. Zhang, J. Zhao, L. Yue, Q. Wang, J. Chai, Z. Liu, X. Zhou, H. Li, Y. Guo, G. Cui and L. Chen, *Adv. Energy Mater.*, 2015, **5**, 1501082.
26 D. Lin, P. Y. Yuen, Y. Liu, W. Liu, N. Liu, R. H. Dauskardt and Y. Cui, *Adv. Mater.*, 2018, **30**, 1802661.
27 J. Wu, Z. Rao, Z. Cheng, L. Yuan, Z. Li and Y. Huang, *Adv. Energy Mater.*, 2019, **9**, 1902767.
28 Q. Zhao, X. Liu, S. Stalin, K. Khan and L. A. Archer, *Nat. Energy*, 2019, **4**, 365–373.
29 Z. Zhu, M. Hong, D. Guo, J. Shi, Z. Tao and J. Chen, *J. Am. Chem. Soc.*, 2014, **136**, 16461–16464.
30 D. Park, H. Park, Y. Lee, S.-O. Kim, H.-G. Jung, K. Y. Chung, J. H. Shim and S. Yu, *ACS Appl. Mater. Interfaces*, 2020, **12**, 34806–34814.
31 R. Schlem, A. Banik, M. Eckardt, M. Zobel and W. G. Zeier, *ACS Appl. Energy Mater.*, 2020, **3**, 10164–10173.
32 R. Schlem, S. Muy, N. Prinz, A. Banik, Y. Shao-Horn, M. Zobel and W. G. Zeier, *Adv. Energy Mater.*, 2020, **10**, 1903719.

2610 | *Energy Environ. Sci.*, 2021, **14**, 2577–2619

This journal is © The Royal Society of Chemistry 2021

33 T. Asano, A. Sakai, S. Ouchi, M. Sakaida, A. Miyazaki and S. Hasegawa, *Adv. Mater.*, 2018, **0**, 1803075.

34 S. Wang, Q. Bai, A. M. Nolan, Y. Liu, S. Gong, Q. Sun and Y. Mo, *Angew. Chem., Int. Ed.*, 2019, **58**, 8039–8043.

35 L. Riegger, R. Schlem, J. Sann, W. G. Zeier and J. Janek, *Angew. Chem., Int. Ed.*, 2020, **60**, 6718–6723.

36 X. Li, J. Liang, J. Luo, M. Norouzi Banis, C. Wang, W. Li, S. Deng, C. Yu, F. Zhao, Y. Hu, T.-K. Sham, L. Zhang, S. Zhao, S. Lu, H. Huang, R. Li, K. R. Adair and X. Sun, *Energy Environ. Sci.*, 2019, **12**, 2665–2671.

37 X. Li, J. Liang, X. Yang, K. R. Adair, C. Wang, F. Zhao and X. Sun, *Energy Environ. Sci.*, 2020, **13**, 1429–1461.

38 L. Zhou, C. Y. Kwok, A. Shyamsunder, Q. Zhang, X. Wu and L. F. Nazar, *Energy Environ. Sci.*, 2020, **13**, 2056–2063.

39 J. Liang, X. Li, S. Wang, K. R. Adair, W. Li, Y. Zhao, C. Wang, Y. Hu, L. Zhang and S. Zhao, *J. Am. Chem. Soc.*, 2020, **142**, 7012–7022.

40 C. Wang, J. Liang, M. Jiang, X. Li, S. Mukherjee, K. Adair, M. Zheng, Y. Zhao, F. Zhao, S. Zhang, R. Li, H. Huang, S. Zhao, L. Zhang, S. Lu, C. V. Singh and X. Sun, *Nano Energy*, 2020, **76**, 105015.

41 X. Li, J. Liang, K. R. Adair, J. Li, W. Li, F. Zhao, Y. Hu, T.-K. Sham, L. Zhang, S. Zhao, S. Lu, H. Huang, R. Li, N. Chen and X. Sun, *Nano Lett.*, 2020, **20**, 4384–4392.

42 H. Kwak, D. Han, J. Lyoo, J. Park, S. H. Jung, Y. Han, G. Kwon, H. Kim, S.-T. Hong, K.-W. Nam and Y. S. Jung, *Adv. Energy Mater.*, 2021, 2003190, DOI: 10.1002/aenm.202003190.

43 W. S. Tang, M. Matsuo, H. Wu, V. Stavila, W. Zhou, A. A. Talin, A. V. Soloninin, R. V. Skoryunov, O. A. Babanova, A. V. Skripov, A. Unemoto, S.-I. Orimo and T. J. Udovic, *Adv. Energy Mater.*, 2016, **6**, 1502237.

44 Y. Yan, R.-S. Kühnel, A. Remhof, L. Duchêne, E. C. Reyes, D. Rentsch, Z. Łodziana and C. Battaglia, *Adv. Energy Mater.*, 2017, **7**, 1700294.

45 J. Cuan, Y. Zhou, T. Zhou, S. Ling, K. Rui, Z. Guo, H. Liu and X. Yu, *Adv. Mater.*, 2019, **31**, 1803533.

46 D. Sveinbjörnsson, A. S. Christiansen, R. Viskinde, P. Norby and T. Vegge, *J. Electrochem. Soc.*, 2014, **161**, A1432–A1439.

47 M. Matsuo, A. Remhof, P. Martelli, R. Caputo, M. Ernst, Y. Miura, T. Sato, H. Oguchi, H. Maekawa, H. Takamura, A. Borgschulte, A. Züttel and S.-i. Orimo, *J. Am. Chem. Soc.*, 2009, **131**, 16389–16391.

48 S. Kim, H. Oguchi, N. Toyama, T. Sato, S. Takagi, T. Otomo, D. Arunkumar, N. Kuwata, J. Kawamura and S.-i. Orimo, *Nat. Commun.*, 2019, **10**, 1081.

49 X. Lü, J. W. Howard, A. Chen, J. Zhu, S. Li, G. Wu, P. Dowden, H. Xu, Y. Zhao and Q. Jia, *Adv. Sci.*, 2016, **3**, 1500359.

50 X. Lu, G. Wu, J. W. Howard, A. Chen, Y. Zhao, L. L. Daemen and Q. Jia, *Chem. Commun.*, 2014, **50**, 11520–11522.

51 J. A. Dawson, T. S. Attari, H. Chen, S. P. Emge, K. E. Johnston and M. S. Islam, *Energy Environ. Sci.*, 2018, **11**, 2993–3002.

52 A. Emly, E. Kioupakis and A. Van der Ven, *Chem. Mater.*, 2013, **25**, 4663–4670.

53 H. H. Heenen, J. Voss, C. Scheurer, K. Reuter and A. C. Luntz, *J. Phys. Chem. Lett.*, 2019, **10**, 2264–2269.

54 L. Chen, Y. Li, S.-P. Li, L.-Z. Fan, C.-W. Nan and J. B. Goodenough, *Nano Energy*, 2018, **46**, 176–184.

55 Y. Tian, F. Ding, H. Zhong, C. Liu, Y.-B. He, J. Liu, X. Liu and Q. Xu, *Energy Storage Mater.*, 2018, **14**, 49–57.

56 X. Zhu, K. Wang, Y. Xu, G. Zhang, S. Li, C. Li, X. Zhang, X. Sun, X. Ge and Y. Ma, *Energy Storage Mater.*, 2021, **36**, 291–308.

57 F. P. McGrogan, T. Swamy, S. R. Bishop, E. Eggleton, L. Porz, X. Chen, Y. M. Chiang and K. J. Van Vliet, *Adv. Energy Mater.*, 2017, 1602011.

58 J. Wu, S. Liu, F. Han, X. Yao and C. Wang, *Adv. Mater.*, 2021, **33**, 2000751.

59 T. Minami, A. Hayashi and M. Tatsumisago, *Solid State Ionics*, 2006, **177**, 2715–2720.

60 Y. S. Jung, D. Y. Oh, Y. J. Nam and K. H. Park, *Isr. J. Chem.*, 2015, **55**, 472–485.

61 S. P. Culver, R. Koerver, W. G. Zeier and J. Janek, *Adv. Energy Mater.*, 2019, **0**, 1900626.

62 S. Chen, D. Xie, G. Liu, J. P. Mwizerwa, Q. Zhang, Y. Zhao, X. Xu and X. Yao, *Energy Storage Mater.*, 2018, **14**, 58–74.

63 R. Xu, F. Han, X. Ji, X. Fan, J. Tu and C. Wang, *Nano Energy*, 2018, **53**, 958–966.

64 J. Lau, R. H. DeBlock, D. M. Butts, D. S. Ashby, C. S. Choi and B. S. Dunn, *Adv. Energy Mater.*, 2018, **8**, 1800933.

65 K. H. Park, Q. Bai, D. H. Kim, D. Y. Oh, Y. Zhu, Y. Mo and Y. S. Jung, *Adv. Energy Mater.*, 2018, **8**, 1800035.

66 Y. Kato, S. Hori and R. Kanno, *Adv. Energy Mater.*, 2020, 2002153.

67 M. Ribes and S. JL, *Rev. Chim. Miner.*, 1979, **16**, 339–348.

68 R. Mercier, J.-P. Malugani, B. Fahys and G. Robert, *Solid State Ionics*, 1981, **5**, 663–666.

69 H. Wada, M. Menetrier, A. Levasseur and P. Hagenmuller, *Mater. Res. Bull.*, 1983, **18**, 189–193.

70 V. K. Deshpande, A. Pradel and M. Ribes, *Mater. Res. Bull.*, 1988, **23**, 379–384.

71 M. Tachez, J.-P. Malugani, R. Mercier and G. Robert, *Solid State Ionics*, 1984, **14**, 181–185.

72 R. Kanno and M. Murayama, *J. Electrochem. Soc.*, 2001, **148**, A742–A746.

73 N. Kamaya, K. Homma, Y. Yamakawa, M. Hirayama, R. Kanno, M. Yonemura, T. Kamiyama, Y. Kato, S. Hama, K. Kawamoto and A. Mitsui, *Nat. Mater.*, 2011, **10**, 682–686.

74 S. Wenzel, T. Leichtweiss, D. A. Weber, J. Sann, W. G. Zeier and J. Janek, *ACS Appl. Mater. Interfaces*, 2016, **8**, 28216–28224.

75 H. Huang, H.-H. Wu, X. Wang, B. Huang and T.-Y. Zhang, *Phys. Chem. Chem. Phys.*, 2018, **20**, 20525–20533.

76 W. D. Richards, T. Tsujimura, L. J. Miara, Y. Wang, J. C. Kim, S. P. Ong, I. Uechi, N. Suzuki and G. Ceder, *Nat. Commun.*, 2016, **7**, 11009.

77 R. Iwasaki, S. Hori, R. Kanno, T. Yajima, D. Hirai, Y. Kato and Z. Hiroi, *Chem. Mater.*, 2019, **31**, 3694–3699.

78 F. Mizuno, A. Hayashi, K. Tadanaga and M. Tatsumisago, *Adv. Mater.*, 2005, **17**, 918–921.

This journal is © The Royal Society of Chemistry 2021

Energy Environ. Sci., 2021, **14**, 2577–2619 | **2611**

79 Y. Seino, T. Ota, K. Takada, A. Hayashi and M. Tatsumisago, *Energy Environ. Sci.*, 2014, **7**, 627–631.

80 H.-J. Deiseroth, S.-T. Kong, H. Eckert, J. Vannahme, C. Reiner, T. Zaiß and M. Schlosser, *Angew. Chem., Int. Ed.*, 2008, **47**, 755–758.

81 O. Pecher, S.-T. Kong, T. Goebel, V. Nickel, K. Weichert, C. Reiner, H.-J. Deiseroth, J. Maier, F. Haarmann and D. Zahn, *Chem. – Eur. J.*, 2010, **16**, 8347–8354.

82 M. A. Kraft, S. Ohno, T. Zinkevich, R. Koerver, S. P. Culver, T. Fuchs, A. Senyshyn, S. Indris, B. J. Morgan and W. G. Zeier, *J. Am. Chem. Soc.*, 2018, **140**, 16330–16339.

83 S.-T. Kong, H.-J. Deiseroth, C. Reiner, Ö. Gün, E. Neumann, C. Ritter and D. Zahn, *Chem. – Eur. J.*, 2010, **16**, 2198–2206.

84 F. Zhao, J. Liang, C. Yu, Q. Sun, X. Li, K. Adair, C. Wang, Y. Zhao, S. Zhang, W. Li, S. Deng, R. Li, Y. Huang, H. Huang, L. Zhang, S. Zhao, S. Lu and X. Sun, *Adv. Energy Mater.*, 2020, **10**, 1903422.

85 W. D. Jung, J.-S. Kim, S. Choi, S. Kim, M. Jeon, H.-G. Jung, K. Y. Chung, J.-H. Lee, B.-K. Kim, J.-H. Lee and H. Kim, *Nano Lett.*, 2020, **20**, 2303–2309.

86 L. Zhou, A. Assoud, Q. Zhang, X. Wu and L. F. Nazar, *J. Am. Chem. Soc.*, 2019, **141**, 19002–19013.

87 P. Adeli, J. D. Bazak, A. Huq, G. R. Goward and L. F. Nazar, *Chem. Mater.*, 2021, **33**, 146–157.

88 Y. Lee, J. Jeong, H.-D. Lim, S.-O. Kim, H.-G. Jung, K. Y. Chung and S. Yu, *ACS Sustainable Chem. Eng.*, 2021, **9**, 120–128.

89 Y. Sun, K. Suzuki, S. Hori, M. Hirayama and R. Kanno, *Chem. Mater.*, 2017, **29**, 5858–5864.

90 M. Tatsumisago, M. Nagao and A. Hayashi, *J. Asian Ceram. Soc.*, 2013, **1**, 17–25.

91 H. Yamane, M. Shibata, Y. Shimane, T. Junke, Y. Seino, S. Adams, K. Minami, A. Hayashi and M. Tatsumisago, *Solid State Ionics*, 2007, **178**, 1163–1167.

92 Z. Deng, Z. Zhu, I.-H. Chu and S. P. Ong, *Chem. Mater.*, 2017, **29**, 281–288.

93 J. Liang, N. Chen, X. Li, X. Li, K. R. Adair, J. Li, C. Wang, C. Yu, M. Norouzi Banis and L. Zhang, *Chem. Mater.*, 2020, **32**, 2664–2672.

94 A. Hayashi, S. Hama, H. Morimoto, M. Tatsumisago and T. Minami, *J. Am. Ceram. Soc.*, 2001, **84**, 477–479.

95 A. Hayashi, S. Hama, T. Minami and M. Tatsumisago, *Electrochem. Commun.*, 2003, **5**, 111–114.

96 F. Mizuno, A. Hayashi, K. Tadanaga and M. Tatsumisago, *Solid State Ionics*, 2006, **177**, 2721–2725.

97 Z. Liu, W. Fu, E. A. Payzant, X. Yu, Z. Wu, N. J. Dudney, J. Kiggans, K. Hong, A. J. Rondinone and C. Liang, *J. Am. Chem. Soc.*, 2013, **135**, 975–978.

98 G. Sahu, Z. Lin, J. Li, Z. Liu, N. Dudney and C. Liang, *Energy Environ. Sci.*, 2014, **7**, 1053–1058.

99 H.-J. Deiseroth, J. Maier, K. Weichert, V. Nickel, S.-T. Kong and C. Reiner, *Z. Anorg. Allg. Chem.*, 2011, **637**, 1287–1294.

100 A. Kuhn, O. Gerbig, C. Zhu, F. Falkenberg, J. Maier and B. V. Lotsch, *Phys. Chem. Chem. Phys.*, 2014, **16**, 14669–14674.

101 P. Bron, S. Johansson, K. Zick, J. Schmedt auf der Günne, S. Dehnen and B. Roling, *J. Am. Chem. Soc.*, 2013, **135**, 15694–15697.

102 H. Morimoto, H. Yamashita, M. Tatsumisago and T. Minami, *J. Am. Ceram. Soc.*, 1999, **82**, 1352–1354.

103 H. Yamashita, A. Hayashi, H. Morimoto, M. Tatsumisago, T. Minami and Y. Miura, *J. Ceram. Soc. Jpn.*, 2000, **108**, 973–978.

104 M. Murayama, R. Kanno, Y. Kawamoto and T. Kamiyama, *Solid State Ionics*, 2002, **154–155**, 789–794.

105 R. Kanno, T. Hata, Y. Kawamoto and M. Irie, *Solid State Ionics*, 2000, **130**, 97–104.

106 J. H. MacNeil, D. M. Massi, J.-H. Zhang, K. A. Rosmus, C. D. Brunetta, T. A. Gentile and J. A. Aitken, *J. Alloys Compd.*, 2014, **586**, 736–744.

107 M. Murayama, N. Sonoyama, A. Yamada and R. Kanno, *Solid State Ionics*, 2004, **170**, 173–180.

108 K. Minami, A. Hayashi and M. Tatsumisago, *J. Am. Ceram. Soc.*, 2011, **94**, 1779–1783.

109 T. Kaib, S. Haddadpour, M. Kapitein, P. Bron, C. Schröder, H. Eckert, B. Roling and S. Dehnen, *Chem. Mater.*, 2012, **24**, 2211–2219.

110 G. Sahu, E. Rangasamy, J. Li, Y. Chen, K. An, N. Dudney and C. Liang, *J. Mater. Chem. A*, 2014, **2**, 10396–10403.

111 A. Al-Qawasmeh and N. A. W. Holzwarth, *J. Electrochem. Soc.*, 2016, **163**, A2079–A2088.

112 M. Murayama, R. Kanno, M. Irie, S. Ito, T. Hata, N. Sonoyama and Y. Kawamoto, *J. Solid State Chem.*, 2002, **168**, 140–148.

113 A. Hayashi, H. Yamashita, M. Tatsumisago and T. Minami, *Solid State Ionics*, 2002, **148**, 381–389.

114 K. Minami, A. Hayashi and M. Tatsumisago, *Solid State Ionics*, 2008, **179**, 1282–1285.

115 Y.-Z. Sun, J.-Q. Huang, C.-Z. Zhao and Q. Zhang, *Sci. China: Chem.*, 2017, **60**, 1508–1526.

116 S. Hori, K. Suzuki, M. Hirayama, Y. Kato, T. Saito, M. Yonemura and R. Kanno, *Faraday Discuss.*, 2014, **176**, 83–94.

117 P. Zhou, J. Wang, F. Cheng, F. Li and J. Chen, *Chem. Commun.*, 2016, **52**, 6091–6094.

118 R. P. Rao and S. Adams, *Phys. Status Solidi A*, 2011, **208**, 1804–1807.

119 S. Boulineau, M. Courty, J.-M. Tarascon and V. Viallet, *Solid State Ionics*, 2012, **221**, 1–5.

120 E. Rangasamy, Z. Liu, M. Gobet, K. Pilar, G. Sahu, W. Zhou, H. Wu, S. Greenbaum and C. Liang, *J. Am. Chem. Soc.*, 2015, **137**, 1384–1387.

121 R.-c. Xu, X.-h. Xia, S.-h. Li, S.-z. Zhang, X.-l. Wang and J.-p. Tu, *J. Mater. Chem. A*, 2017, **5**, 6310–6317.

122 K. Kaup, J. D. Bazak, S. H. Vajargah, X. Wu, J. Kulisch, G. R. Goward and L. F. Nazar, *Adv. Energy Mater.*, 2020, **10**, 1902783.

123 K. Kaup, L. Zhou, A. Huq and L. F. Nazar, *J. Mater. Chem. A*, 2020, **8**, 12446–12456.

124 R. Makiura, T. Yonemura, T. Yamada, M. Yamauchi, R. Ikeda, H. Kitagawa, K. Kato and M. Takata, *Nat. Mater.*, 2009, **8**, 476–480.

125 Y. G. Guo, J. S. Lee and J. Maier, *Adv. Mater.*, 2005, **17**, 2815–2819.

2612 | *Energy Environ. Sci.*, 2021, **14**, 2577–2619

This journal is © The Royal Society of Chemistry 2021

126 Y. Yang, Q. Wu, Y. Cui, Y. Chen, S. Shi, R.-Z. Wang and H. Yan, *ACS Appl. Mater. Interfaces*, 2016, **8**, 25229–25242.

127 A. Hayashi, K. Minami, S. Ujiie and M. Tatsumisago, *J. Non-Cryst. Solids*, 2010, **356**, 2670–2673.

128 M. R. Busche, D. A. Weber, Y. Schneider, C. Dietrich, S. Wenzel, T. Leichtweiss, D. Schröder, W. Zhang, H. Weigand, D. Walter, S. J. Sedlmaier, D. Houtarde, L. F. Nazar and J. Janek, *Chem. Mater.*, 2016, **28**, 6152–6165.

129 A. Sakuda, A. Hayashi and M. Tatsumisago, *Sci. Rep.*, 2013, **3**, 2261.

130 Z. Liu, S. Ma, J. Liu, S. Xiong, Y. Ma and H. Chen, *ACS Energy Lett.*, 2021, **6**, 298–304.

131 D. A. Ziolkowska, W. Arnold, T. Druffel, M. Sunkara and H. Wang, *ACS Appl. Mater. Interfaces*, 2019, **11**, 6015–6021.

132 M. Ghidiu, J. Ruhl, S. P. Culver and W. G. Zeier, *J. Mater. Chem. A*, 2019, **7**, 17735–17753.

133 N. Phuc, K. Morikawa, T. Mitsuhiro, H. Muto and A. Matsuda, *Ionics*, 2017, **23**, 2061–2067.

134 M. Calpa, N. C. Rosero-Navarro, A. Miura and K. Tadanaga, *Inorg. Chem. Front.*, 2018, **5**, 501–508.

135 X. Yao, D. Liu, C. Wang, P. Long, G. Peng, Y.-S. Hu, H. Li, L. Chen and X. Xu, *Nano Lett.*, 2016, **16**, 7148–7154.

136 Q. Zhang, H. Wan, G. Liu, Z. Ding, J. P. Mwizerwa and X. Yao, *Nano Energy*, 2019, **57**, 771–782.

137 K. Minami, A. Hayashi and M. Tatsumisago, *J. Ceram. Soc. Jpn.*, 2010, **118**, 305–308.

138 Y. Wang, D. Lu, M. Bowden, P. Z. El Khoury, K. S. Han, Z. D. Deng, J. Xiao, J.-G. Zhang and J. Liu, *Chem. Mater.*, 2018, **30**, 990–997.

139 J. Ruhl, L. M. Riegger, M. Ghidiu and W. G. Zeier, *Adv. Energy Sustainability Res.*, 2021, **2**, 2000077.

140 J. Peng, Y. Liu, Y. Pan, J. Wu, Y. Su, Y. Guo, X. Wu, C. Wu and Y. Xie, *J. Am. Chem. Soc.*, 2020, **142**, 18645–18651.

141 H. Morimoto, H. Yamashita, M. Tatsumisago and T. Minami, *J. Ceram. Soc. Jpn.*, 2000, **108**, 128–131.

142 T. Inada, T. Kobayashi, N. Sonoyama, A. Yamada, S. Kondo, M. Nagao and R. Kanno, *J. Power Sources*, 2009, **194**, 1085–1088.

143 A. Kuhn, V. Duppel and B. V. Lotsch, *Energy Environ. Sci.*, 2013, **6**, 3548.

144 Y. Kato, R. Saito, M. Sakano, A. Mitsui, M. Hirayama and R. Kanno, *J. Power Sources*, 2014, **271**, 60.

145 O. Kwon, M. Hirayama, K. Suzuki, Y. Kato, T. Saito, M. Yonemura, T. Kamiyama and R. Kanno, *J. Mater. Chem. A*, 2015, **3**, 438.

146 D. A. Weber, A. Senyshyn, K. S. Weldert, S. Wenzel, W. Zhang, R. Kaiser, S. Berendts, J. Janek and W. G. Zeier, *Chem. Mater.*, 2016, **28**, 5905–5915.

147 Y. Mo, S. P. Ong and G. Ceder, *Chem. Mater.*, 2012, **24**, 15–17.

148 K. Minami, A. Hayashi, S. Ujiie and M. Tatsumisago, *Solid State Ionics*, 2011, **192**, 122–125.

149 H. Muramatsu, A. Hayashi, T. Ohtomo, S. Hama and M. Tatsumisago, *Solid State Ionics*, 2011, **182**, 116–119.

150 I.-H. Chu, H. Nguyen, S. Hy, Y.-C. Lin, Z. Wang, Z. Xu, Z. Deng, Y. S. Meng and S. P. Ong, *ACS Appl. Mater. Interfaces*, 2016, **8**, 7843–7853.

151 B. R. Shin, Y. J. Nam, D. Y. Oh, D. H. Kim, J. W. Kim and Y. S. Jung, *Electrochim. Acta*, 2014, **146**, 395.

152 Z. Yu, S.-L. Shang, D. Wang, Y. C. Li, H. P. Yennawar, G. Li, H.-T. Huang, Y. Gao, T. E. Mallouk, Z.-K. Liu and D. Wang, *Energy Storage Mater.*, 2019, **17**, 70–77.

153 H. Zhang, X. Li, S. Hao, X. Zhang and J. Lin, *Electrochim. Acta*, 2019, **325**, 134943.

154 P. Gorai, H. Long, E. Jones, S. Santhanagopalan and V. Stevanović, *J. Mater. Chem. A*, 2020, **8**, 3851–3858.

155 S. P. Ong, Y. Mo, W. D. Richards, L. Miara, H. S. Lee and G. Ceder, *Energy Environ. Sci.*, 2013, **6**, 148–156.

156 I. Tarhouchi, V. Viallet, P. Vinatier and M. Ménétrier, *Solid State Ionics*, 2016, **296**, 18–25.

157 Q. Zhang, J. Hu, Y. Chu, W. Wan, L. Zhao and Y. Zhu, *Mater. Lett.*, 2019, **248**, 153–156.

158 R. B. Beeken, J. J. Garbe, J. M. Gillis, N. R. Petersen, B. W. Podoll and M. R. Stoneman, *J. Phys. Chem. Solids*, 2005, **66**, 882–886.

159 H. M. Chen, C. Maohua and S. Adams, *Phys. Chem. Chem. Phys.*, 2015, **17**, 16494–16506.

160 P. R. Rayavarapu, N. Sharma, V. K. Peterson and S. Adams, *J. Solid State Electrochem.*, 2012, **16**, 1807–1813.

161 S. T. Kong, Ö. Gün, B. Koch, H. J. Deiseroth, H. Eckert and C. Reiner, *Chem. – Eur. J.*, 2010, **16**, 5138–5147.

162 Z. Zhang, J. Zhang, H. Jia, L. Peng, T. An and J. Xie, *J. Power Sources*, 2020, **450**, 227601.

163 N. J. J. de Klerk, I. Rosłoń and M. Wagemaker, *Chem. Mater.*, 2016, **28**, 7955–7963.

164 C. Yu, S. Ganapathy, E. R. H. v. Eck, H. Wang, S. Basak, Z. Li and M. Wagemaker, *Nat. Commun.*, 2017, **8**, 1086.

165 H. Fudong, Y. Jie, Z. Xiangyang and W. Chunsheng, *Adv. Energy Mater.*, 2018, **0**, 1703644.

166 L. Zhou, K.-H. Park, X. Sun, F. Lalère, T. Adermann, P. Hartmann and L. F. Nazar, *ACS Energy Lett.*, 2018, **4**, 265–270.

167 S. Yubuchi, M. Uematsu, M. Deguchi, A. Hayashi and M. Tatsumisago, *ACS Appl. Energy Mater.*, 2018, **1**, 3622–3629.

168 N. C. Rosero-Navarro, A. Miura and K. Tadanaga, *J. Power Sources*, 2018, **396**, 33–40.

169 S. Chen, C. Niu, H. Lee, Q. Li, L. Yu, W. Xu, J.-G. Zhang, E. J. Dufek, M. S. Whittingham, S. Meng, J. Xiao and J. Liu, *Joule*, 2019, **3**, 1094–1105.

170 J. C. Bachman, S. Muy, A. Grimaud, H.-H. Chang, N. Pour, S. F. Lux, O. Paschos, F. Maglia, S. Lupart, P. Lamp, L. Giordano and Y. Shao-Horn, *Chem. Rev.*, 2016, **116**, 140–162.

171 T. Baba and Y. Kawamura, *Front. Energy Res.*, 2016, **4**, 22.

172 B. Zhang, R. Tan, L. Yang, J. Zheng, K. Zhang, S. Mo, Z. Lin and F. Pan, *Energy Storage Mater.*, 2018, **10**, 139–159.

173 Y. Gao, A. M. Nolan, P. Du, Y. Wu, C. Yang, Q. Chen, Y. Mo and S.-H. Bo, *Chem. Rev.*, 2020, **120**, 5954–6008.

174 Z. Gao, H. Sun, L. Fu, F. Ye, Y. Zhang, W. Luo and Y. Huang, *Adv. Mater.*, 2018, **30**, 1705702.

175 Y. Wang, W. D. Richards, S. P. Ong, L. J. Miara, J. C. Kim, Y. Mo and G. Ceder, *Nat. Mater.*, 2015, **14**, 1026–1031.

176 X. He, Y. Zhu and Y. Mo, *Nat. Commun.*, 2017, **8**, 15893.

This journal is © The Royal Society of Chemistry 2021

Energy Environ. Sci., 2021, **14**, 2577–2619 | **2613**

177 A. Gautam, M. Sadowski, M. Ghidiu, N. Minafra, A. Senyshyn, K. Albe and W. G. Zeier, *Adv. Energy Mater.*, 2020, **11**, 2003369.

178 Z. Zhu, H. Tang, J. Qi, X.-G. Li and S. P. Ong, *Adv. Energy Mater.*, 2021, **11**, 2003196.

179 J. Kim, Y. Yoon, M. Eom and D. Shin, *Solid State Ionics*, 2012, **225**, 626–630.

180 Y. Zhu and Y. Mo, *Angew. Chem., Int. Ed.*, 2020, **59**, 17472–17476.

181 A. Hayashi, H. Muramatsu, T. Ohtomo, S. Hama and M. Tatsumisago, *J. Mater. Chem. A*, 2013, **1**, 6320–6326.

182 T. Ohtomo, A. Hayashi, M. Tatsumisago and K. Kawamoto, *J. Mater. Sci.*, 2013, **48**, 4137–4142.

183 T. Ohtomo, A. Hayashi, M. Tatsumisago and K. Kawamoto, *J. Non-Cryst. Solids*, 2013, **364**, 57–61.

184 A. Hayashi, H. Muramatsu, T. Ohtomo, S. Hama and M. Tatsumisago, *J. Alloys Compd.*, 2014, **591**, 247–250.

185 G. Liu, D. Xie, X. Wang, X. Yao, S. Chen, R. Xiao, H. Li and X. Xu, *Energy Storage Mater.*, 2019, **17**, 266–274.

186 A. Banerjee, K. H. Park, J. W. Heo, Y. J. Nam, C. K. Moon, S. M. Oh, S.-T. Hong and Y. S. Jung, *Angew. Chem., Int. Ed.*, 2016, **55**, 9634–9638.

187 H. Wang, Y. Chen, Z. D. Hood, G. Sahu, A. S. Pandian, J. K. Keum, K. An and C. Liang, *Angew. Chem., Int. Ed.*, 2016, **55**, 8551–8555.

188 H. Kwak, K. H. Park, D. Han, K.-W. Nam, H. Kim and Y. S. Jung, *J. Power Sources*, 2020, **446**, 227338.

189 A. Fukushima, A. Hayashi, H. Yamamura and M. Tatsumisago, *Solid State Ionics*, 2017, **304**, 85–89.

190 Z. Zhang, L. Zhang, X. Yan, H. Wang, Y. Liu, C. Yu, X. Cao, L. van Eijck and B. Wen, *J. Power Sources*, 2019, **410–411**, 162–170.

191 Y. Li, B. Xu, H. Xu, H. Duan, X. Lü, S. Xin, W. Zhou, L. Xue, G. Fu, A. Manthiram and J. B. Goodenough, *Angew. Chem., Int. Ed.*, 2017, **56**, 753–756.

192 M. Calpa, N. C. Rosero-Navarro, A. Miura, R. Jalem, Y. Tateyama and K. Tadanaga, *Appl. Mater. Today*, 2021, **22**, 100918.

193 W. D. Jung, M. Jeon, S. S. Shin, J.-S. Kim, H.-G. Jung, B.-K. Kim, J.-H. Lee, Y.-C. Chung and H. Kim, *ACS Omega*, 2020, **5**, 26015–26022.

194 F. D. Han, Y. Z. Zhu, X. F. He, Y. F. Mo and C. S. Wang, *Adv. Energy Mater.*, 2016, **6**, 1501590.

195 W. D. Richards, L. J. Miara, Y. Wang, J. C. Kim and G. Ceder, *Chem. Mater.*, 2016, **28**, 266–273.

196 F. Wu, W. Fitzhugh, L. Ye, J. Ning and X. Li, *Nat. Commun.*, 2018, **9**, 4037.

197 S. Hori, K. Suzuki, M. Hirayama, Y. Kato and R. Kanno, *Front. Energy Res.*, 2016, **4**, 38.

198 K.-H. Park, K. Kaup, A. Assoud, Q. Zhang, X. Wu and L. F. Nazar, *ACS Energy Lett.*, 2020, **5**, 533–539.

199 K. J. Kim, M. Balaish, M. Wadaguchi, L. Kong and J. L. M. Rupp, *Adv. Energy Mater.*, 2021, **11**, 2002689.

200 J. Haruyama, K. Sodeyama, L. Y. Han, K. Takada and Y. Tateyama, *Chem. Mater.*, 2014, **26**, 4248–4255.

201 C. Chen and X. Guo, *Acta Chim. Slov.*, 2016, **63**, 489.

202 L. Wang, R. Xie, B. Chen, X. Yu, J. Ma, C. Li, Z. Hu, X. Sun, C. Xu, S. Dong, T.-S. Chan, J. Luo, G. Cui and L. Chen, *Nat. Commun.*, 2020, **11**, 5889.

203 Y. Nomura, K. Yamamoto, T. Hirayama, S. Ouchi, E. Igaki and K. Saitoh, *Angew. Chem., Int. Ed.*, 2019, **58**, 1–6.

204 N. J. J. de Klerk and M. Wagemaker, *ACS Appl. Energy Mater.*, 2018, **1**, 5609–5618.

205 M. Haruta, S. Shiraki, T. Suzuki, A. Kumatani, T. Ohsawa, Y. Takagi, R. Shimizu and T. Hitosugi, *Nano Lett.*, 2015, **15**, 1498–1502.

206 J. Haruyama, K. Sodeyama and Y. Tateyama, *ACS Appl. Mater. Interfaces*, 2017, **9**, 286–292.

207 Y. Zhu, X. He and Y. Mo, *ACS Appl. Mater. Interfaces*, 2015, **7**, 23685–23693.

208 A. Sakuda, A. Hayashi and M. Tatsumisago, *Chem. Mater.*, 2010, **22**, 949–956.

209 W. Zhang, F. H. Richter, S. P. Culver, T. Leichtweiss, J. G. Lozano, C. Dietrich, P. G. Bruce, W. G. Zeier and J. Janek, *ACS Appl. Mater. Interfaces*, 2018, **10**, 22226–22236.

210 A. Banerjee, H. Tang, X. Wang, J.-H. Cheng, H. Nguyen, M. Zhang, D. H. S. Tan, T. A. Wynn, E. A. Wu, J.-M. Doux, T. Wu, L. Ma, G. E. Sterbinsky, M. S. D'Souza, S. P. Ong and Y. S. Meng, *ACS Appl. Mater. Interfaces*, 2019, **11**, 43138–43145.

211 J. Auvergniot, A. Cassel, J.-B. Ledeuil, V. Viallet, V. Seznec and R. Dedryvère, *Chem. Mater.*, 2017, **29**, 3883–3890.

212 R. Koerver, I. Aygün, T. Leichtweiß, C. Dietrich, W. Zhang, J. O. Binder, P. Hartmann, W. G. Zeier and J. Janek, *Chem. Mater.*, 2017, **19**, 5574–5582.

213 C. Wang, X. Li, Y. Zhao, M. N. Banis, J. Liang, X. Li, Y. Sun, K. R. Adair, Q. Sun, Y. Liu, F. Zhao, S. Deng, X. Lin, R. Li, Y. Hu, T.-K. Sham, H. Huang, L. Zhang, R. Yang, S. Lu and X. Sun, *Small Methods*, 2019, **3**, 1900261.

214 X. Li, Z. Ren, M. Norouzi Banis, S. Deng, Y. Zhao, Q. Sun, C. Wang, X. Yang, W. Li, J. Liang, X. Li, Y. Sun, K. Adair, R. Li, Y. Hu, T.-K. Sham, H. Huang, L. Zhang, S. Lu, J. Luo and X. Sun, *ACS Energy Lett.*, 2019, **4**, 2480–2488.

215 Y. Zhu, X. He and Y. Mo, *J. Mater. Chem. A*, 2016, **4**, 3253–3266.

216 X. Meng, J. Liu, X. Li, M. N. Banis, J. Yang, R. Li and X. Sun, *RSC Adv.*, 2013, **3**, 7285–7288.

217 B. Wang, Y. Zhao, M. N. Banis, Q. Sun, K. R. Adair, R. Li, T.-K. Sham and X. Sun, *ACS Appl. Mater. Interfaces*, 2018, **10**, 1654–1661.

218 J. Liu, M. N. Banis, X. Li, A. Lushington, M. Cai, R. Li, T.-K. Sham and X. Sun, *J. Phys. Chem. C*, 2013, **117**, 20260–20267.

219 B. Wang, J. Liu, M. Norouzi Banis, Q. Sun, Y. Zhao, R. Li, T.-K. Sham and X. Sun, *ACS Appl. Mater. Interfaces*, 2017, **9**, 31786–31793.

220 B. Wang, J. Liu, Q. Sun, R. Li, T.-K. Sham and X. Sun, *Nanotechnology*, 2014, **25**, 504007.

221 F. Zhao, Y. Zhao, J. Wang, Q. Sun, K. Adair, S. Zhang, J. Luo, J. Li, W. Li, Y. Sun, X. Li, J. Liang, C. Wang, R. Li, H. Huang, L. Zhang, S. Zhao, S. Lu and X. Sun, *Energy Storage Mater.*, 2020, **33**, 139–146.

2614 | *Energy Environ. Sci.*, 2021, **14**, 2577–2619

This journal is © The Royal Society of Chemistry 2021

222 S. Deng, X. Li, Z. Ren, W. Li, J. Luo, J. Liang, J. Liang, M. N. Banis, M. Li, Y. Zhao, X. Li, C. Wang, Y. Sun, Q. Sun, R. Li, Y. Hu, H. Huang, L. Zhang, S. Lu, J. Luo and X. Sun, *Energy Storage Mater.*, 2020, **27**, 117–123.

223 K. Takada, T. Ohno, N. Ohta, T. Ohnishi and Y. Tanaka, *ACS Energy Lett.*, 2017, **3**, 98–103.

224 J. Zhang, C. Zheng, L. Li, Y. Xia, H. Huang, Y. Gan, C. Liang, X. He, X. Tao and W. Zhang, *Adv. Energy Mater.*, 2019, **10**, 1903311.

225 S. H. Jung, K. Oh, Y. J. Nam, D. Y. Oh, P. Brüner, K. Kang and Y. S. Jung, *Chem. Mater.*, 2018, **30**, 8190–8200.

226 X. Li, J. Liu, M. N. Banis, A. Lushington, R. Li, M. Cai and X. Sun, *Energy Environ. Sci.*, 2014, **7**, 768–778.

227 N. Ohta, K. Takada, I. Sakaguchi, L. Zhang, R. Ma, K. Fukuda, M. Osada and T. Sasaki, *Electrochem. Commun.*, 2007, **9**, 1486–1490.

228 N. Ohta, K. Takada, L. Zhang, R. Ma, M. Osada and T. Sasaki, *Adv. Mater.*, 2006, **18**, 2226–2229.

229 A. Sakuda, H. Kitaura, A. Hayashi, K. Tadanaga and M. Tatsumisago, *J. Electrochem. Soc.*, 2009, **156**, A27–A32.

230 J. W. Lee and Y. J. Park, *J. Electrochem. Sci. Technol.*, 2018, **9**, 176–183.

231 J. H. Woo, J. E. Trevey, A. S. Cavanagh, Y. S. Choi, S. C. Kim, S. M. George, K. H. Oh and S.-H. Lee, *J. Electrochem. Soc.*, 2012, **159**, A1120–A1124.

232 Y. Xiao, L. J. Miara, Y. Wang and G. Ceder, *Joule*, 2019, **3**, 1–24.

233 P. Yan, J. Zheng, J. Liu, B. Wang, X. Cheng, Y. Zhang, X. Sun, C. Wang and J.-G. Zhang, *Nat. Energy*, 2018, **3**, 600–605.

234 C. Wang, J. Liang, S. Hwang, X. Li, Y. Zhao, K. Adair, C. Zhao, X. Li, S. Deng, X. Lin, X. Yang, R. Li, H. Huang, L. Zhang, S. Lu, D. Su and X. Sun, *Nano Energy*, 2020, **72**, 104686.

235 D. Cao, Y. Zhang, A. M. Nolan, X. Sun, C. Liu, J. Sheng, Y. Mo, Y. Wang and H. Zhu, *Nano Lett.*, 2020, **20**, 1483–1490.

236 C. Yu, Y. Li, K. R. Adair, W. Li, K. Goubitz, Y. Zhao, M. J. Willans, M. A. Thijs, C. Wang, F. Zhao, Q. Sun, S. Deng, J. Liang, X. Li, R. Li, T.-K. Sham, H. Huang, S. Lu, S. Zhao, L. Zhang, L. van Eijck, Y. Huang and X. Sun, *Nano Energy*, 2020, **77**, 105097.

237 Y. Liu, S. Wang, A. M. Nolan, C. Ling and Y. Mo, *Adv. Energy Mater.*, 2020, **10**, 2002356.

238 M. Gombotz and H. M. R. Wilkening, *ACS Sustainable Chem. Eng.*, 2020, **9**, 743–755.

239 R. Schlem, A. Banik, S. Ohno, E. Suard and W. G. Zeier, *Chem. Mater.*, 2021, **33**, 327–337.

240 X. Li, J. Liang, N. Chen, J. Luo, K. R. Adair, C. Wang, M. N. Banis, T. K. Sham, L. Zhang and S. Zhao, *Angew. Chem., Int. Ed.*, 2019, **131**, 16579–16584.

241 Z. Xu, X. Chen, K. Liu, R. Chen, X. Zeng and H. Zhu, *Chem. Mater.*, 2019, **31**, 7425–7433.

242 D. Y. Oh, A. R. Ha, J. E. Lee, S. H. Jung, G. Jeong, W. Cho, K. S. Kim and Y. S. Jung, *ChemSusChem*, 2020, **13**, 146–151.

243 Y. B. Song, D. H. Kim, H. Kwak, D. Han, S. Kang, J. H. Lee, S.-M. Bak, K.-W. Nam, H.-W. Lee and Y. S. Jung, *Nano Lett.*, 2020, **20**, 4337–4345.

244 K. H. Park, D. Y. Oh, Y. E. Choi, Y. J. Nam, L. Han, J.-Y. Kim, H. Xin, F. Lin, S. M. Oh and Y. S. Jung, *Adv. Mater.*, 2016, **28**, 1874–1883.

245 Y. E. Choi, K. H. Park, D. H. Kim, D. Y. Oh, H. R. Kwak, Y.-G. Lee and Y. S. Jung, *ChemSusChem*, 2017, **10**, 2605–2611.

246 D. H. Kim, D. Y. Oh, K. H. Park, Y. E. Choi, Y. J. Nam, H. A. Lee, S.-M. Lee and Y. S. Jung, *Nano Lett.*, 2017, **17**, 3013–3020.

247 D. Y. Oh, D. H. Kim, S. H. Jung, J.-G. Han, N.-S. Choi and Y. S. Jung, *J. Mater. Chem. A*, 2017, **5**, 20771–20779.

248 S. Teragawa, K. Aso, K. Tadanaga, A. Hayashi and M. Tatsumisago, *J. Power Sources*, 2014, **248**, 939–942.

249 Z. D. Hood, H. Wang, A. S. Pandian, R. Peng, K. D. Gilroy, M. Chi, C. Liang and Y. Xia, *Adv. Energy Mater.*, 2018, **8**, 1800014.

250 H. Wang, Z. D. Hood, Y. Xia and C. Liang, *J. Mater. Chem. A*, 2016, **4**, 8091–8096.

251 M. Calpa, N. C. Rosero-Navarro, A. Miura and K. Tadanaga, *RSC Adv.*, 2017, **7**, 46499–46504.

252 K. Suzuki, A. Yageta, Y. Ikeda, N. Mashimo, S. Hori, M. Hirayama and R. Kanno, *Chem. Lett.*, 2020, **49**, 1379–1381.

253 S. Yubuchi, S. Teragawa, K. Aso, K. Tadanaga, A. Hayashi and M. Tatsumisago, *J. Power Sources*, 2015, **293**, 941–945.

254 N. C. Rosero-Navarro, A. Miura and K. Tadanaga, *J. Sol–Gel Sci. Technol.*, 2019, **89**, 303–309.

255 S. Yubuchi, M. Uematsu, C. Hotehama, A. Sakuda, A. Hayashi and M. Tatsumisago, *J. Mater. Chem. A*, 2019, **7**, 558–566.

256 J. Xu, L. Liu, N. Yao, F. Wu, H. Li and L. Chen, *Mater. Today Nano*, 2019, **8**, 100048.

257 Y. J. Nam, D. Y. Oh, S. H. Jung and Y. S. Jung, *J. Power Sources*, 2018, **375**, 93–101.

258 D. H. Kim, Y.-H. Lee, Y. B. Song, H. Kwak, S.-Y. Lee and Y. S. Jung, *ACS Energy Lett.*, 2020, **5**, 718–727.

259 Y. J. Nam, S. J. Cho, D. Y. Oh, J. M. Lim, S. Y. Kim, J. H. Song, Y. G. Lee, S. Y. Lee and Y. S. Jung, *Nano Lett.*, 2015, **15**, 3317–3323.

260 X. Yang, K. R. Adair, X. Gao and X. Sun, *Energy Environ. Sci.*, 2021, **14**, 643–671.

261 R. Koerver, W. Zhang, L. de Biasi, S. Schweidler, A. O. Kondrakov, S. Kolling, T. Brezesinski, P. Hartmann, W. G. Zeier and J. Janek, *Energy Environ. Sci.*, 2018, **11**, 2142–2158.

262 A. Hayashi, A. Sakuda and M. Tatsumisago, *Front. Energy Res.*, 2016, **4**, 25.

263 T. Shi, Y.-Q. Zhang, Q. Tu, Y. Wang, M. C. Scott and G. Ceder, *J. Mater. Chem. A*, 2020, **8**, 17399–17404.

264 W. Zhang, D. Schröder, T. Arlt, I. Manke, R. Koerver, R. Pinedo, D. A. Weber, J. Sann, W. G. Zeier and J. Janek, *J. Mater. Chem. A*, 2017, **5**, 9929–9936.

265 J.-M. Doux, Y. Yang, D. H. S. Tan, H. Nguyen, E. A. Wu, X. Wang, A. Banerjee and Y. S. Meng, *J. Mater. Chem. A*, 2020, **8**, 5049–5055.

266 J. M. Doux, H. Nguyen, D. H. Tan, A. Banerjee, X. Wang, E. A. Wu, C. Jo, H. Yang and Y. S. Meng, *Adv. Energy Mater.*, 2020, **10**, 1903253.

This journal is © The Royal Society of Chemistry 2021

Energy Environ. Sci., 2021, **14**, 2577–2619 | **2615**

267 W. Zhang, T. Leichtweiß, S. P. Culver, R. Koerver, D. Das, D. A. Weber, W. G. Zeier and J. Janek, *ACS Appl. Mater. Interfaces*, 2017, **9**, 35888–35896.

268 G. Oh, M. Hirayama, O. Kwon, K. Suzuki and R. Kanno, *Chem. Mater.*, 2016, **28**, 2634–2640.

269 D. H. S. Tan, E. A. Wu, H. Nguyen, Z. Chen, M. A. T. Marple, J.-M. Doux, X. Wang, H. Yang, A. Banerjee and Y. S. Meng, *ACS Energy Lett.*, 2019, **4**, 2418–2427.

270 S. Deng, Y. Sun, X. Li, Z. Ren, J. Liang, K. Doyle-Davis, J. Liang, W. Li, M. Norouzi Banis and Q. Sun, *ACS Energy Lett.*, 2020, **5**, 1243–1251.

271 F. Strauss, D. Stepien, J. Maibach, L. Pfaffmann, S. Indris, P. Hartmann and T. Brezesinski, *RSC Adv.*, 2020, **10**, 1114–1119.

272 T. Swamy, X. Chen and Y.-M. Chiang, *Chem. Mater.*, 2019, **31**, 707–713.

273 F. Walther, S. Randau, Y. Schneider, J. Sann, M. Rohnke, F. H. Richter, W. G. Zeier and J. Janek, *Chem. Mater.*, 2020, **32**, 6123–6136.

274 K. Yoon, J.-J. Kim, W. M. Seong, M. H. Lee and K. Kang, *Sci. Rep.*, 2018, **8**, 8066.

275 C. Cui, X. Fan, X. Zhou, J. Chen, Q. Wang, L. Ma, C. Yang, E. Hu, X.-Q. Yang and C. Wang, *J. Am. Chem. Soc.*, 2020, **142**, 8918–8927.

276 H. Chen, C. Wang, W. Dong, W. Lu, Z. Du and L. Chen, *Nano Lett.*, 2015, **15**, 798–802.

277 G. Girishkumar, B. McCloskey, A. C. Luntz, S. Swanson and W. Wilcke, *J. Phys. Chem. Lett.*, 2010, **1**, 2193–2203.

278 P. G. Bruce, S. A. Freunberger, L. J. Hardwick and J.-M. Tarascon, *Nat. Mater.*, 2012, **11**, 19–29.

279 X. L. Ji, K. T. Lee and L. F. Nazar, *Nat. Mater.*, 2009, **8**, 500–506.

280 Y. Sun, N. Liu and Y. Cui, *Nat. Energy*, 2016, **1**, 16071.

281 Y. Li, W. Zhou, X. Chen, X. Lü, Z. Cui, S. Xin, L. Xue, Q. Jia and J. B. Goodenough, *Proc. Natl. Acad. Sci. U. S. A.*, 2016, **113**, 13313–13317.

282 Y. Tang, L. Zhang, J. Chen, H. Sun, T. Yang, Q. Liu, Q. Huang, T. Zhu and J. Huang, *Energy Environ. Sci.*, 2021, **14**, 602–642.

283 T. Krauskopf, F. H. Richter, W. G. Zeier and J. Janek, *Chem. Rev.*, 2020, **120**, 7745–7794.

284 C. Fu, V. Venturi, J. Kim, Z. Ahmad, A. W. Ells, V. Viswanathan and B. A. Helms, *Nat. Mater.*, 2020, **19**, 758–766.

285 Y. Huang, J. Duan, X. Zheng, J. Wen, Y. Dai, Z. Wang, W. Luo and Y. Huang, *Matter*, 2020, **3**, 1009–1030.

286 J. Kasemchainan, S. Zekoll, D. Spencer Jolly, Z. Ning, G. O. Hartley, J. Marrow and P. G. Bruce, *Nat. Mater.*, 2019, **18**, 1105–1111.

287 S. Wenzel, S. Randau, T. Leichtweiß, D. A. Weber, J. Sann, W. G. Zeier and J. Janek, *Chem. Mater.*, 2016, **28**, 2400–2407.

288 P. Bron, B. Roling and S. Dehnen, *J. Power Sources*, 2017, **352**, 127–134.

289 S. Wenzel, S. J. Sedlmaier, C. Dietrich, W. G. Zeier and J. Janek, *Solid State Ionics*, 2018, **318**, 102–112.

290 J. Janek and W. G. Zeier, *Nat. Energy*, 2016, **1**, 16141.

291 M. Nagao, A. Hayashi, M. Tatsumisago, T. Kanetsuku, T. Tsuda and S. Kuwabata, *Phys. Chem. Chem. Phys.*, 2013, **15**, 18600.

292 A. M. Nolan, Y. Zhu, X. He, Q. Bai and Y. Mo, *Joule*, 2018, **2**, 2016–2046.

293 X. Fan, X. Ji, F. Han, J. Yue, J. Chen, L. Chen, T. Deng, J. Jiang and C. Wang, *Sci. Adv.*, 2018, **4**, 9245.

294 J. Liang, X. Li, Y. Zhao, L. V. Goncharova, W. Li, K. R. Adair, M. N. Banis, Y. Hu, T.-K. Sham, H. Huang, L. Zhang, S. Zhao, S. Lu, R. Li and X. Sun, *Adv. Energy Mater.*, 2019, **9**, 1902125.

295 C. Wang, Y. Zhao, Q. Sun, X. Li, Y. Liu, J. Liang, X. Li, X. Lin, R. Li, K. R. Adair, L. Zhang, R. Yang, S. Lu and X. Sun, *Nano Energy*, 2018, **53**, 168–174.

296 F. Zhao, Q. Sun, C. Yu, S. Zhang, K. Adair, S. Wang, Y. Liu, Y. Zhao, J. Liang, C. Wang, X. Li, X. Li, W. Xia, R. Li, H. Huang, L. Zhang, S. Zhao, S. Lu and X. Sun, *ACS Energy Lett.*, 2020, **5**, 1035–1043.

297 P. Hartmann, T. Leichtweiss, M. R. Busche, M. Schneider, M. Reich, J. Sann, P. Adelhelm and J. r. Janek, *J. Phys. Chem. C*, 2013, **117**, 21064–21074.

298 S. Wenzel, T. Leichtweiss, D. Krüger, J. Sann and J. Janek, *Solid State Ionics*, 2015, **278**, 98–105.

299 S. Wenzel, D. A. Weber, T. Leichtweiss, M. R. Busche, J. Sann and J. Janek, *Solid State Ionics*, 2016, **286**, 24–33.

300 A. Schwöbel, R. Hausbrand and W. Jaegermann, *Solid State Ionics*, 2015, **273**, 51–54.

301 M. Sakuma, K. Suzuki, M. Hirayama and R. Kanno, *Solid State Ionics*, 2016, **285**, 101–105.

302 T. Kobayashi, A. Yamada and R. Kanno, *Electrochim. Acta*, 2008, **53**, 5045–5050.

303 Y. Gao, D. Wang, Y. C. Li, Z. Yu, T. E. Mallouk and D. Wang, *Angew. Chem., Int. Ed.*, 2018, **57**, 13608–13612.

304 J. Liang, X. Li, Y. Zhao, L. V. Goncharova, G. Wang, K. R. Adair, C. Wang, R. Li, Y. Zhu, Y. Qian, L. Zhang, R. Yang, S. Lu and X. Sun, *Adv. Mater.*, 2018, **30**, 1804684.

305 Z. Zhang, S. Chen, J. Yang, J. Wang, L. Yao, X. Yao, P. Cui and X. Xu, *ACS Appl. Mater. Interfaces*, 2017, **10**, 2556–2565.

306 Y. Sun, Y. Zhao, J. Wang, J. Liang, C. Wang, Q. Sun, X. Lin, K. R. Adair, J. Luo, D. Wang, R. Li, M. Cai, T.-K. Sham and X. Sun, *Adv. Mater.*, 2019, **31**, 1806541.

307 X.-B. Cheng, R. Zhang, C.-Z. Zhao and Q. Zhang, *Chem. Rev.*, 2017, **117**, 10403–10473.

308 D. Lin, Y. Liu and Y. Cui, *Nat. Nanotechnol.*, 2017, **12**, 194–206.

309 X.-Q. Zhang, X.-B. Cheng and Q. Zhang, *Adv. Mater. Interfaces*, 2018, **5**, 1701097.

310 Q. Pang, X. Liang, A. Shyamsunder and L. F. Nazar, *Joule*, 2017, **1**, 871–886.

311 X. Ji, S. Hou, P. Wang, X. He, N. Piao, J. Chen, X. Fan and C. Wang, *Adv. Mater.*, 2020, **32**, 2002741.

312 A. D. Bui, S.-H. Choi, H. Choi, Y.-J. Lee, C.-H. Doh, J.-W. Park, B. G. Kim, W.-J. Lee, S.-M. Lee and Y.-C. Ha, *ACS Appl. Energy Mater.*, 2021, **4**, 1–8.

313 W. Jiang, L. Yan, X. Zeng, X. Meng, R. Huang, X. Zhu, M. Ling and C. Liang, *ACS Appl. Mater. Interfaces*, 2020, **12**, 54876–54883.

2616 | *Energy Environ. Sci.*, 2021, **14**, 2577–2619

This journal is © The Royal Society of Chemistry 2021

314 F. Han, A. S. Westover, J. Yue, X. Fan, F. Wang, M. Chi, D. N. Leonard, N. J. Dudney, H. Wang and C. Wang, *Nat. Energy*, 2019, **4**, 187–196.

315 C. Niu, H. Lee, S. Chen, Q. Li, J. Du, W. Xu, J.-G. Zhang, M. S. Whittingham, J. Xiao and J. Liu, *Nat. Energy*, 2019, **4**, 551–559.

316 P. Shi, X.-B. Cheng, T. Li, R. Zhang, H. Liu, C. Yan, X.-Q. Zhang, J.-Q. Huang and Q. Zhang, *Adv. Mater.*, 2019, **31**, 1902785.

317 J. Xiao, Q. Li, Y. Bi, M. Cai, B. Dunn, T. Glossmann, J. Liu, T. Osaka, R. Sugiura, B. Wu, J. Yang, J.-G. Zhang and M. S. Whittingham, *Nat. Energy*, 2020, **5**, 561–568.

318 H. Li, D. Chao, B. Chen, X. Chen, C. Chuah, Y. Tang, Y. Jiao, M. Jaroniec and S.-Z. Qiao, *J. Am. Chem. Soc.*, 2020, **142**, 2012–2022.

319 L. Sang, R. T. Haasch, A. A. Gewirth and R. G. Nuzzo, *Chem. Mater.*, 2017, **29**, 3029–3037.

320 X. Li, J. Liang, X. Li, C. Wang, J. Luo, R. Li and X. Sun, *Energy Environ. Sci.*, 2018, **11**, 2828.

321 Y. Yamagishi, H. Morita, Y. Nomura and E. Igaki, *ACS Appl. Mater. Interfaces*, 2021, **13**, 580–586.

322 C. Wang, Y. Gong, J. Dai, L. Zhang, H. Xie, G. Pastel, B. Liu, E. Wachsman, H. Wang and L. Hu, *J. Am. Chem. Soc.*, 2017, **139**, 14257–14264.

323 H. Masuda, N. Ishida, Y. Ogata, D. Ito and D. Fujita, *Nanoscale*, 2017, **9**, 893–898.

324 P.-H. Chien, X. Feng, M. Tang, J. T. Rosenberg, S. O'Neill, J. Zheng, S. C. Grant and Y.-Y. Hu, *J. Phys. Chem. Lett.*, 2018, **9**, 1990–1998.

325 Z. Wang, D. Santhanagopalan, W. Zhang, F. Wang, H. L. Xin, K. He, J. Li, N. Dudney and Y. S. Meng, *Nano Lett.*, 2016, **16**, 3760–3767.

326 N. Seitzman, H. Guthrey, D. B. Sulas, H. A. S. Platt, M. Al-Jassim and S. Pylypenko, *J. Electrochem. Soc.*, 2018, **165**, A3732–A3737.

327 A. M. Abakumov, S. S. Fedotov, E. V. Antipov and J.-M. Tarascon, *Nat. Commun.*, 2020, **11**, 4976.

328 D. H. S. Tan, A. Banerjee, Z. Chen and Y. S. Meng, *Nat. Nanotechnol.*, 2020, **15**, 170–180.

329 Y. Li, Z. Gao, F. Hu, X. Lin, Y. Wei, J. Peng, J. Yang, Z. Li, Y. Huang and H. Ding, *Small Methods*, 2020, **4**, 2000111.

330 Z. Deng, X. Lin, Z. Huang, J. Meng, Y. Zhong, G. Ma, Y. Zhou, Y. Shen, H. Ding and Y. Huang, *Adv. Energy Mater.*, 2021, **11**, 2000806.

331 Y. Li, Z. Gao, F. Hu, X. Lin, Y. Wei, J. Peng, J. Yang, Z. Li, Y. Huang and H. Ding, *Small Methods*, 2020, **4**, 2000111.

332 K. N. Wood, K. X. Steirer, S. E. Hafner, C. Ban, S. Santhanagopalan, S.-H. Lee and G. Teeter, *Nat. Commun.*, 2018, **9**, 2490.

333 Y. Zhou, C. Doerrer, J. Kasemchainan, P. G. Bruce, M. Pasta and L. Hardwick, *Batteries Supercaps*, 2020, **3**, 647.

334 M. Otoyama, Y. Ito, A. Hayashi and M. Tatsumisago, *J. Power Sources*, 2016, **302**, 419–425.

335 X. Liu, D. Wang, G. Liu, V. Srinivasan, Z. Liu, Z. Hussain and W. Yang, *Nat. Commun.*, 2013, **4**, 2568.

336 J. F. M. Oudenhoven, F. Labohm, M. Mulder, R. A. H. Niessen, F. M. Mulder and P. H. L. Notten, *Adv. Mater.*, 2011, **23**, 4103–4106.

337 Q. Li, T. Yi, X. Wang, H. Pan, B. Quan, T. Liang, X. Guo, X. Yu, H. Wang, X. Huang, L. Chen and H. Li, *Nano Energy*, 2019, **63**, 103895.

338 C. Wang, Y. Gong, J. Dai, L. Zhang, H. Xie, G. Pastel, B. Liu, E. Wachsman, H. Wang and L. Hu, *J. Am. Chem. Soc.*, 2017, **139**, 14257–14264.

339 X. Sun, A. M. Stavola, D. Cao, A. M. Bruck, Y. Wang, Y. Zhang, P. Luan, J. W. Gallaway and H. Zhu, *Adv. Energy Mater.*, 2020, **11**, 2002861.

340 M. B. Dixit, W. Zaman, N. Hortance, S. Vujic, B. Harkey, F. Shen, W.-Y. Tsai, V. De Andrade, X. C. Chen, N. Balke and K. B. Hatzell, *Joule*, 2020, **4**, 207–221.

341 J. Wan, Y.-X. Song, W.-P. Chen, H.-J. Guo, Y. Shi, Y.-J. Guo, J.-L. Shi, Y.-G. Guo, F.-F. Jia, F.-Y. Wang, R. Wen and L.-J. Wan, *J. Am. Chem. Soc.*, 2020, **143**, 839–848.

342 Z. D. Hood, X. Chen, R. L. Sacci, X. Liu, G. M. Veith, Y. Mo, J. Niu, N. J. Dudney and M. Chi, *Nano Lett.*, 2021, **21**, 151–157.

343 Y. Yamada, K. Suzuki, K. Yoshino, S. Taminato, T. Satoh, M. Finsterbusch, T. Kamiya, A. Yamazaki, Y. Kato, K. Fujita, K. Mima, S. Hori, M. Hirayama and R. Kanno, *Electrochemistry*, 2020, **88**, 45–49.

344 Y. Xiao, Y. Wang, S.-H. Bo, J. C. Kim, L. J. Miara and G. Ceder, *Nat. Rev. Mater.*, 2019, **5**, 105–126.

345 Y. Zhang, X. He, Z. Chen, Q. Bai, A. M. Nolan, C. A. Roberts, D. Banerjee, T. Matsunaga, Y. Mo and C. Ling, *Nat. Commun.*, 2019, **10**, 5260.

346 S. Muy, J. Voss, R. Schlem, R. Koerver, S. J. Sedlmaier, F. Maglia, P. Lamp, W. G. Zeier and Y. Shao-Horn, *iScience*, 2019, **16**, 270–282.

347 Y. Tateyama, B. Gao, R. Jalem and J. Haruyama, *Curr. Opin. Electrochem.*, 2019, **17**, 149–157.

348 Z. Wang and G. Shao, *J. Mater. Chem. A*, 2017, **5**, 21846–21857.

349 T. Shi, Q. Tu, Y. Tian, Y. Xiao, L. J. Miara, O. Kononova and G. Ceder, *Adv. Energy Mater.*, 2019, **10**, 1902881.

350 Z. Xu, R. Chen and H. Zhu, *J. Mater. Chem. A*, 2019, **7**, 12645–12653.

351 F. Hao, Y. Liang, Y. Zhang, Z. Chen, J. Zhang, Q. Ai, H. Guo, Z. Fan, J. Lou and Y. Yao, *ACS Energy Lett.*, 2021, **6**, 201–207.

352 F. Hao, X. Chi, Y. Liang, Y. Zhang, R. Xu, H. Guo, T. Terlier, H. Dong, K. Zhao, J. Lou and Y. Yao, *Joule*, 2019, **3**, 1349–1359.

353 X. Chi, Y. Liang, F. Hao, Y. Zhang, J. Whiteley, H. Dong, P. Hu, S. Lee and Y. Yao, *Angew. Chem., Int. Ed.*, 2018, **57**, 2630–2634.

354 F. Strauss, J. H. Teo, J. Maibach, A. Y. Kim, A. Mazilkin, J. Janek and T. Brezesinski, *ACS Appl. Mater. Interfaces*, 2020, **12**, 57146–57154.

355 X. Yang, X. Li, K. Adair, H. Zhang and X. Sun, *Electrochem. Energy Rev.*, 2018, **1**, 239–293.

356 J. Yin, X. Yao, G. Peng, J. Yang, Z. Huang, D. Liu, Y. Tao and X. Xu, *Solid State Ionics*, 2015, **274**, 8–11.

357 H. Tsukasaki, Y. Mori, M. Otoyama, S. Yubuchi, T. Asano, Y. Tanaka, T. Ohno, S. Mori, A. Hayashi and M. Tatsumisago, *Sci. Rep.*, 2018, **8**, 6214.

This journal is © The Royal Society of Chemistry 2021

Energy Environ. Sci., 2021, **14**, 2577–2619 | **2617**

358 F. Strauss, T. Bartsch, L. de Biasi, A. Y. Kim, J. Janek, P. Hartmann and T. Brezesinski, *ACS Energy Lett.*, 2018, **3**, 992–996.

359 T. Bartsch, F. Strauss, T. Hatsukade, A. Schiele, A. Y. Kim, P. Hartmann, J. Janek and T. Brezesinski, *ACS Energy Lett.*, 2018, **3**, 2539–2543.

360 S. Deng, Q. Sun, M. Li, K. Adair, C. Yu, J. Li, W. Li, J. Fu, X. Li, R. Li, Y. Hu, N. Chen, H. Huang, L. Zhang, S. Zhao, S. Lu and X. Sun, *Energy Storage Mater.*, 2021, **35**, 661–668.

361 C. Wang, R. Yu, S. Hwang, J. Liang, X. Li, C. Zhao, Y. Sun, J. Wang, N. Holmes, R. Li, H. Huang, S. Zhao, L. Zhang, S. Lu, D. Su and X. Sun, *Energy Storage Mater.*, 2020, **30**, 98–103.

362 S. H. Jung, U.-H. Kim, J.-H. Kim, S. Jun, C. S. Yoon, Y. S. Jung and Y.-K. Sun, *Adv. Energy Mater.*, 2020, **10**, 1903360.

363 C. Wang, K. R. Adair, J. Liang, X. Li, Y. Sun, X. Li, J. Wang, Q. Sun, F. Zhao, X. Lin, R. Li, H. Huang, L. Zhang, R. Yang, S. Lu and X. Sun, *Adv. Funct. Mater.*, 2019, **29**, 1900392.

364 C. Yu, Y. Li, M. Willans, Y. Zhao, K. R. Adair, F. Zhao, W. Li, S. Deng, J. Liang, M. N. Banis, R. Li, H. Huang, L. Zhang, R. Yang, S. Lu, Y. Huang and X. Sun, *Nano Energy*, 2020, **69**, 104396.

365 X. Liu, B. Zheng, J. Zhao, W. Zhao, Z. Liang, Y. Su, C. Xie, K. Zhou, Y. Xiang, J. Zhu, H. Wang, G. Zhong, Z. Gong, J. Huang and Y. Yang, *Adv. Energy Mater.*, 2021, **11**, 2003583.

366 A. Sakuda, A. Hayashi, T. Ohtomo, S. Hama and M. Tatsumisago, *Electrochem. Solid-State Lett.*, 2010, **13**, A73–A75.

367 X. Li, Q. Sun, Z. Wang, D. Song, H. Zhang, X. Shi, C. Li, L. Zhang and L. Zhu, *J. Power Sources*, 2020, **456**, 227997.

368 G.-L. Zhu, C.-Z. Zhao, H. Yuan, B.-C. Zhao, L.-P. Hou, X.-B. Cheng, H.-X. Nan, Y. Lu, J. Zhang, J.-Q. Huang, Q.-B. Liu, C.-X. He and Q. Zhang, *Energy Storage Mater.*, 2020, **31**, 267–273.

369 K. Aso, A. Sakuda, A. Hayashi and M. Tatsumisago, *ACS Appl. Mater. Interfaces*, 2013, **5**, 686–690.

370 H. Chen, C. Wang, Y. Dai, S. Qiu, J. Yang, W. Lu and L. Chen, *Nano Lett.*, 2015, **15**, 5443–5448.

371 Q. Pang, X. Liang, C. Y. Kwok and L. F. Nazar, *Nat. Energy*, 2016, **1**, 16132.

372 D. He, J. Meng, X. Chen, Y. Liao, Z. Cheng, L. Yuan, Z. Li and Y. Huang, *Adv. Funct. Mater.*, 2021, **31**, 2001201.

373 Z. Rao, J. Meng, J. Wu, S. Yu, Q. Fu and Y. Huang, *ACS Appl. Energy Mater.*, 2020, **3**, 10139–10146.

374 H. Chen, C. Wang, Y. Dai, J. Ge, W. Lu, J. Yang and L. Chen, *Nano Energy*, 2016, **26**, 43–49.

375 C. Wang, H. Chen, W. Dong, J. Ge, W. Lu, X. Wu, L. Guo and L. Chen, *Chem. Commun.*, 2014, **50**, 1202–1204.

376 X. Li, M. Banis, A. Lushington, X. Yang, Q. Sun, Y. Zhao, C. Liu, Q. Li, B. Wang, W. Xiao, C. Wang, M. Li, J. Liang, R. Li, Y. Hu, L. Goncharova, H. Zhang, T.-K. Sham and X. Sun, *Nat. Commun.*, 2018, **9**, 4509.

377 Z. Lin and C. Liang, *J. Mater. Chem. A*, 2015, **3**, 936–958.

378 M. Nagao, A. Hayashi and M. Tatsumisago, *Electrochim. Acta*, 2011, **56**, 6055–6059.

379 A. Hayashi, T. Ohtomo, F. Mizuno, K. Tadanaga and M. Tatsumisago, *Electrochem. Commun.*, 2003, **5**, 701–705.

380 T. Kobayashi, Y. Imade, D. Shishihara, K. Homma, M. Nagao, R. Watanabe, T. Yokoi, A. Yamada, R. Kanno and T. Tatsumi, *J. Power Sources*, 2008, **182**, 621–625.

381 E. Umeshbabu, B. Zheng and Y. Yang, *Electrochem. Energy Rev.*, 2019, **2**, 199–230.

382 T. Yamada, S. Ito, R. Omoda, T. Watanabe, Y. Aihara, M. Agostini, U. Ulissi, J. Hassoun and B. Scrosati, *J. Electrochem. Soc.*, 2015, **162**, A646–A651.

383 Z. Lin, Z. Liu, W. Fu, N. J. Dudney and C. Liang, *Angew. Chem., Int. Ed.*, 2013, **125**, 7608–7611.

384 W. Liu, X. Sun, H. Wang and X. Cao, *Front. Energy Res.*, 2019, **7**, 112.

385 J. Yue, Y. Huang, S. Liu, J. Chen, F. Han and C. Wang, *ACS Appl. Mater. Interfaces*, 2020, **12**, 36066–36071.

386 R. Xu, J. Yue, S. Liu, J. Tu, F. Han, P. Liu and C. Wang, *ACS Energy Lett.*, 2019, **4**, 1073–1079.

387 F. Han, J. Yue, X. Fan, T. Gao, C. Luo, Z. Ma, L. Suo and C. Wang, *Nano Lett.*, 2016, **16**, 4521–4527.

388 Z. Lin, Z. Liu, N. J. Dudney and C. Liang, *ACS Nano*, 2013, **7**, 2829–2833.

389 T. Hakari, A. Hayashi and M. Tatsumisago, *Adv. Sustainable Syst.*, 2017, **1**, 1700017.

390 X. Li, J. Liang, M. N. Banis, J. Luo, C. Wang, W. Li, X. Li, Q. Sun, Y. Hu, Q. Xiao, T.-K. Sham, L. Zhang, S. Zhao, S. Lu, H. Huang, R. Li and X. Sun, *Energy Storage Mater.*, 2020, **28**, 325–333.

391 J. P. Mwizerwa, Q. Zhang, F. Han, H. Wan, L. Cai, C. Wang and X. Yao, *ACS Appl. Mater. Interfaces*, 2020, **12**, 18519–18525.

392 Y. Kawasaki, H. Tsukasaki, T. Ayama, S. Mori, M. Deguchi, M. Tatsumisago, A. Sakuda and A. Hayashi, *ACS Appl. Energy Mater.*, 2021, **4**, 20–24.

393 X. Qi, Y. Yang, Q. Jin, F. Yang, Y. Xie, P. Sang, K. Liu, W. Zhao, X. Xu, Y. Fu, J. Zhou, L. Qie and Y. Huang, *Angew. Chem., Int. Ed.*, 2020, **59**, 13908–13914.

394 S. Li, W. Zhang, Z. Zeng, S. Cheng and J. Xie, *Electrochem. Energy Rev.*, 2020, **3**, 613–642.

395 S. Randau, D. A. Weber, O. Kötz, R. Koerver, P. Braun, A. Weber, E. Ivers-Tiffée, T. Adermann, J. Kulisch, W. G. Zeier, F. H. Richter and J. Janek, *Nat. Energy*, 2020, **5**, 259–270.

396 L. Liu, J. Xu, S. Wang, F. Wu, H. Li and L. Chen, *eTransportation*, 2019, **1**, 100010.

397 J. Schnell, T. Günther, T. Knoche, C. Vieider, L. Köhler, A. Just, M. Keller, S. Passerini and G. Reinhart, *J. Power Sources*, 2018, **382**, 160–175.

398 A. Sakuda, K. Kuratani, M. Yamamoto, M. Takahashi, T. Takeuchi and H. Kobayashi, *J. Electrochem. Soc.*, 2017, **164**, A2474–A2478.

399 K. Kerman, A. Luntz, V. Viswanathan, Y.-M. Chiang and Z. Chen, *J. Electrochem. Soc.*, 2017, **164**, A1731–A1744.

400 L. Baggetto, R. A. H. Niessen, F. Roozeboom and P. H. L. Notten, *Adv. Funct. Mater.*, 2008, **18**, 1057–1066.

401 K. J. Huang, G. Ceder and E. A. Olivetti, *Joule*, 2021, **5**, 564–580.

2618 | *Energy Environ. Sci.*, 2021, **14**, 2577–2619

This journal is © The Royal Society of Chemistry 2021

402 H. Yuan, J. Liu, Y. Lu, C. Zhao, X. Cheng, H. Nan, Q. Liu, J. Huang and Q. Zhang, *Chem. Res. Chin. Univ.*, 2020, 1–9.

403 J. Wu, Z. Rao, Z. Cheng, L. Yuan, Z. Li and Y. Huang, *Adv. Energy Mater.*, 2019, **9**, 1902767.

404 J. Schnell, H. Knörzer, A. J. Imbsweiler and G. Reinhart, *Energy Technol.*, 2020, **8**, 1901237.

405 N. Machida, J. Kashiwagi, M. Naito and T. Shigematsu, *Solid State Ionics*, 2012, **225**, 354–358.

406 J. Y. Kim, J. Park, M. J. Lee, S. H. Kang, D. O. Shin, J. Oh, J. Kim, K. M. Kim, Y.-G. Lee and Y. M. Lee, *ACS Energy Lett.*, 2020, **5**, 2995–3004.

407 A. Chen, C. Qu, Y. Shi and F. Shi, *Front. Energy Res.*, 2020, **8**, 226.

408 D. H. Kim, H. A. Lee, Y. B. Song, J. W. Park, S.-M. Lee and Y. S. Jung, *J. Power Sources*, 2019, **426**, 143–150.

409 T. Jiang, P. He, G. Wang, Y. Shen, C.-W. Nan and L.-Z. Fan, *Adv. Energy Mater.*, 2020, **10**, 1903376.

410 M. Yamamoto, Y. Terauchi, A. Sakuda and M. Takahashi, *Sci. Rep.*, 2018, **8**, 1212.

411 B. Wu, S. Wang, W. J. Evans Iv, D. Z. Deng, J. Yang and J. Xiao, *J. Mater. Chem. A*, 2016, **4**, 15266–15280.

412 J. Betz, G. Bieker, P. Meister, T. Placke, M. Winter and R. Schmuch, *Adv. Energy Mater.*, 2018, 1803170.

413 J. Wan, J. Xie, X. Kong, Z. Liu, K. Liu, F. Shi, A. Pei, H. Chen, W. Chen, J. Chen, X. Zhang, L. Zong, J. Wang, L.-Q. Chen, J. Qin and Y. Cui, *Nat. Nanotechnol.*, 2019, **14**, 705–711.

414 J. M. Whiteley, P. Taynton, W. Zhang and S.-H. Lee, *Adv. Mater.*, 2015, **27**, 6922–6927.

415 S. Thieme, J. Brückner, I. Bauer, M. Oschatz, L. Borchardt, H. Althues and S. Kaskel, *J. Mater. Chem. A*, 2013, **1**, 9225–9234.

416 F. Hippauf, B. Schumm, S. Doerfler, H. Althues, S. Fujiki, T. Shiratsuchi, T. Tsujimura, Y. Aihara and S. Kaskel, *Energy Storage Mater.*, 2019, **21**, 390–398.

417 S. Cangaz, F. Hippauf, F. S. Reuter, S. Doerfler, T. Abendroth, H. Althues and S. Kaskel, *Adv. Energy Mater.*, 2020, **10**, 2001320.

418 T. Inoue and K. Mukai, *ACS Appl. Mater. Interfaces*, 2017, **9**, 1507–1515.

419 J. Duan, X. Tang, H. Dai, Y. Yang, W. Wu, X. Wei and Y. Huang, *Electrochem. Energy Rev.*, 2020, **3**, 1–42.

420 X. Yang, J. Luo and X. Sun, *Chem. Soc. Rev.*, 2020, **49**, 2140–2195.

421 J. Wu, L. Yuan, W. Zhang, Z. Li, X. Xie and Y. Huang, *Energy Environ. Sci.*, 2021, **14**, 12–36.

This journal is © The Royal Society of Chemistry 2021

Energy Environ. Sci., 2021, **14**, 2577–2619 | **2619**